TRAJECTORY OPTIMIZATION FOR FUEL CELL POWERED UAVS

A Dissertation
Presented to
The Academic Faculty

by

Min Zhou

In Partial Fulfillment
of the Requirements for the Degree
Doctor of Philosophy in the

School of Aerospace Engineering
Georgia Institute of Technology

December, 2013

TRAJECTORY OPTIMIZATION FOR FUEL CELL POWERED UAVS

Approved by:

Dr. J.V.R. Prasad
School of Aerospace Engineering
Georgia Institute of Technology

Dr. Dimitri Mavris
School of Aerospace Engineering
Georgia Institute of Technology

Dr. Eric Johnson
School of Aerospace Engineering
Georgia Institute of Technology

Dr. Chang Chen
Guided System Division
DSO National Laboratories, Singapore

Dr. Mark Costello
School of Aerospace Engineering
Georgia Institute of Technology

Date Approved: August 9, 2013

ACKNOWLEDGEMENTS

I would like to express my sincere gratitude to my advisor, Dr. Prasad, for his continuous guidance, valuable suggestions, and insightful advice. I have deeply appreciated his patience for the last five years. I would also like to thank my thesis committee members, Dr. Eric Johnson, Dr. Mark Costello, Dr. Dimitri Mavris, and Dr. Chang Chen, for their comments and suggestions.

My five years of study at Georgia Tech would not have been possible without the financial sponsorship from DSO National Laboratories and I sincerely thank my division director, Dr. Tan Kok Tin, for recommending me for the DSO postgraduate scholarship. The scholarship would also not have been possible without the support from my superiors, Dr. Ho Quan Wai, Dr. Chen Wei Peng, Dr. Chang Yew Wing, Mr. Peter Seah, Mr. Lim Kok Yong, Mr. Yew Gim Koon, Mr. Yip Mee Sin, Dr. Yee Jiong Sang, and Mr. Conrad Chong.

My memories on the days and nights in DSO are still fresh as if I just left DSO. For all these unforgettable memories, I thank my cheerful friends and colleges, who also took over my work responsibilities when I was away. They include, but are not limited to, Kevin Ang, Paw Yew Chai, Alvin Teng, Boyd Loh, Hong Bo, Eric Seah, Bala, and Lo Chang How.

My time at Georgia Tech wouldn't have been complete without my friends at Georgia Tech, An Vu, Keeryun Kang, and Gi Yun Chung, etc. An and I took many courses together, and we had many hours of discussion on homework and assignments. Keeryun familiarized me with the PSOPT optimal control solver, which was the very first

step for this dissertation. Gi Yun helped me with the administrative details throughout my studies, from my qualifying examination, to my thesis proposal and defense.

I would also like to thank my parents for their continuous support and my two sisters, Xuehua and Xueqin, for taking care of my parents while I am not around. Most importantly, I would like to thank my wife, Lingzhi, for all she has done for me. I can't imagine how my life would be without her.

Finally, I would like to express my appreciation to Mr. Kurt Belgum from the Language Institute at Georgia Tech, who proofread the whole dissertation and gave me many suggestions to improve the writing of this dissertation.

TABLE OF CONTENTS

LIST OF TABLES

LIST OF FIGURES

NOMENCLATURE

a	Fuel cell anode electron transfer coefficient (-)
A	Fuel cell cross-sectional area (cm^2)
A_a	Fuel cell single cell active area (cm^2)
c_0	Coefficient c_0 of transient cost model (g)
c_1	Coefficient c_1 of transient cost model (g/rad^2)
C	Fuel cell equivalent capacitance (F)
C_p	Propeller power coefficient (-)
D	UAV Drag in wind axis (N)
E	Fuel cell theoretical voltage (V)
E^0	Fuel cell theoretical voltage at standard condition (V)
E_d	Fuel cell voltage drop (V)
E_r	Fuel cell Ernest voltage (V)
F	Faraday constant (96487 cols/mole)
g	Gravitational acceleration (m/s^2)
i	Fuel cell current density (A/cm^2)
i_0	Fuel cell exchange current density (A/cm^2)
$i_{0,\mathrm{m}}$	Electric motor no load current (A)
i_{loss}	Fuel cell open circuit current losses (A/cm^2)
I	Fuel cell operating current (A)
I_m	Electric motor current (A)
I_{cell}	Fuel cell current (A)
J	Propeller moment of inertial ($kg\text{-}m^2$)
k	Geometric collocation points scale factor (-)
K_v	Electric motor constant (rad/s/V)
L_m	Inductance of electric motor (H)
m	Fuel cell concentration loss coefficient m (V)
$\dot{m}_{fuel}$	Fuel consumption rate (g/s)
m_{fuel}	Fuel consumption cost (g)

m_{fuel_t}	Transient fuel consumption cost (g)
m_{fuel_s}	Steady state fuel consumption cost (g)
M	UAV total weight (kg)
n	Fuel cell concentration loss coefficient n (cm^2/A)
N	Fuel cell number of cells (-)
N_{pop}	Population size of genetic algorithm (-)
N_{max}	Maximum iteration number of genetic algorithm (-)
p_{H_2}	Pressure of hydrogen (atm)
p_{O_2}	Pressure of oxygen (atm)
p_{H_2O}	Pressure of water vapor (atm)
p_0	Initial position (-)
p_f	Final position (-)
P_i	i^{th} waypoint (-)
Q_m	Motor torque (N-m)
Q_p	Propeller torque (N-m)
R	Universal gas constant (8.31 J/mol-K)
R_i	Fuel cell ohmic resistances per cell (ohm-cm^2)
R_m	Internal resistance of electric motor (ohm)
R	Propeller radius (m)
R_{act}	Fuel cell activation resistance (Ohm)
R_{con}	Fuel cell concentration resistance (Ohm)
R_{ohm}	Fuel cell ohmic resistance (Ohm)
R_{cross}	Crossover rate of genetic algorithm (-)
R_{mut}	Mutation rate of genetic algorithm (-)
t	Time (sec)
t_0	Initial time (sec)
t_f	Final time (sec)
T	Temperature (K)
T	Propeller thrust (N)
u_1	Heading angular rate input of the Dubins airplane model (rad/s)

u_2	Flight path angular rate input of the Dubins airplane model (rad/s)
V	UAV air speed (m/s)
V_c	Fuel cell capacitor voltage (V)
V_{in}	Input voltage to electric motor (V)
V_{out}	Output voltage from fuel cell (V)
V_m	Back EMF voltage of electric motor (V)
x, y, z	UAV positions in inertial coordinates (m)
α	UAV angle of attack (rad)
α_T	UAV thrust line angle (rad)
γ	UAV flight path angle (rad)
δ_T	Throttle input signal (-)
ΔH	Height difference (m)
ΔV_{act}	Activation voltage loss (V)
ΔV_{con}	Concentration voltage loss (V)
ΔV_{ohm}	Ohmic voltage loss (V)
η	Propeller efficiency (-)
θ	Azimuth angle of point-to-point flight path (rad)
ρ	Air density (kg/m^3)
λ_e	Fuel cell delay effect gain constant (V/A)
τ_e	Fuel cell delay effect time constant (sec)
ϕ	UAV roll angle (rad)
ψ	UAV heading angle (rad)
ψ_0	Initial heading angle (rad)
ψ_f	Final heading angle (rad)
ψ_i	UAV heading angle at ith waypoint (rad)
Ω	Propeller rotational speed (rad/s)
AFC	Alkaline Fuel Cell
BEMF	Back Electromotive Force
BLDC	Brushless Direct Current
CGL	Chebyshev-Gauss-Lobatto
CPM	Chebyshev Pseudospectral Method

DC	Direct Current
DMFC	Direct Methanol Fuel Cell
DTSP	Traveling Salesman Problem for the Dubins Vehicle
ETSP	Euclidean Traveling Salesman Problem
GC	Geometric Collocation
GFM	Generalized Framework
GPM	Gauss Pseudospectral Method
LG	Legendre-Gauss
LGL	Legendre-Gauss-Lobatto
LGR	Legendre-Gauss-Radau
LPM	Legendre Pseudospectral Method
MCFC	Molten Carbonate Fuel Cell
MDO	Multidisciplinary Design Optimization
NLP	Nonlinear Programming
PAFC	Phosphoric Acid Fuel Cell
PEM	Proton Exchange Membrane
PEMFC	Proton Exchange Membrane Fuel Cell
RPM	Radau Pseudospectral Method
SFC	Specific Fuel Consumption
SOFC	Solid Oxide Fuel Cell
SQP	Sequential Quadratic Programming
TSP	Traveling Salesman Problem
UAV	Unmanned Air Vehicle

SUMMARY

Among all the possible missions for Unmanned Air Vehicles (UAVs), reconnaissance is still ranked as the most important mission, and endurance is one of the most important performance criteria. In recent years, a new class of small-sized UAVs, powered by fuel cells, has demonstrated significant endurance improvements over the conventional gas powered UAVs of the same weight class. Along with the development of fuel cell powered UAVs, the design optimization of such UAVs has been a research focus. However, studies on the energy management of fuel cell powered UAVs in operation have been mostly limited to steady state flight conditions. Trajectory analyses of conventional gas powered UAVs, on the other hand, have been carried out extensively in the literature. The trajectory optimization for fuel cell powered UAVs can be properly addressed only if the dynamic constraints consider the dynamics of a fuel cell system. Path planning that considers the characteristics of the optimal trajectories may further improve the mission performance. In addition, if the influence of fuel cell system dynamics on mission performance can be established, fuel cell system design parameters can be optimized for different missions.

This dissertation progressively addresses the above research problems related to the trajectory optimization for fuel cell powered UAVs, from propulsion system model development, to optimal trajectory analyses and optimal trajectory applications. A dynamic model of a fuel cell powered UAV propulsion system is derived by combining a fuel cell system dynamic model, an electric motor dynamic model, and a propeller performance model. The influence of the fuel cell system dynamics on the optimal

trajectories of a fuel cell powered UAV is investigated in two phases. In the first phase, the optimal trajectories of a fuel cell powered configuration and that of a conventional gas powered configuration are compared for point-to-point trajectory optimization problems with different performance index functions. In the second phase, the influence of the fuel cell system parameters on the optimal fuel consumption cost of the minimum fuel point-to-point optimal trajectories is investigated.

This dissertation also presents two applications for the minimum fuel point-to-point optimal trajectories of a fuel cell powered UAV: three-dimensional minimum fuel route planning and path generation, and fuel cell system size optimization with respect to a UAV mission. The proposed method for minimum fuel route planning and path generation problems for a fuel cell powered UAV consists of three steps: fuel consumption cost estimation, route plan optimization with a genetic algorithm, and flight path generation with optimal trajectories. The proposed method successfully solves case study problems with different waypoint densities. In addition, an iterative method is proposed to find the optimal fuel cell system size for a given UAV mission. Case study of the fuel cell system size optimization for different missions suggests that the optimal fuel cell system sizes for different missions are expected to be different.

CHAPTER 1 INTRODUCTION

1.1 Overview

Since the first flying bomb was developed in World Word I, the capabilities of UAVs have been expanded to many areas, including intelligence surveillance and reconnaissance, communication, force protection, and signal intelligence, etc. Many of these roles have been successfully demonstrated in wars [1]. It is very common for a single type of UAV to perform multiple missions, for which different performance measures are desired. The operational aspects of UAVs have been studied in the literature with a focus on the optimal trajectories of conventional gas powered UAVs. Some of the examples are minimum fuel loitering trajectories, obstacle avoidance trajectories, minimum time travel trajectories, and maximum target tracking trajectories.

In recent years, a new type of UAVs powered by fuel cell systems has demonstrated significant endurance improvements due to the low fuel consumption rates of fuel cell systems. Since fuel cell powered UAVs are relatively new, their operational aspects have not been well addressed in the literature. The immediate question is whether studies on the optimal trajectories of conventional gas powered UAVs are still applicable to fuel cell powered UAVs. If the studies for conventional gas powered UAVs are not applicable to fuel cell powered UAVs, how can we investigate the optimal trajectories of fuel cell powered UAVs? What are the differences between the optimal trajectories of a fuel cell powered UAV and that of a convention gas powered UAV? How can we apply the optimal trajectories in mission planning and path generation problems? Can we bring

the influence of fuel cell system dynamics to the mission level so that the fuel cell system design parameters can be optimized for a given mission?

To address these questions regarding the trajectory optimization for fuel cell powered UAVs, the following sections of this chapter present a literature review on related research, beginning with an introduction to fuel cells and fuel cell powered UAVs. A survey on research activities on fuel cell powered UAVs summarizes the current state of the art in research areas related to fuel cell powered UAVs. A review of fuel cell performance models and dynamic models then identifies the appropriate models to be used in this dissertation. A review on the trajectory optimization for conventional gas powered UAVs reviews different formulation methods and different trajectories that have been studied in the literature. Next, a review of numerical methods for optimal control problems determines the appropriate method for solving trajectory optimization problems.

The research objectives of this dissertation focus on trajectory optimization for fuel cell powered UAVs, from propulsion system model development, to optimal trajectory analysis and optimal trajectory applications. A dynamic model of a fuel cell powered UAV propulsion system is developed to facilitate the trajectory optimization study for a fuel cell powered UAV considering the fuel cell system dynamics. Subsequently, the optimal trajectories of a fuel cell powered UAV are investigated by comparing the optimal trajectories of a fuel cell powered configuration and that of a conventional gas powered configuration. Finally, this dissertation presents two applications of the minimum fuel point-to-point optimal trajectories: three-dimensional minimum fuel route planning and path generation, and fuel cell system size optimization.

1.2 Literature Review

1.2.1 Introduction to Fuel Cells

A fuel cell operates like a battery by converting chemical energy to electricity, but it differs from a battery in a number of ways [2]. The most significant difference is where the chemical energy is stored. With batteries, the chemical energy is stored in the substances inside the batteries. When all the stored chemical energy is converted to electrical energy, the batteries must be thrown away or recharged. With a fuel cell, on the other hand, the chemical energy is stored outside of the fuel cell. The electrical energy can be continuously generated as long as the fuel cell is supplied with the fuel and oxidant. The inputs and outputs of a fuel cell are illustrated in Figure 1.1.

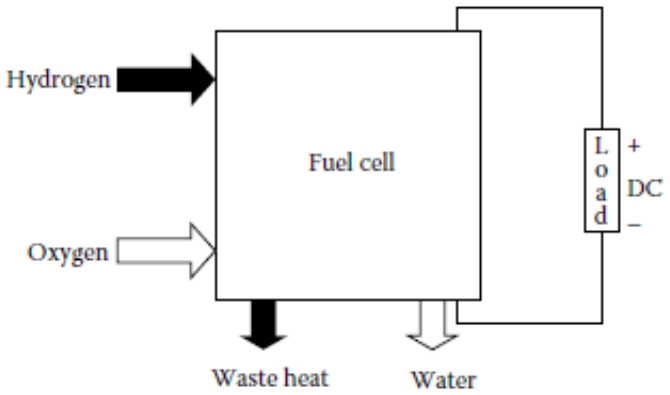

Figure 1.1 A fuel cell's inputs and outputs [3].

A fuel cell and electric motor pair is similar to a conventional reciprocating engine. Both are converting chemical energy to mechanical energy. One of the main differences is that the generation of electricity in a fuel cell does not involve very high temperatures. The Carnot efficiency of a heat engine does not apply to a fuel cell [4].

Hence the efficiency of a fuel cell with an electric motor is higher than that of a conventional reciprocating engine.

Many types of fuel cells have been developed since the creation of the first fuel cell prototype by W.R. Grove in 1839 [4]. Due to the differences in the electrolytes and fuel types that have been used, fuel cells can be categorized as shown in Table 1.1 [5]. Proton exchange membrane fuel cells (PEMFC) are primarily used for automotive power generation. Direct methanol fuel cells (DMFC) are used mainly for portable power generation. Alkaline fuel cells (AFC) were developed for the space programs to produce electricity and drinking water. Phosphoric acid fuel cells (PAFC), molten carbonate fuel cells (MCFC) and solid oxide fuel cells (SOFC) are often seen in stationary power applications.

Among the many types of fuel cells, the proton exchange membrane (PEM) fuel cells are most commonly used in the aerospace industry. The first version of a PEM fuel cell rated at 1kW was developed by General Electric for the Gemini spacecraft program in the early 1960s [6]. However, in subsequent space flights, AFCs were used due to the fact that the membrane of the PEM fuel cells at that time was not stable enough for the desired power density. The breakthrough for PEMFC happened in the 1980s, when the perfluorinated sulfonic acid polymer, Nafion, was used as the electrolyte [7]. The chemical stability of Nafion greatly exceeded that of the previously known membranes. In recent years, due to the high demand and investment in clean energy, the specific power of PEM fuel cells has achieved up to 600-800 mW/cm^2 and the lifetime is now several tens of thousands of hours [8]. Zero-emission vehicle prototypes powered by PEM fuel cells have been developed by many leading car manufactures [9,10].

Table 1.1 Characteristics of the important fuel cells [5].

	PEMFC	DMFC	AFC	PAFC	MCFC	SOFC
Primary Applications	Automotive and stationary power	Portable power	Space vehicles and drinking water	Stationary power	Stationary power	Vehicle auxiliary power
Electrolyte	Polymer (plastic) membrane	Polymer (plastic) membrane	Concentrated (30-50%) KOH in H_2O	Concentrated 100% phosphoric acid	Molten Carbonate retained in a ceramic matrix of $LiAlO_2$	Yttrium-stabilized Zirkondioxide
Operating temperature	50-100 ^oC	0-60^oC	50-200 ^oC	150-200 ^oC	600-700 ^oC	700-1000 ^oC
Charge carrier	H^+	H^+	OH^-	H^+	$CO_3^=$	$O^=$
Primary cell components	Carbon-based	Carbon-based	Carbon-based	Graphite-based	Stainless steel	Ceramic
Catalyst	Platinum	Pt-Pt/Ru	Platinum	Platinum	Nickel	Perovskites
Primary fuel	H_2	Methanol	H_2	H_2	H_2, CO, CH_4	H_2, CO
Start-up time	Sec-min	Sec-min		Hours	Hours	Hours
Power density (kW/m^3)	3.8-6.5	~0.6	~1	0.8-1.9	1.5-2.6	0.1-1.5
Combined cycle fuel efficiency	50-60%	30-40%	50-60%	55%	55-65%	55-65%

Figure 1.2 shows the critical components of a PEM fuel cell, which consists of gas flow channels, gas diffusion layers, catalyst layers and electrolyte layers [3]. The gas flow channels provide the guided flow of hydrogen and oxygen. On the anode side of the fuel cell, hydrogen molecules travel through the gas diffusion layer by pressure gradient and concentration differences. At the interface between the catalyst layer and the electrolyte layer, the hydrogen molecules are broken into protons and electrons. Electrons travel through the external circuit, which effectively generates electricity. The protons travel through the electrolyte layer and arrive at the cathode side catalyst layer. Similar to what happens on the anode side, oxygen molecules travel through the cathode side gas

diffusion layer and arrive at the catalyst layer. On the cathode side, a catalyst layer, protons, electrons, and oxygen molecules form water molecules.

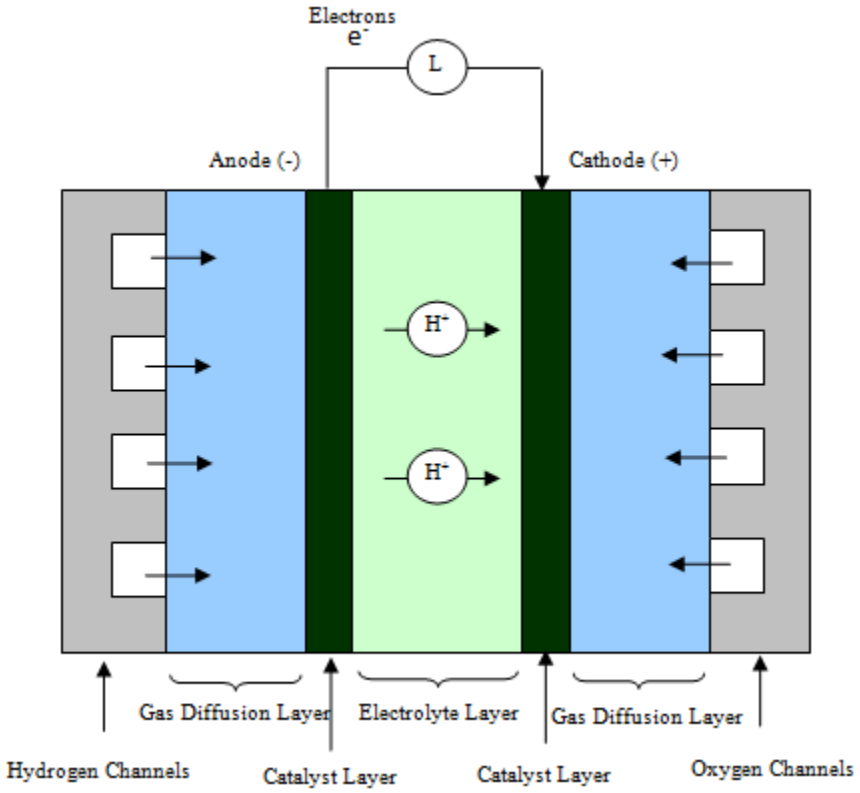

Figure 1.2 The schematics of a PEM fuel cell.

1.2.2 Fuel Cell Powered UAV Prototypes

With many successful applications of PEM fuel cells in the automotive industry, researchers in the aerospace industry started to equip UAVs with PEM fuel cells. The first fuel cell powered UAV prototype was designed by AeroVironment and Lynntech in 2003 [11]. As shown in Figure 1.3, the Hornet weighted only 6 ounces, and its wing span was 15 inches. The incorporation of the fuel cell system as the power plant was designed to double the endurance, but during the flight test, the Hornet was able to fly for only about 5 minutes. The difference between the achieved endurance and the potential

endurance of the Hornet suggested the need for additional research on fuel cell powered UAVs at that time.

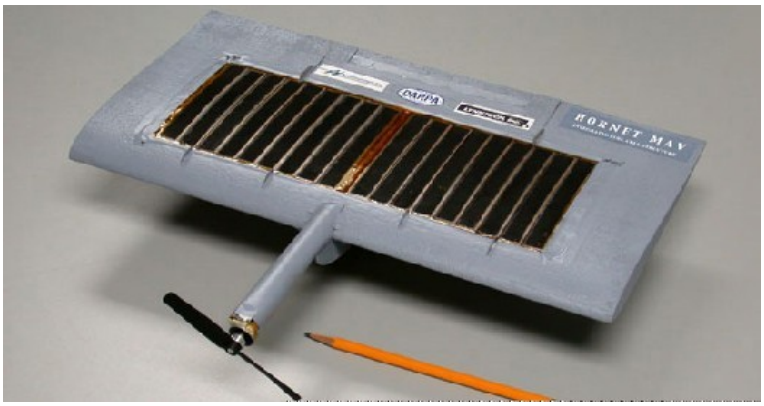

Figure 1.3 AeroVironment Hornet fuel cell UAV[12].

Since 2003, many groups have been involved in the development of fuel cell powered UAVs. Several prototypes have demonstrated superior flight endurances over conventional gas or battery powered UAVs in the same weight class. In 2007, AeroVironment equipped the Puma UAV with PEM fuel cells and achieved nearly five hours of flight endurance. That was double the flight time for the same airframe with standard rechargeable batteries [13]. In 2009, the first commercial fuel cell powered UAV, named Boomerang, was showcased at the AUVSI exhibition in Washington by BlueBird Aero Systems [14]. The Boomerang weighed only 9 kg and flew for more than nine hours. The fuel cell pack, named Aeropak, was from the Horizon Fuel Cell Technologies. The same fuel cell pack was used by the Israel Aerospace Industries on the Birdeye 650, which extended the flight endurance to 6 hours, which was more than double its endurance with the lithium batteries [15]. In November 2009, the Ion Tiger from Naval Research Laboratory achieved a flight endurance of 26 hours [16]. The Ion Tiger, which weighed approximately 17 kg, was equipped with a 550W PEM fuel cell

propulsion system from Protonex. The 26-hour flight endurance significantly outperformed the flight endurances demonstrated by previous small UAVs. In August 2011, the Faucon H_2 UAV, from EnergyOr, achieved 10 hours of flight endurance, which once again demonstrated the endurance advantage of fuel cell powered UAVs [17]. The key specifications of the above fuel cell powered UAVs are summarized in Table 1.2.

Table 1.2 Fuel cell powered UAV prototypes.

Company	UAV	Endurance (hr)	Gross Weight (lb)	Fuel Cell Power (W)	Wingspan (m)	Year
AeroVironment	Puma	9	5.7	-	2.6	2008
BlueBird Aero Systems	Boomerang	9	9	200	2.75	2009
Naval Research Laboratory	Ion Tiger	26	16.8	550	5.2	2009
Israel Aerospace Industries (IAI)	Birdeye 650 LE	6	11	200	3	2010
EnergyOr Technology	Faucon H2	10	9	210	3	2011

1.2.3 Research Activities on Fuel Cell Powered UAVs

Although the long endurances of fuel cell powered UAVs have been realized only in recent five years, the conceptual design study of fuel cell powered UAVs can be traced back to the 1980s. In 1984, NASA Langley Research Center published a preliminary performance analysis and conceptual design of an unmanned airplane with multi-day endurance capability [18]. In the conceptual design, a mixed-mode electric power system was proposed with solar cells for daytime flight and fuel cells for nighttime flight. Based on the fuel cell technology at that time, the conceptual design study led to a class of airplanes with very low wing loadings and relatively long wing spans.

With many successful applications of the PEM fuel cells in the automotive industry, the conceptual designs of fuel cell powered UAVs in the 2000s were much closer to realization. In 2003, Jeffery conducted an analytical feasibility and performance assessment of a fuel cell powered small electric airplane based on the MCR-01 two-seater plane [19]. The results indicated that the flight with an off-the-shelf fuel cell may be possible with reduced speed, climb rate, range, and payload-carrying capabilities. Jeffery also highlighted the need for advanced fuel cell technology to achieve comparable reciprocating engine aircraft performance. In the same year, researchers at Boeing Research & Technology - Europe initiated a fuel cell demonstrator design with a fuel cell/battery hybrid configuration [20]. A battery was needed for startup and takeoff assistance. The Boeing fuel cell demonstrator was completed in 2007, and flight was demonstrated in 2008 [21].

With the advancement of the fuel cell technology, researchers started to investigate the integrated design optimization of fuel cell powered UAVs. Among them, researchers from Georgia Tech contributed a series of papers on the multi-disciplinary design optimization of fuel cell powered UAVs [22,23,24]. They proposed a design method that optimized the design variables with respect to aircraft performance metrics. The mapping from the design variables to the aircraft performance metrics was based on subsystem level contribution analyses, in which empirical and physics-based models were used to model the subsystems. The design uncertainties were further reduced when the contribution analyses with significant contribution to the performance metrics were validated through the experimental data. To validate the design methodology, the Georgia

Tech researchers constructed and flight tested the Georgia Tech fuel cell aircraft demonstrator in 2008 [25].

To improve the performance of fuel cell powered UAVs, many researchers have proposed a hybrid power system, in which both fuel cells and batteries are used for propulsion [26]. Fuel cells are known for high energy density and low power density. Batteries, on the other hand, have the properties of low energy density and high power density. The idea of hybridization allows the energy demand and power demand to be separated. Ref. [27] investigated the effect of such hybridization on the flight performance in a simulation, and concluded that the use of a fuel cell - battery hybrid system did not improve the endurance of a fuel cell powered UAV if the fuel cell system alone was sufficient to meet the power requirement. Ref. [27] also claimed that the only benefit of the hybrid power system was to decouple the design requirements of a climb flight from those of a cruise flight.

For conventional gas powered UAVs, researchers have realized that using a periodic flight path pattern can improve the endurance performance as compared to using a steady-state flight path pattern [28]. Ref. [29] confirmed this possibility for UAVs in a constant wind in 2009, in which the optimal periodic flight path was partitioned into a boost arc and a coast arc. Ref. [27] evaluated the same flight path pattern on a fuel cell powered UAV to maximize the flight endurance, which claimed that the optimal flight path for endurance was a steady level flight and that there wasn't any benefit for a fuel cell powered UAV to fly in the periodic boost-coast flight path pattern. It seemed that trajectory optimization for a fuel cell powered UAV was not required. However, in real applications, many different flight paths other than steady state level flight are required to

complete a flight mission. In addition, the dynamics of a fuel cell system on the optimal trajectories was not considered in [27]. The trajectory optimization for a fuel cell powered UAV can be appropriately addressed only if the dynamic constraints include the dynamics of a fuel cell system.

1.2.4 Fuel Cell Performance Models

The performance of a fuel cell is represented by its polarization curve, which is also known as a voltage-current curve. Figure 1.4 shows the potential losses of a typical fuel cell as a function of the current density, where the major potential losses are illustrated [30]. The role of a fuel cell performance model is to accurately predict these potential losses. Since the research scope of this dissertation concerns only PEM fuel cells, only performance models for PEM fuel cells are discussed in this section.

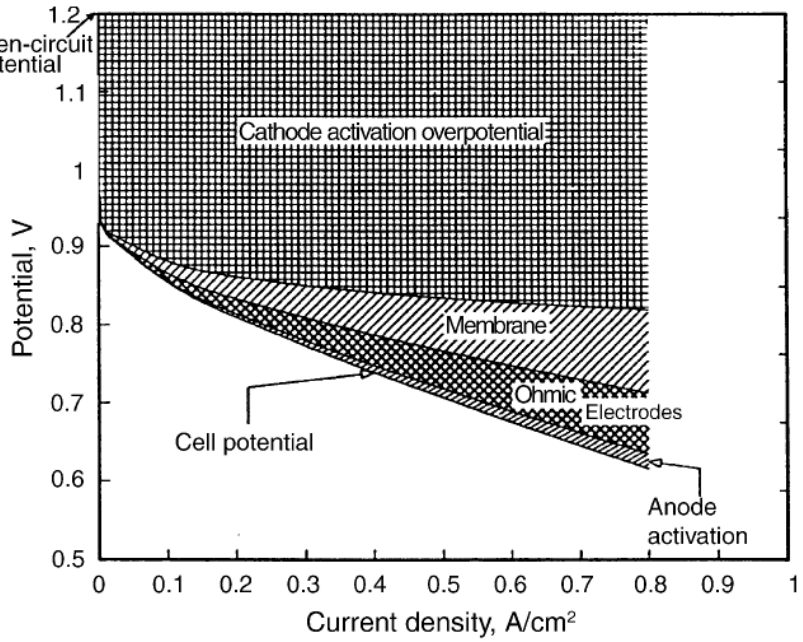

Figure 1.4 Fuel cell potential losses as a function of current density [30].

While reviewing the approaches to PEM fuel cell modeling, Ref. [31] categorized PEM fuel cell models into three categories: analytical models, semi-empirical models, and mechanistic models. Ref. [32] presented an analytical fuel cell model, using an equivalent electric circuit with simple mathematics. In this model, the voltage current relationship is valid only within a limited operation range. Semi-empirical models were also developed by combining the theoretically derived equations with the empirically determined relations [31]. For example, the equations in [5] used theoretical relations for the activation losses and the ohmic losses, and an empirical relation for the concentration losses.

The mechanistic models of PEM fuel cells can be further classified into two categories based on the computation scope of the model [33]. The first type of model deals only with a specific part of fuel cells. This model is good for representing the details within that particular part of a fuel cell. The second type of model includes all the parts of a fuel cell, where all the potential losses at different current densities can be obtained. Depending on the level of complexity, this type of models ranges from one-dimensional to three-dimensional and from single phase to two-phase [33]. Figure 1.5 illustrates the three dimensions within a fuel cell gas flow channel. In a one-dimensional model, gas properties are uniform in the flow channels. Only gas diffusions across the x-direction are modeled. In a two-dimensional model, gas properties are non-uniform along the flow channel direction (y-direction). In a three-dimensional model, gas properties in the cross direction (z-direction) of the gas flow channel are non-uniform. The terms "single phase" and "two-phase" refer to the forms of water in the gas mixtures. In a

single phase model, water is either in liquid form or in vapor form. In a two-phase model, water is in both liquid and vapor forms.

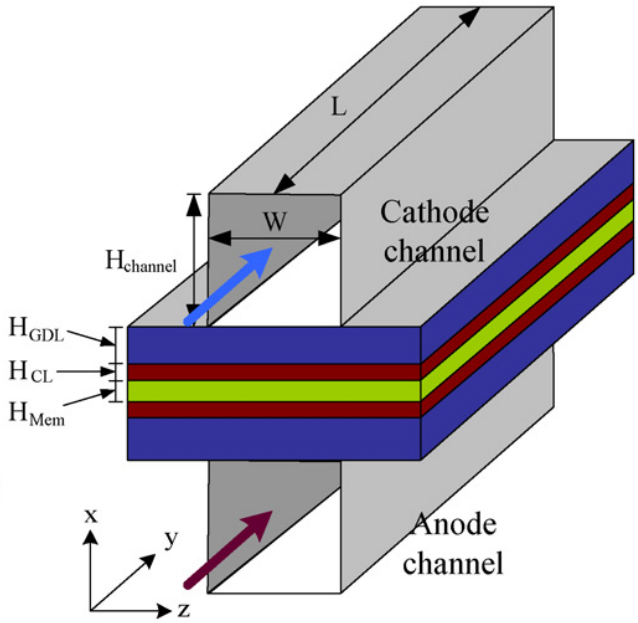

Figure 1.5 Schematic diagram of a three-dimensional fuel cell model [34].

Ref. [30] developed one of the earlier one-dimensional fuel cell models, in which they derived coupled differential equations to model the species transport, gas-phase transport and electrochemical relations. The results showed that this one-dimensional model could predict the fuel cell performance in the low and intermediate current density region. Further improvements have been achieved by the development of two-dimensional and three-dimensional fuel cell models. Although three-dimensional models are capable of capturing the full picture of the gas properties in the gas flow channels, commercial software packages are often required to solve the coupled equations [35].

This dissertation uses the semi-empirical fuel cell performance model discussed in [36] to develop the dynamic model of a fuel cell powered UAV propulsion system. Compared to analytical models, the semi-empirical model can predict the fuel cell

performance in a wide operating range. Unlike mechanistic models, the semi-empirical model does not require iterative procedures.

1.2.5 Fuel Cell Dynamic Models

Although the performance model of a fuel cell is capable of determining the steady state voltage-current relation, it fails to capture the transient behavior under load variations. Depending on the different requirements, a dynamic model of a fuel cell may include various transient effects such as the double-layer charging effect, the fuel cell delay effect, and the temperature effect.

The double-layer charging effect of a fuel cell is similar to a capacitor effect, which is when positive and negative charges gather on two opposite plates [37]. In a fuel cell (Figure 1.2), the membrane allows only protons to pass and electrons reach the cathode through an external circuit. Across the boundary of the cathode and the membrane, two charged layers are formed by protons and electrons, which behave like a capacitor. The double-layer charging effect is modeled with an equivalent capacitor coupled with equivalent resistors, as shown in Figure 1.6. Based on the equivalent electric circuit model, the transient voltage of a fuel cell exhibits a first order delay when the current density is changed. The double-layer charging effect was considered in the fuel cell dynamic models in [37,38,39].

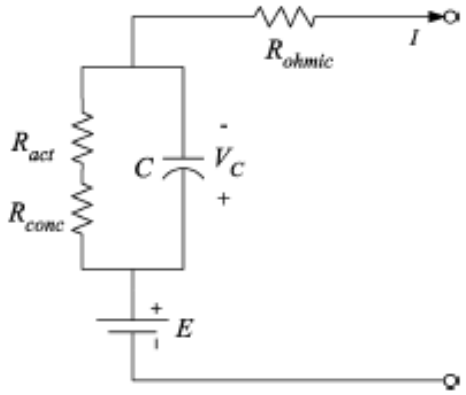

Figure 1.6 Equivalent electric circuit of the double-layer charging effect [37].

The fuel cell delay effect is caused by the delay between the change in the load current and the flow of the fuel and oxidant [37]. When there is a sudden change in the load current, additional protons are required to travel through the membrane layer. But hydrogen and oxygen molecules take time to travel from the gas flow channels to the electrolyte layers. The delay is due to the transport process of the protons, hydrogen, oxygen, water vapor, and liquid water through the fuel cell membranes. Fuel cell dynamic models that include this effect are found in [37,40].

Another important parameter that affects the dynamics of a fuel cell is temperature. The temperature dynamics are derived based on the energy balance of a fuel cell as net heat gain or loss results in temperature increase or decrease. As indicated in the Nernst Equation [3], the temperature affects the amount of Gibbs energy that is available for converting into electrical energy. Hence, the fuel cell voltage drops as the temperature increases. However, the effect of rising temperature on the fuel cell voltage is dominated by the reduction on the activation resistance, resulting in improved fuel cell performance [4,41]. Fuel cell dynamic models that include the temperature effect can be found in [37,42,43].

Among the various dynamic effects of a fuel cell, the double-layer charging effect mainly affects the fuel cell transient responses in the short-time range. This effect is similar to a capacitor in an electric circuit, where the short-time energy buffer smoothes the voltage ripples due to load variations. When the load of a fuel cell is increased suddenly, the delay in the fuel and oxidant results in a sudden voltage dip. The voltage recovers from the dip once the fuel and oxidant flows reach the steady states. Among the above transient effects, the temperature effect is the slowest. As the current loading increases, the temperature of a fuel cell increases, resulting in additional voltage being recovered due to the reduction in activation losses. These dynamic effects can be seen in Figure 1.7 from [44], which shows the measured transient voltage of a fuel cell when the current increases from one level to another level.

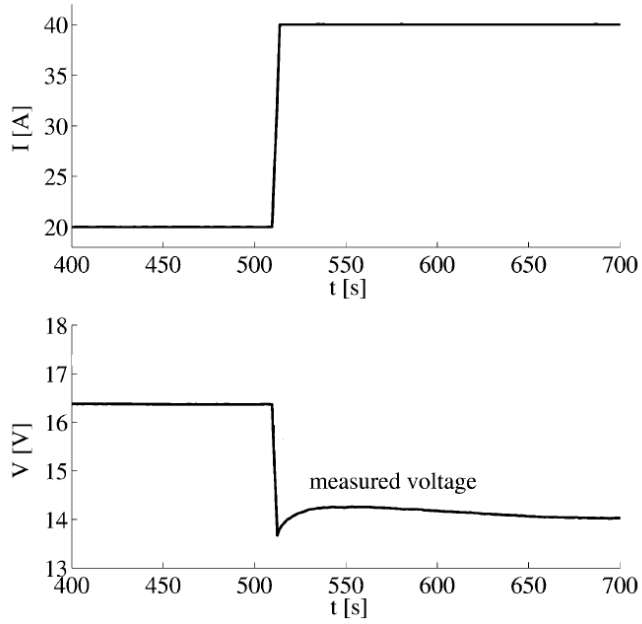

Figure 1.7 Measured transient voltage during a current step [44].

When deriving the dynamic model for a fuel cell powered UAV propulsion system, this dissertation assumes that the temperature is constant. This assumption is based on the fact that many commercial fuel cell systems use closed-loop controllers to regulate the fuel cell temperature. The double-layer charging effect and the fuel cell delay effect are included in the fuel cell dynamic model.

1.2.6 Trajectory Optimization for UAVs

A trajectory optimization problem, also known as an optimal control problem, can be stated as follows [45]: "Determine the control signals that will cause a system to satisfy the physical constraints and, at the same time, minimize (or maximize) some performance criterion." In a trajectory optimization problem, variables are separated into two classes, state variables and control variables. The evolutions of state variables are determined by the control variables through a set of differential equations, which represent the dynamics of the physical system. The solution of a trajectory optimization problem is the control variables that minimize (or maximize) the performance criterion and that satisfy the dynamic equations and other constraints.

Applications of optimal control to UAVs for trajectory optimization are essentially the formulation of the performance criterion and the derivation of the dynamic equations. Depending on different objectives, various performance criteria and UAV dynamic equations have been explored in the literature. In [46], the optimal trajectories of UAVs to avoid multiple radars were studied, and the UAV dynamic model was a simple 2-D planar point mass model with the heading variation only. In [47], optimal control problems with a similar 2-D UAV dynamic mode were formulated to find the optimal waypoints and control sequences to avoid threats and obstacles. A 2-D point mass

kinematics model including the target motion dynamics was used in [48], in which the optimal trajectories for tracking various types of targets were obtained. A more sophisticated six-state point mass UAV model including three positions, velocity, flight path angle, and heading angle was derived in [49] to investigate the optimal trajectories for extracting energy from downdraft. Similar point mass UAV models were used to investigate various trajectory optimization problems in [50,51,52,53].

Trajectory optimization problems for UAVs are classified as periodic or non-periodic depending on the time domain of the problem. In a periodic trajectory optimization problem, the initial states and the final states are identical. The performance criteria of such problems are usually time-averaged values. This type of problem formulation is mostly for loitering trajectories. Examples of periodic problems are found in [49,50]. In a non-periodic trajectory optimization problem, some or all of the initial states and the final states are different. This type of problem formulation is often applied to point-to-point travel trajectories. Examples of such a problem are found in [46,47,54].

Depending on different mission objectives, trajectory optimization problems can be formulated for obstacle avoidance, target tracking, minimum time, and minimum fuel, etc. In some applications, dynamic equations or performance indices do not include the propulsion system characteristics. Results obtained in these studies are applicable to any type of UAV. In other applications, the propulsion system characteristics are embedded in the dynamic equations or the performance indices, and the optimal trajectories are strongly influenced by the propulsion system characteristics. The optimal trajectories to avoid multiple radars obtained in [46] and the optimal trajectories to track moving or stationary targets obtained in [48] are not influenced by the propulsion system

characteristics. The minimum fuel periodic loitering trajectories for a jet engine aircraft obtained in [50], on the other hand, are highly influenced by the specific fuel consumption curve. Although the optimal flight patterns for extracting energy from downdraft to enhance endurance for a jet engine powered aircraft and a propeller powered aircraft obtained in [49] are similar, the corresponding engine activities are different.

As compared to a conventional gas powered UAV propulsion system, a fuel cell powered UAV propulsion system is different in the transient response delay and the specific fuel consumption curve. The delay in the transient response is expected to influence the transient trajectories of a fuel cell powered UAV. The specific fuel consumption curve is expected to influence the minimum fuel optimal trajectories, but exactly how the optimal trajectories are influenced by the characteristics of the fuel cell system has not been addressed in the literature.

1.2.7 Numerical Methods for Optimal Control Problems

Numerical methods are widely used to solve optimal control problems, which can be classified into two main categories: direct methods and indirect methods [55]. In an indirect method, the optimal control problem is converted to a two-point boundary value problem by applying the calculus of variations and Pontryagin's minimum principle [56]. The resulting boundary value problem is then solved by numerical methods. In a direct method, the optimal control problem is transcribed directly to a nonlinear programming (NLP) problem. The resulting NLP problem is then solved numerically by NLP solvers. The direct methods have the advantage that the first order necessary conditions do not

need to be derived. They also have larger radii of convergence than the indirect methods, which do not require a good initial guess [57].

The direct methods can be further classified into different categories based on the quantities (controls or/and states) to be discretized. Two common categories of direct methods are control parameterization and state and control parameterization [58]. In a control parameterization method, the control variables are approximated and the dynamic control equations are solved by numerical integration. A shooting method is one example of control parameterization. In a state and control parameterization method, both the state and control variables are approximated. The dynamic equations are converted to algebraic constraints at the discretized nodes. Most pseudospectral methods are categorized as state and control parameterizations.

The differences between pseudospectral methods and other state and control parameterization methods are the choices of the basis functions used for parameterization. Since the interpolation basis functions are orthogonal at the collocation points, the pseudospectral methods are also referred to as orthogonal collocation methods [59]. In a pseudospectral method, a finite basis of interpolating polynomials is used to approximate the state and control trajectories at a set of collocation points. The dynamic constraints are approximated by the time derivative of the approximating polynomials, resulting in a set of algebraic constraint equations. Similarly, the integration cost is also approximated by integrating the approximation polynomials. The main advantage of the pseudospectral methods is that the approximation of the derivatives and the integrations for smooth functions exhibit spectral accuracy [60].

In the literature of the pseudospectral methods for optimal control, several well-known pseudospectral methods have been developed: the Chebyshev pseudospectral method [61], the Legendre pseudospectral method [62], the Radau pseudospectral method [63] and the Gauss pseudospectral method [64]. Among these methods, the Legendre pseudospectral method is the most well-established method with several convergence theorems. The Radau and Gauss pseudospectral methods, which are extensions of the Legendre pseudospectral method, replace the Legendre-Gauss-Lobatto points with Legendre-Gauss-Radau points and Legendre-Gauss points, respectively.

Some examples of software packages based on pseudospectral methods are PSOPT [65], GPOPS [66], which are open source software packages, DIDO [67], and SOCS [68] . PSOPT is an optimal control package written in C++ that uses the Legendre pseudospectral method. The compatible NLP solvers are IPOPT and SNOPT. The IPOPT solver is an open source C++ implementation of an interior point nonlinear programming method [69]. The SNOPT solver is a proprietary large scale NLP solver that uses a sequential quadratic programming (SQP) algorithm [70]. GPOPS, (General Pseudospectral Optimization Software) is a software program, written in MATLAB, for solving multi-phase optimal control problems using the Radau pseudospectral method. Similar to PSOPT, GPOPS also uses the SNOPT solver to solve transcribed NLP problems.

An indirect method would be very difficult to implement when solving the trajectory optimization problems for fuel cell powered UAVs since there are many nonlinear relations in the dynamic equations. Among different direct methods, pseudospectral methods are well-known for their approximation accuracy at relatively

fewer grid points. In this dissertation, different pseudospectral methods are implemented with one generalized framework to transcribe optimal control problems into nonlinear programming problems. The SNOPT solver is used to solve the transcribed NLP problems. The trajectory optimization problems studied in this dissertation are solved by the generalized framework.

1.3 Research Objectives

The research objectives stated in this section are progressively staged to investigate the trajectory optimization for fuel cell powered UAVs, from model development, to optimal trajectory analysis, to optimal trajectory applications.

Research Objective 1: To derive a dynamic model of a fuel cell powered UAV propulsion system that can be used for the study of trajectory optimization for a fuel cell powered UAV.

A fuel cell system, as a propulsion power source, has its own dynamic behavior. For this research, the dynamic model of a fuel cell powered UAV propulsion system is developed by combining a dynamic model of a fuel cell system, a dynamic model of an electric motor, and a performance model of a fixed-pitch propeller. The developed model is used to determine the influence of the fuel cell system parameters on the effective time constants and the step command responses. It is also used to study the optimal trajectories of fuel cell powered UAVs.

Research Objective 2: To understand the differences between the point-to-point optimal trajectories of a fuel cell powered UAV and those of a conventional gas powered UAV.

As optimal trajectories are often used for mission planning and path planning, it is beneficial to understand the differences between the optimal trajectories of a fuel cell powered UAV and those of a conventional gas powered UAV. Since the specific fuel consumption curve of a fuel cell system is different from that of a reciprocating engine, the minimum fuel optimal trajectories of a fuel cell powered UAV are expected to be different from those of a conventional gas powered UAV. First, trajectory optimization problems with different performance index functions are formulated for a fuel cell powered configuration and a conventional gas powered configuration. After this, the optimal trajectories of these two configurations are compared to understand the characteristics of the optimal trajectories of a fuel cell powered UAV.

Research Objective 3: To develop a method for three-dimensional minimum fuel route planning and path generation problems for a fuel cell powered UAV.

One of the goals of trajectory optimization is to assist the mission planning and/or path planning. Current mission planning methods for UAVs either do not consider the characteristics of the UAV propulsion system, or they are formulated based on the conventional gas powered UAV propulsion system. In this dissertation, significant differences between the optimal trajectories of a fuel cell powered UAV and those of a conventional gas powered UAV are observed in the minimum fuel point-to-point optimal trajectories. A method for three-dimensional minimum fuel route planning and path generation problems for a fuel cell powered UAV, considering the characteristics of minimum fuel optimal trajectories, is expected to generate a route plan and flight path that is both dynamically feasible and fuel optimal.

Research Objective 4: To develop a design optimization method that can bring the influence of the fuel cell system dynamics on UAV performance to the mission level so that the fuel cell system design parameters can be optimized for a given mission.

Design optimizations for a given UAV mission are often formulated with steady state performance measures. In this research, the influence of a fuel cell system on the optimal trajectories is observed in both steady state segments and transient segments. The fuel cell system dynamics are expected to influence the UAV performance at the mission level. If the relations between the fuel cell system design parameters and the mission performance can be established, the fuel cell system can be optimized with respect to a given mission.

1.4 Organization of Dissertation

This chapter (Chapter 1) reviews the literature related to fuel cells, fuel cell powered UAVs, and trajectory optimization for UAVs. The research objectives address the research gaps associated with trajectory optimization for fuel cell powered UAVs, from dynamic model development, to optimal trajectory analysis, to optimal trajectory applications.

Chapter 2 derives the dynamic model for a fuel cell powered UAV propulsion system, which is the combination of a fuel cell system, an electric motor, an electric motor controller, and a fixed-pitch propeller. The derived model is used to model both the steady state performance and the transient performance. Parametric studies then determine the influence of fuel cell system parameters on the effective time constants and step command responses.

In Chapter 3, a fuel cell powered UAV configuration is obtained by modifying the Aerosonde UAV with a properly sized fuel cell system. The conventional gas powered reciprocating engine, the conventional gasoline fuel, and the conventional fuel tank of the original configuration is replaced with a fuel cell system, an electric motor, compressed hydrogen, and a compressed hydrogen tank. The gross weight of the fuel cell powered configuration is the same as that of the conventional gas powered configuration. The performance of the fuel cell powered configuration is evaluated and compared to that of the conventional gas powered configuration.

Chapter 4 proposes a generalized framework for pseudospectral methods to transcribe an optimal control problem to a nonlinear programming (NLP) optimization problem for any given set of collocation points. With this framework, different pseudospectral methods are compared with one NLP solver for a number of example optimal control problems. In addition, the proposed framework is used to evaluate a new pseudospectral method with a new set of collocation points.

In Chapter 5, the influence of the fuel cell system on the optimal trajectories of a fuel cell powered UAV is investigated in two phases. In the first phase, the point-to-point optimal trajectories of the fuel cell powered configuration and that of the conventional gas powered configuration are compared by using different performance index functions. In the second phase, the optimal fuel consumption costs of the minimum fuel point-to-point optimal trajectories with different fuel cell system parameters are compared.

Chapter 6 proposes a method to solve three-dimensional minimum fuel route planning and path generation problems as an application of the minimum fuel point-to-point optimal trajectories of a fuel cell powered UAV. The proposed method consists of

the development of a minimum fuel cost model, the implementation of a genetic algorithm for route planning, and the generation of the optimal path with optimal trajectories.

In Chapter 7, an iterative method is proposed to optimize the fuel cell system size parameters, in other words, the number of cells and the cell area, for a given mission. With the fuel consumption cost model, the proposed method considers both the steady state cost and the transient cost associated with the optimal flight trajectories. At the end of the design optimization process, both the optimal fuel cell system size and the optimal route plan are determined for a given mission.

Chapter 8 presents conclusions drawn from this dissertation, a summary of original contributions, and recommendations for future work.

CHAPTER 2

DYNAMIC MODEL OF A FUEL CELL POWERED UAV PROPULSION SYSTEM

2.1 Introduction

When a fuel cell system is used to provide the propulsion power to a UAV, it is connected to an electric motor and a propeller. The connection between the fuel cell, electric motor, and propeller is similar to that of a battery powered UAV, which is shown in Figure 2.1 [71]. To allow the variation of the propeller rotational speed, a control signal (5) is fed to the speed controller (3). Depending on the control signal, a different amount of voltage from the battery (4) is applied to the electric motor (2) through the speed controller. With voltage applied to the electric motor, the electrical energy is converted into mechanical energy to rotate the propeller (1). The fuel cell powered UAV propulsion system discussed in this dissertation is a UAV propulsion system that consists of a fuel cell system, an electric motor, an electric motor controller, and a fixed-pitch propeller.

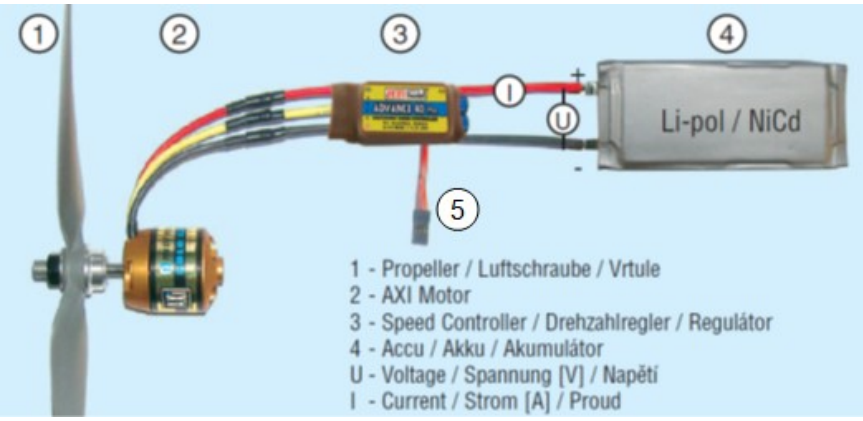

Figure 2.1 A battery powered UAV propulsion system [71].

In this chapter, the dynamic model of a fuel cell powered UAV propulsion system is developed by combining the dynamic model of a fuel cell system, the dynamic model of an electric motor, and the performance model of a fixed-pitch propeller. The dynamic model of a fuel cell system models both the steady state performance and the transient performance of a fuel cell system. The steady state performance model is a semi-empirical model, which uses equations from both theoretical relations and experimental observations. The dynamic model includes two dynamic effects: the double-layer charging effect and the fuel cell delay effect. As the influence of the gas pressure variables on the fuel cell voltage is insignificant, these variables are reduced to steady state variables. In addition, the transient characteristics of a fuel cell powered UAV propulsion system are studied in the form of effective time constant and step command responses with the derived dynamic model.

2.2 Dynamic Model of a Fuel Cell System

As fuel cells are the most critical subjects to be studied in this dissertation, their unique characteristics need to be clearly understood. This section explains all the fundamental principles and details of a fuel cell that are needed to study the trajectory optimization for a fuel cell powered UAV. Fundamentals to a fuel cell are the aspects of electrochemistry and energy conversion. The steady state fuel cell performance curve represents the relation between the current density and voltage when a fuel cell is operating in steady states. This relation includes the energy loss that occurs when a fuel cell is used in an electric circuit to supply power. The dynamic model simulates the transient behavior of a fuel cell, which are critical when analyzing their influence on the UAV's transient

responses. A fuel cell dynamic model can be simplified by reducing some insignificant fuel cell states to steady states.

2.2.1 Fundamentals of PEM Fuel Cells

Chapter 1 introduced the basic operation principle of a fuel cell. In this section, the energy conversion aspect of a PEM fuel cell is explained. As shown in Figure 2.2, the PEM fuel cell is fed with hydrogen at the membrane's anode side and oxygen at the membrane's cathode side. The catalyst at the anode causes the hydrogen atoms to release their electrons and become H^+ ions (protons).

$$H_2 \rightarrow 2H^+ + 2e^- \tag{2.1}$$

The core of a PEM fuel cell, the proton exchange membrane (PEM), allows only protons to pass through. The electrons have to travel to the cathode through the external circuit. The travel of these electrons from the anode to the cathode realizes the generation of electricity. On the cathode side, H^+ ions, electrons, and oxygen molecules form water with the following reaction:

$$2e^- + 2H^+ + 0.5\,O_2 \rightarrow H_2O \tag{2.2}$$

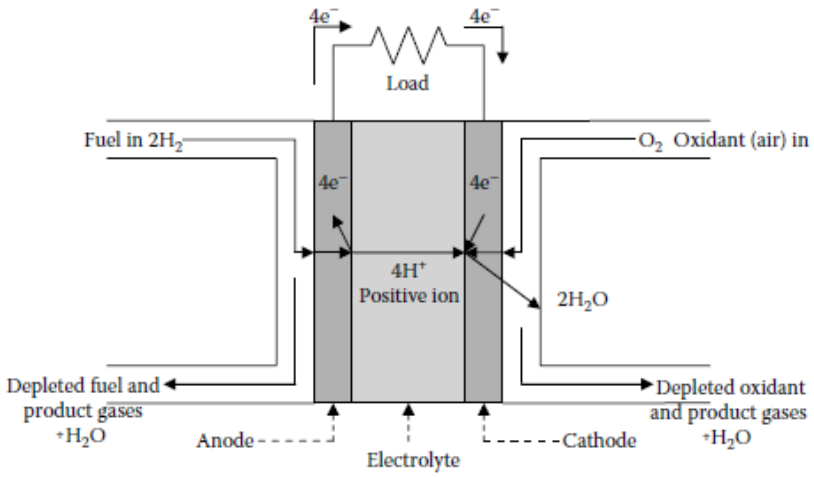

Figure 2.2 Electrochemical reactions in a PEMFC [3].

The overall reaction is shown as follows, which is the same as the reaction of hydrogen combustion.

$$H_2 + 0.5\ O_2 \rightarrow H_2O \tag{2.3}$$

Since hydrogen combustion is an exothermic process, the above equation can be modified as follows, where the heat is the difference between the heat of formation of the product (H_2O) and that of the reactants (H_2 and $0.5\ O_2$).

$$H_2 + 0.5\ O_2 \rightarrow H_2O + heat \tag{2.4}$$

The heat of formation of liquid water is -286 kJ/mol at 25 ^{o}C and the heat of formation of H_2 and O_2 are zeros. Therefore, the enthalpy change of the above reaction is -286 kJ per mole of H_2 at 25 ^{o}C. The negative sign means that energy is released in the reaction. The enthalpy change from the hydrogen combustion reaction is also called the hydrogen's heating value [4].

However, there is no combustion in a fuel cell. Only a portion of the hydrogen's heating value can be converted into electricity. This amount corresponds to Gibbs free energy with the following definition:

$$\Delta G = \Delta H - T\Delta S \tag{2.5}$$

where G is the Gibbs free energy, H is the enthalpy, T is the temperature in Kelvin, and S is the entropy. Δ refers to the changes from the reactants to the products.

The equivalence of the Gibbs free energy to the fuel cell potential (voltage) is linked through Faraday's constant (F).

$$W_{el} = -\Delta G \tag{2.6}$$

$$W_{el} = nFE \tag{2.7}$$

$$F = 96485\ coulombs/electron - mol \tag{2.8}$$

The theoretical potential (voltage) of a fuel cell is obtained as follows:

$$E = \frac{-\Delta G}{nF} \tag{2.9}$$

At 25 ^{o}C, the theoretical PEM fuel cell potential cell is 1.229 Volts.

$$E^{0} = \frac{-\Delta G^{0}}{nF} \tag{2.10}$$

At a temperature other than 25 ^{o}C and a pressure other than 1 atm, the Nernst equation [4] is used to compute the theoretical open circuit voltage.

$$E_r = -\frac{\Delta H - T\Delta S}{nF} - \frac{RT}{nF} ln(\frac{p_{H_2O}}{p_{H_2}\, p_{O_2}^{0.5}}) \tag{2.11}$$

where p_{H_2O}, p_{H_2} and $p_{O_2}$are partial pressures in the unit of atm.

However, in practice, the open circuit cell potential is significantly lower than the theoretical cell potential due to the losses in the fuel cell even when no external current is generated. The cell potential drops even further when the fuel cell is connected to an external circuit to provide electricity. The next section explains the fuel cell characteristics when it is in operation.

2.2.2 Performance Model of a Fuel Cell

Figure 2.3 shows the polarization curve (voltage-current curve) of a typical PEM fuel cell. The x-axis of the curve is the current density with the unit of A/cm^2. The y-axis is the cell potential (voltage) with the unit of Volt. From the curve, the operation voltage of a fuel cell can be determined as a function of the current density. The polarization curve is commonly used to evaluate the performance of a fuel cell. It provides a graphic indication of the losses associated with a fuel cell, namely open circuit losses, activation losses, ohmic losses, and mass transportation losses.

As shown in Figure 2.3, even when the current density is zero, which means no electrical load is connected to the fuel cell, the cell potential is less than the theoretical

voltage from Equation (2.11). This difference may be due to the fuel crossover from anode to the cathode, the existence of an impurity, or current leakage [38].

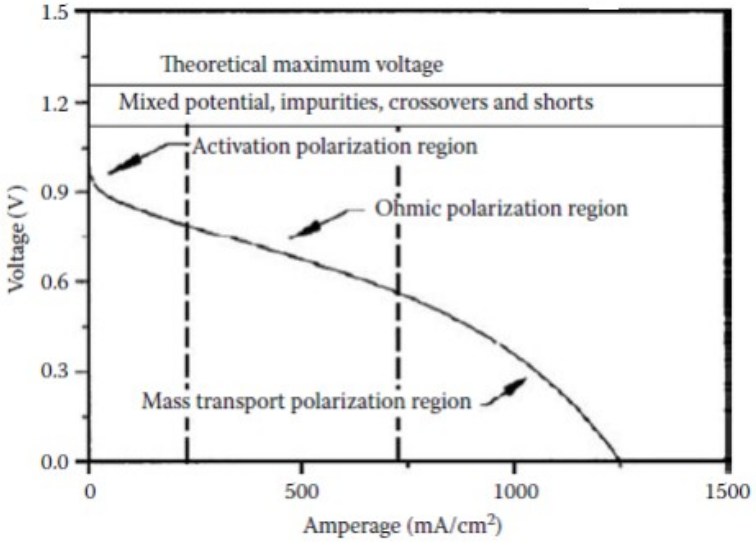

Figure 2.3 Polarization curve of a typical PEM fuel cell [4].

The activation polarization is the voltage differences that are needed to drive the electrochemical reactions (Equation (2.1) and (2.2)) in the direction of electron generation from the chemical reaction equilibrium. This behavior was observed by Tafel in 1905 through experiments [2]. The amount of the activation losses is given by the following equation, which is also known as the Tafel Equation.

$$\Delta V_{act} = A\, log(\frac{i}{i_0}) = a + b\, log\, i \tag{2.12}$$

where i is the current density and i_0 is the exchange current density.

The exchange current density i_0 is the current density at which the fuel cell starts to have useful cell potential that is greater than zero.

This behavior was later explained theoretically using the *Butler-Volmer Equation* [4]. The activation losses can be expressed as follows,

$$\Delta V_{act} = \frac{RT}{\alpha_c F} ln\left(\frac{i}{i_{0,c}}\right) + \frac{RT}{\alpha_a F} ln\left(\frac{i}{i_{0,c}}\right) \tag{2.13}$$

where α_c is the transfer coefficient at the cathode, and α_a is the transfer coefficient at the anode.

For a PEM fuel cell, the activation losses at the cathode are much more significant than the activation losses at the anode. The activation voltage losses can be further simplified as follows:

$$\Delta V_{act} = \frac{RT}{\alpha F} ln\left(\frac{i}{i_0}\right) \tag{2.14}$$

Equation (2.14) is modified to include the open circuit voltage losses due to fuel crossover and internal resistance [2].

$$\Delta V_{act} = \frac{RT}{\alpha F} ln\left(\frac{i - i_{loss}}{i_0}\right) \tag{2.15}$$

Ohmic losses, which are due to the resistance to the flow of ions in the electrolyte and the flow of the electrons through the conductive components of a fuel cell, can be expressed by the Ohm's law, which states that the voltage losses are proportional to the internal resistance of a fuel cell.

$$\Delta V_{ohm} = i\, R_i \tag{2.16}$$

where the R_i is the area specific resistance, with the unit $\text{Ohm} \cdot \text{cm}^2$.

Concentration losses are significant when the reactants are consumed rapidly to deliver high current density. When a fuel cell is operating at high current density, the reactions at the anode and cathode cause a pressure drop for the hydrogen and oxygen at the gas flow channel. The reduction in gas pressure leads to a reduction in voltage. However, an analytical solution to model this behavior is absent from the literature. Equation (2.17) is a commonly used empirical equation, which fits the experimental results very well [36].

$$\Delta V_{con} = m\, exp(ni) \tag{2.17}$$

With the above voltage losses, the cell potential of a fuel cell in operation can be obtained as follows:

$$E = E_r - \Delta V_{act} - \Delta V_{ohm} - \Delta V_{con} \tag{2.18}$$

$$E = E_r - \frac{RT}{\alpha F} ln\left(\frac{i - i_{loss}}{i_0}\right) - i\, R_{ohm} - m\, exp(ni) \tag{2.19}$$

Figure 2.4 shows a comparison of the experimental data and the numerical model using Equation (2.19). The experimental data was obtained from a PEM fuel cell system with 50 cm^2 active area with low platinum loading and a Nafion® 115 membrane [36]. The fuel cell model parameters, E_r, i_{loss}, i_0, R_{ohm}, m, and n are obtained through nonlinear programming optimization software that minimizes the differences between the model and the experimental data.

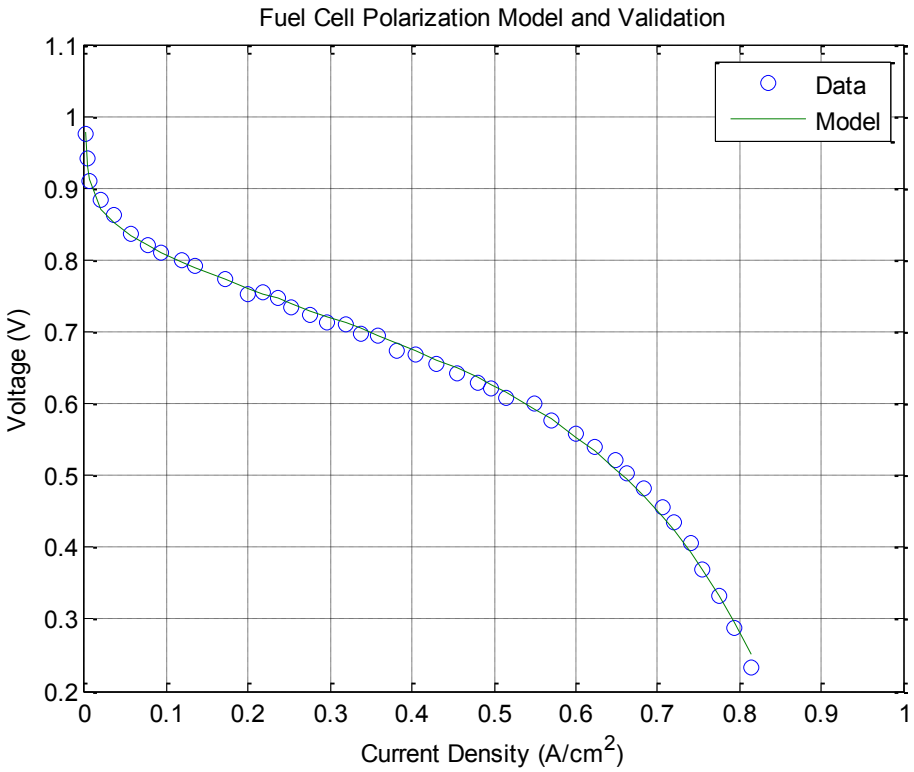

Figure 2.4 Model validation for the polarization curve of a fuel cell.

2.2.3 Dynamic Model of a Fuel Cell

The polarization curve of a fuel cell addresses only the steady state relationship between the current density and the cell potential. Dynamic modeling of a fuel cell is needed to understand the transient behavior when its current density is changed from one level to another level. An electric circuit model of a fuel cell is commonly used to model the dynamic behavior of a fuel cell [3].

As shown in Equation (2.11), the ideal voltage of a fuel cell depends on the partial pressure of the reactants, which is determined by the number of reactants inside the gas flow channel, which are influenced by the supply and consumption of the reactants. The reactant consumption is determined by the current at the electric circuit. The partial pressures of the reactants can be determined through the following ideal gas equations:

$$\frac{V_a}{RT}\frac{dp_{H_2}}{dt} = M_{H_2,net} - \frac{I}{2F} \tag{2.20}$$

$$\frac{V_c}{RT}\frac{dp_{O_2}}{dt} = M_{O_2,net} - \frac{I}{4F} \tag{2.21}$$

$$\tau_a \frac{dM_{H_2,net}}{dt} = \frac{I}{2F} - M_{H_2,net} \tag{2.22}$$

$$\tau_c \frac{dM_{O_2,net}}{dt} = \frac{I}{4F} - M_{O_2,net} \tag{2.23}$$

where p_{H_2} is the partial pressure of hydrogen, $p_{O_2}$is the partial pressure of O2, V_a is the volume of the anode flow channel, V_c is the volume of the cathode flow channel, R is the universal gas constant, T is the temperature, I is the current, F is the Faraday constant, $M_{H_2,net}$ is the net molar flow rate of hydrogen, and $M_{O_2,net}$ is the net molar flow rate of oxygen.

At a steady state condition, the net flow rate of hydrogen and oxygen is balanced with the current delivery in the electric circuit.

$$M_{H_2,net} = \frac{I}{2F} = 2\, M_{O_2,net} \tag{2.24}$$

Another important transient behavior of a fuel cell is the double-layer charging effect [37]. The membrane of a PEM fuel cell allows only the flow of protons, while the electrons have to travel through the external circuit. At the surface of the membrane, the electrons and protons form two charged layers of opposite polarity. The charged double-layer behaves like a super capacitor. The equivalent circuit of a fuel cell with this double-layer charging effect is shown in Figure 2.5, which is modeled with an equivalent capacitor.

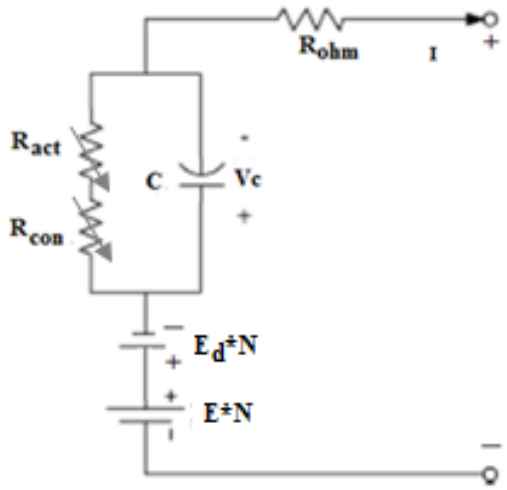

Figure 2.5 Equivalent electric circuit model of a fuel cell.

The corresponding mathematical equations can be obtained as follows:

$$V_c = \left(I - C\frac{dV_c}{dt}\right)(R_{act} + R_{con}) \tag{2.25}$$

$$V_{out} = E - V_c - I\, R_{ohm} \tag{2.26}$$

where the R_{act} and R_{con} are the equivalent resistances for activation losses and concentration losses.

Although Equations (2.20) to (2.23) consider the effect of reactant dynamics on the partial pressure, there is an additional transient voltage drop due to the fuel cell delay effect [37]. The fuel cell delay, which is the delay between the load current and the change in the flow of fuel and oxidant, is caused by the transport process of proton, hydrogen, oxygen, water vapor and liquid water within the fuel cell membranes [72]. The simplified model from [37] is used to model the fuel cell delay effect and is shown as follows:

$$\frac{dE_d}{dt} = -\frac{1}{\tau_e}E_d(t) + \lambda_e\frac{dI}{dt} \tag{2.27}$$

The dynamic equations of a fuel cell system, which is formed by connecting many fuel cells in series, are summarized as follows:

$$\frac{V_a}{RT}\frac{dp_{H_2}}{dt} = M_{H_2,net} - \frac{I}{2F} \tag{2.28}$$

$$\frac{V_c}{RT}\frac{dp_{O_2}}{dt} = M_{O_2,net} - \frac{I}{4F} \tag{2.29}$$

$$\frac{dM_{H_2,net}}{dt} = \frac{1}{\tau_a}\left(\frac{I}{2F} - M_{H_2,net}\right) \tag{2.30}$$

$$\frac{dM_{O_2,net}}{dt} = \frac{1}{\tau_c}\left(\frac{I}{4F} - M_{O_2,net}\right) \tag{2.31}$$

$$\frac{dV_c}{dt} = -\frac{1}{(R_{act} + R_{con})C}V_c + \frac{I}{C} \tag{2.32}$$

$$\frac{dE_d}{dt} = -\frac{1}{\tau_e}E_d(t) + \lambda_e\frac{dI}{dt} \tag{2.33}$$

where

$$E_r = E^0 - \frac{RT}{nF}ln\left(\frac{p_{H_2O}}{p_{H_2}\,p_{O_2}^{0.5}}\right) = E^0 + \frac{RT}{nF}ln\left(p_{H_2}\,p_{O_2}^{0.5}\right) \tag{2.34}$$

$$E = E_r - \frac{RT}{\alpha F}ln\left(\frac{i + i_{loss}}{i_0}\right) - i\,R_{ohm} - m\,exp(ni) \tag{2.35}$$

$$V_{out} = (E - E_d)N - V_c - I\,R_{ohm} \tag{2.36}$$

$$i = \frac{I}{A_a} \tag{2.37}$$

$$C = C_i\left(\frac{A_a}{N}\right) \tag{2.38}$$

$$R_{ohm} = \frac{R_i N}{A_a} \tag{2.39}$$

$$R_{act} = \frac{RT}{\alpha F} ln\left(\frac{i + i_{loss}}{i_0}\right)\left(\frac{N}{i\ A_a}\right) \tag{2.40}$$

$$R_{con} = m\ exp(n\ i)\left(\frac{N}{i\ A_a}\right) \tag{2.41}$$

2.2.4 Model Reduction

From Equations (2.29) to (2.33), it can be observed that the states, p_{H_2}, p_{O_2}, $M_{H_2,net}$ and $M_{O_2,net}$ are isolated from other dynamic states. These states are influenced only by the current. Figure 2.6 shows the dynamic responses of the partial pressures and the corresponding theoretical open circuit voltage (E_r). It can be observed that the magnitude of the change in the partial pressure (p_{H_2}) from one operating point to another operating point is very small. The calculation of the corresponding theoretical open circuit voltage is given by Equation (2.34). The term $\frac{RT}{nF}$, which is very small, leads to very little influence observed in the theoretical open circuit voltage. Due to the insignificant influence of these four dynamic states on the fuel cell theoretical open circuit voltage, these states are reduced to steady states.

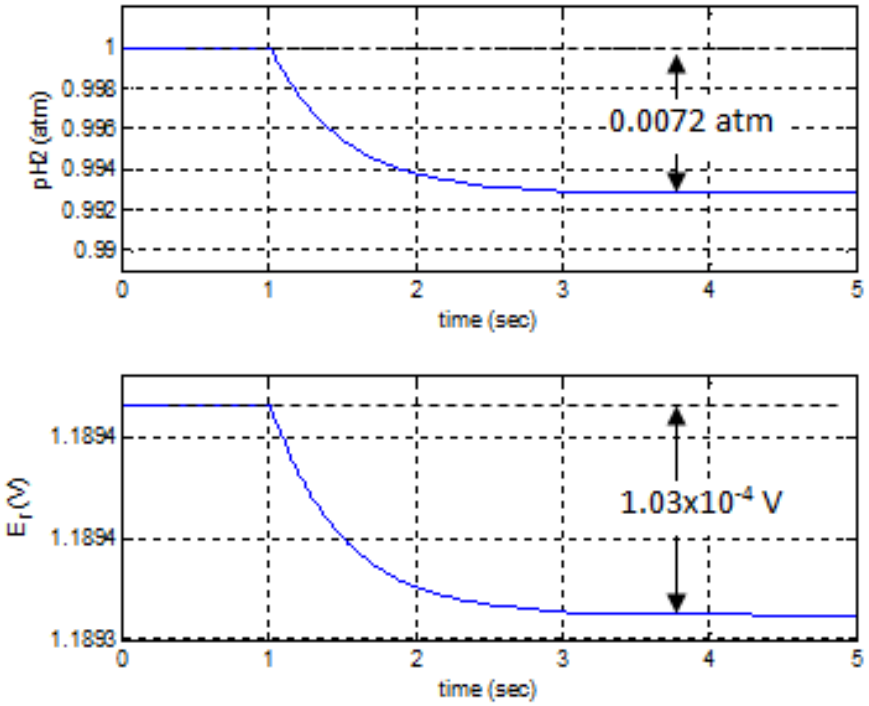

Figure 2.6 Transient responses of the partial pressures in a fuel cell.

With the gas states reduced to steady states, there are two dynamic effects to be included in a fuel cell dynamic model, the double-layer charging effect (Equation (2.32)) and the fuel cell delay effect (Equation (2.33)). Figure 2.7 shows the transient response of a fuel cell system, whose performance curve is shown in Figure 2.8, when the current is changed from one level to another level. It can be observed in Figure 2.7 that the fuel cell output voltage (V_{out}) drops to the lowest level immediately after the current step and then slowly reaches another steady state value. When there is a sudden change in the current, a voltage drop is expected due to the fuel cell delay effect. This voltage drop slowly recovers back to zero. The associate operating points in the fuel cell performance curve are shown in Figure 2.8. The delay in the fuel cell output voltage directly translates to a delay in the power available from the fuel cell system, which is expected to lead to additional delay in the propeller rotational speed.

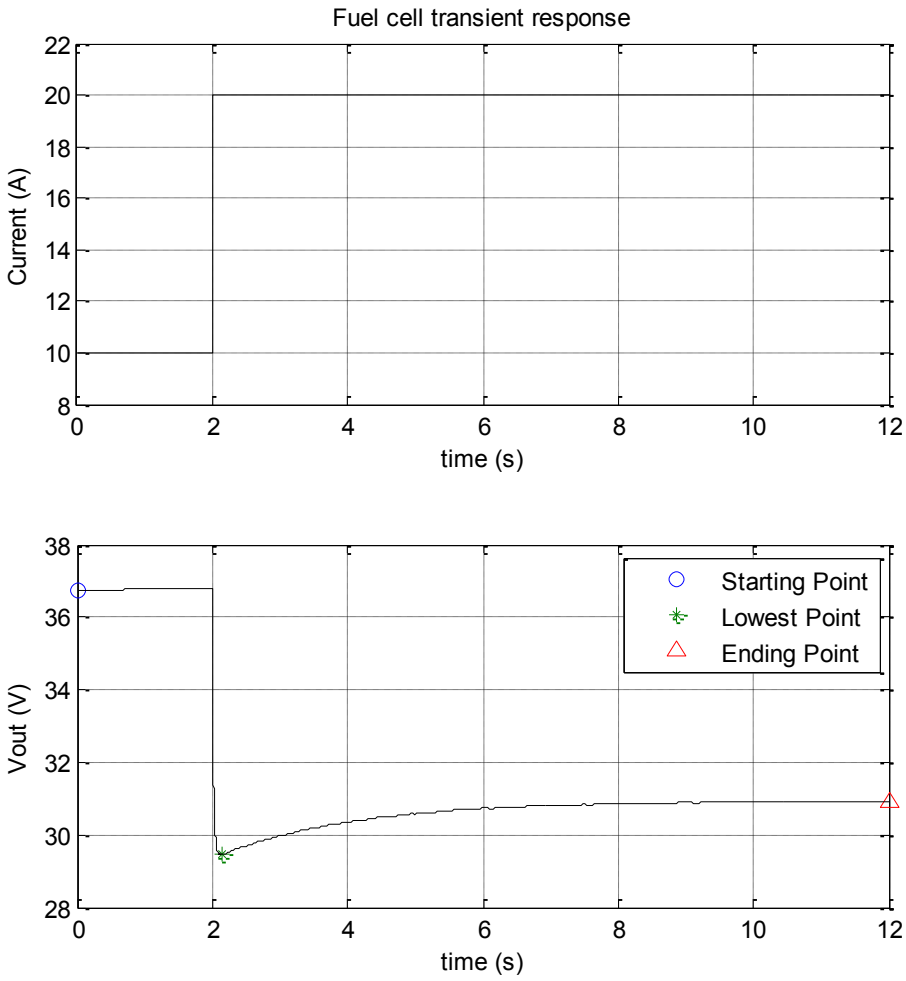

Figure 2.7 Fuel cell transient response for a step change in the current.

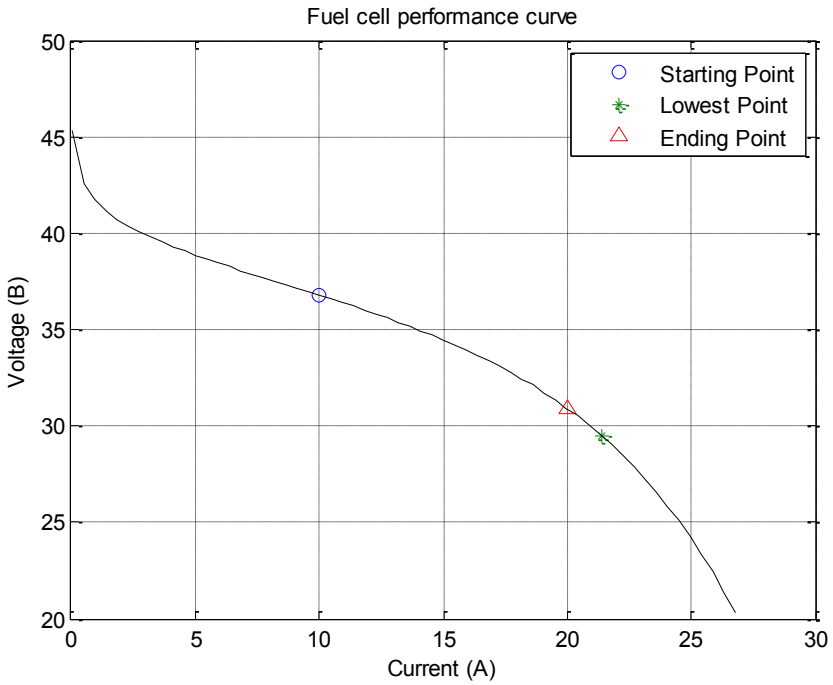

Figure 2.8 Fuel cell operating points for a step change in the current.

2.3 Dynamic Model of an Electric Motor

Brushless Direct Current (BLDC) motors, which are electronically commutated instead of using brushes for commutation, are widely used in the appliance, automotive, aerospace, and automation industries [73]. Their advantages are high dynamic response, high efficiency, long operation life, and noiseless operation, etc [73]. These advantages make BLDC motors excellent for UAV applications.

Figure 2.9 shows the equivalent electric circuit of a BLDC motor. When a DC voltage is applied to a BLDC motor, there is current in the windings due to Ohm's law. The electric current in the windings, together with the magnetic field around the windings, generates mechanical forces (torque) due to the electromotive effect. When the motor rotates, a back EMF (BEMF) voltage is generated due to the electromotive effect of a

rotational current in a magnetic field. The rotational speed of the BLDC motor reaches a constant level when the torque of the motor is equal to the torque of the load.

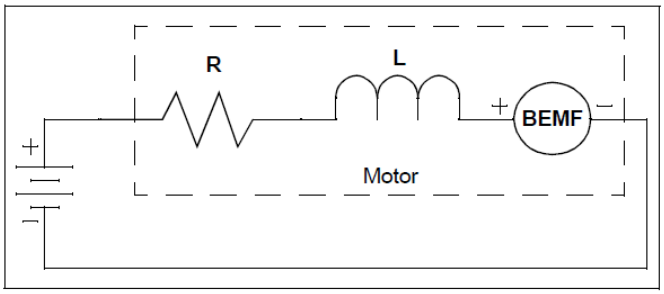

Figure 2.9 BLDC motor equivalent circuit [74].

Figure 2.10 illustrates the working principle of a BLDC motor with a propeller. The control signal of the speed controller determines the voltage (V_{in}) applied to the motor circuit. An increase in V_{in} leads to an increase in the current (Equation (2.42)). The increase in the current leads to an increase in the motor torque (Equation (2.43)). The rotational speed of the propeller increases due to the difference in the driving torque and the loading torque (Equation (2.44)). The increase in the motor rotational speed results an increase in the BEMF (V_m) due to the electromotive effect (Equation (2.45)). The increase in the BEMF (V_m) limits the increase of the current. The whole system reaches a steady state when the driving torque of the motor (Q_m) is the same as the aerodynamic torque of the propeller (Q_p).

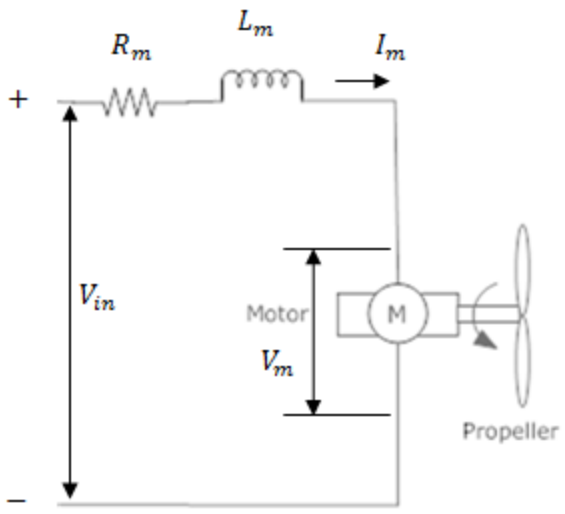

Figure 2.10 Diagram of a BLDC motor connected with a propeller.

The mathematical relations of the above process are summarized in Equations (2.42) to (2.45).

$$V_{in} = I_{mr}\, R_{mr} + L_m \frac{dI_m}{dt} + V_m \tag{2.42}$$

$$Q_m = \frac{I_m - i_{0,m}}{K_v} \tag{2.43}$$

$$\frac{d\Omega}{dt} = \frac{Q_m - Q_p}{J} \tag{2.44}$$

$$V_m = \frac{\Omega}{K_v} \tag{2.45}$$

where R_m, L_m, $i_{0,m}$, K_v are motor specific parameters.

2.4 Performance Model of a Fixed-Pitch Propeller

A propeller produces thrust force by rotating its lifting surfaces about a shaft [75]. The rotation of the lifting surfaces, the propeller blades, leads to several relative motions of the air. As shown in Figure 2.11, V is the axial velocity due to free stream air velocity, Ωr_0 is the rotational velocity of the propeller, and U_{θ_0} and U_{z_0} are the induced velocities caused by the propeller disturbances.

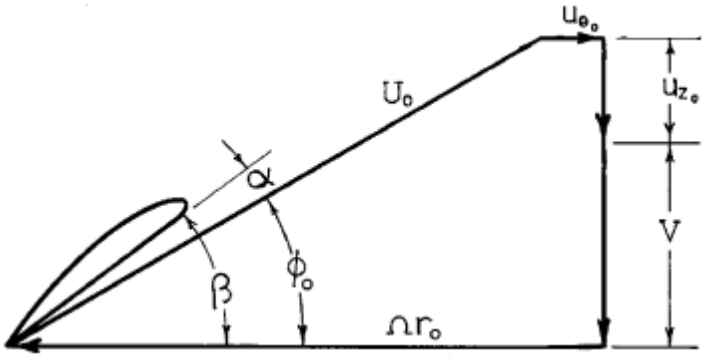

Figure 2.11 Velocity of a blade element [75].

The fundamental relations for a propeller are derived from the Kutta-Joukowsky theorem and the two-dimensional airfoil theory [75]. The equations from [75] are summarized as follows:

$$dL = \rho U_0 \times \Gamma \, dr \tag{2.46}$$

where dL is the lift force on a blade element, ρ is the air density, U_0 is the resultant total velocity, Γ is the bound circulation, and dr is the blade element radial dimension.

$$dT = \rho\Gamma\left(\Omega r - u_{\theta_0}\right)dr \tag{2.47}$$

$$dQ = \rho\Gamma\left(V + u_{z_0}\right)r \, dr \tag{2.48}$$

where dT is the sectional thrust, dQ is the sectional torque, and u_{θ_0} and u_{z_0} are the induced velocities.

From the two-dimensional airfoil theory, the sectional lift force is determined by the local angle of attack of the blade element.

$$dL = \frac{\rho}{2} U_0^2 c_l c \, dr = \frac{\rho}{2} a_0 (\alpha - a_0) U_0^2 c \, dr \tag{2.49}$$

where a_0 is the lift curve slope, α is the local angle of attack, a_0 is the zero-lift angle of attack, and c is the blade chord.

The local angle of attack is computed as $\alpha = \beta - \phi$, where β is the geometric blade angle and ϕ is the angle of the resultant velocity to the plane of the propeller.

$$\phi = atan\left(\frac{V + u_{z_0}}{\Omega r - u_{\theta_0}}\right) \tag{2.50}$$

The link between the bound circulation and airfoil lift can be obtained from Equation (2.49) and (2.51).

$$\Gamma = \frac{1}{2} a_0(\alpha - a_0) U_0 c \tag{2.51}$$

The above equations define the fundamental relations of a propeller, but the relations among the bound circulation, the blade geometry, and the induced velocities are difficult to determine. The investigation of the propeller theories for these relations can be dated back to the early 1900s [76,77,78].

The non-dimensional propeller performance parameters, the thrust coefficient (C_t), the power coefficient (C_p), and the efficiency of a propeller, are defined as follows:

$$C_t = \frac{Thrust}{\rho \Omega^2 R^4} \tag{2.52}$$

$$C_p = \frac{Power}{\rho \Omega^3 R^5} \tag{2.53}$$

$$\eta = \frac{Thrust \cdot V}{Power} \tag{2.54}$$

Studying the dynamic behavior of a fuel cell powered propeller requires that the propeller's performance data be obtained either from a comprehensive propeller inflow model or from the experimental measurement data. The thrust coefficient and torque coefficient can be determined based on the rotational speed and the free stream air velocity. The resulting thrust force and required power are computed using Equations (2.52) and (2.53).

2.5 Dynamic Model of a Fuel Cell Powered UAV Propulsion System

The dynamic model of a fuel cell powered UAV propulsion system is obtained by combining the dynamic model of a fuel cell system, the dynamic model of an electric motor, and the performance model of a fixed pitch propeller. The electric circuit illustration of a fuel cell powered UAV propulsion system is shown in Figure 2.12. The left portion of the diagram represents a fuel cell system, where both the steady state performance and the transient performance are modeled. The right portion of the diagram represents an electric motor and a propeller. The electric motor is modeled with an inductor and a resistor, and the thrust and power of the propeller is calculated from its aerodynamic performance data. The center portion represents an electric motor controller, which controls the amount of voltage from the fuel cell system to be applied to the electric motor according to the input signal.

The dynamic equations of a fuel cell powered UAV propulsion system are derived with the following assumptions:

- Both the performance model and dynamic model of the fuel cell system are based on one-dimensional treatment.
- The gases inside the fuel cell systems are assumed to be uniformly distributed.
- The temperature of the fuel cell system is assumed to be constant as it is regulated by the fuel cell system controller.
- The partial pressures of the hydrogen and oxygen are assumed to be constant as their influence on the open circuit voltage is insignificant.
- The electric motor is modeled with a lumped resistor and inductor.

- Both the back-EMF and the driving torque of the electric motor are linear functions of the motor constant (K_v).
- The delay between the propeller rotational speed and the thrust generated is assumed to be negligible.
- The propeller performance model is simplified with one-dimensional treatment, and the thrust coefficient and power coefficient are functions of the inflow ratio only.

The equations for a fuel cell powered UAV propulsion system model are shown in Equations (2.55) through (2.58), in which V_c is the voltage of the equivalent capacitor, E_d is the voltage drop associated with the fuel cell delay effect, I_m is the electric motor current and Ω is the propeller rotational speed. The transient behavior of a fuel cell system is modeled in Equations (2.55) and (2.56). The electric motor current as function of input voltage, motor resistance, and BEMF are modeled in Equation (2.57). The propeller rotational speed is governed by the torque difference between the electric motor and the propeller aerodynamic loading, as shown in Equation (2.58).

Equations (2.59) to (2.69) are derived based on physical relations. Equation (2.59) determines the fuel cell voltage as a function of load current density. The current density (i) is defined as current per unit area as shown in Equation (2.61). Equation (2.59) also models the steady state performance of a fuel cell system. The parameters, i_{loss}, i_0, R_i, m, and n, in Equation (2.59) are obtained by validating the fuel cell performance curve against the manufacturer's performance data. The output voltage of the fuel cell system (V_{out}) is computed using Ohm's Law, as shown in Equation (2.60). The three types of losses associated with a fuel cell system in operation, the activation losses (R_{act}), the

ohmic losses (R_{ohm}) and the concentration losses (R_{con}), are calculated using Equations (2.63) to (2.65). Equation (2.66) is the amount of voltage from the fuel cell system that is applied to the electric motor as a linear function of the input signal (u). Equation (2.67) is the back EMF voltage from the electric motor. Equation (2.68) is the torque available from the electric motor, which is proportional to the current of the electric motor. Equation (2.69) is the aerodynamic torque from the propeller, whose torque coefficient (C_q) is obtained from the propeller performance model.

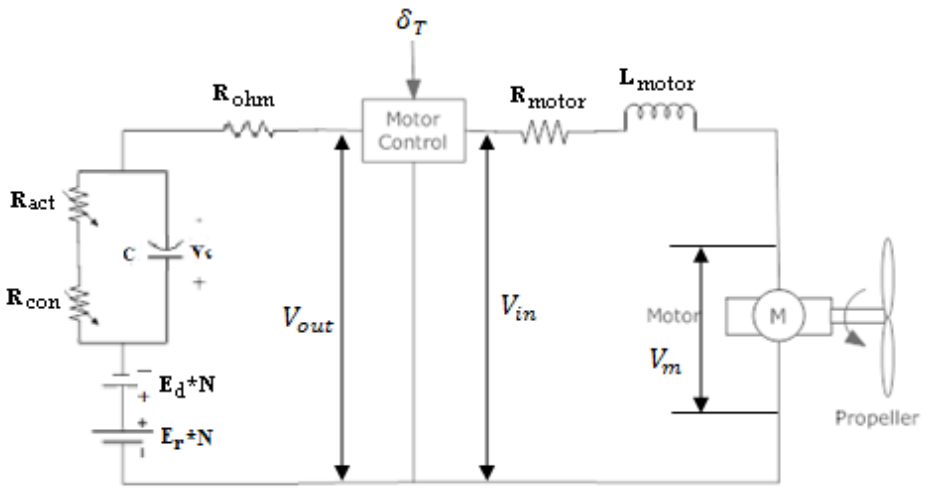

Figure 2.12 Electric circuit illustration of the fuel cell powered UAV propulsion system.

$$\frac{dV_c}{dt} = -\frac{1}{(R_{act} + R_{con})C} V_c + \frac{I}{C} \tag{2.55}$$

$$\frac{dE_d}{dt} = -\frac{1}{\tau_e} E_d(t) + \lambda_e \frac{dI}{dt} \tag{2.56}$$

$$\frac{dI_m}{dt} = \frac{1}{L_m}(V_{in} - I_m R_m - V_m) \tag{2.57}$$

$$\frac{d\Omega}{dt} = \frac{Q_m - Q_p}{J} \tag{2.58}$$

where,

$$E = E_r - \frac{RT}{\alpha F} ln\left(\frac{i + i_{loss}}{i_0}\right) - i\, R_i - m\, exp(ni) \tag{2.59}$$

$$V_{out} = (E_r - E_d)N - V_c - I\,R_{ohm} \tag{2.60}$$

$$i = \frac{I}{A_a} \tag{2.61}$$

$$C = C_i\left(\frac{A_a}{N}\right) \tag{2.62}$$

$$R_{ohm} = \frac{R_i N}{A_a} \tag{2.63}$$

$$R_{act} = \frac{RT}{\alpha F} ln\left(\frac{i + i_{loss}}{i_0}\right)\left(\frac{N}{i\,A_a}\right) \tag{2.64}$$

$$R_{con} = m\,exp(n\,i)\left(\frac{N}{i\,A_a}\right) \tag{2.65}$$

$$V_{in} = \delta_T * V_{out} \tag{2.66}$$

$$V_m = \frac{\Omega}{K_v} \tag{2.67}$$

$$Q_m = \frac{I_m - i_{0,m}}{K_v} \tag{2.68}$$

$$Q_p = \frac{1}{2}\rho(\Omega R)^2 \pi R^3 C_q \tag{2.69}$$

2.6 Transient Characteristics of a Fuel Cell Powered UAV Propulsion System

In this section, the dynamic model for a fuel cell powered UAV propulsion system is used to study the influence of the model parameters on the transient response characteristics of a fuel cell powered UAV propulsion system in the form of effective time constants and step command responses. The effective time constants are obtained by computing the eigenvalues of the linearized model at a specific operating point. The step responses are obtained by computing the time history of the state variables when the input signal is stepped from one value to another value.

The fuel cell powered UAV propulsion system sized for the Aerosonde UAV is used as the nominal model. The nominal values of the model parameters, L_m, C, τ_e, λ_e, and J, are shown in Table 2.1.

Table 2.1 Nominal values of the model parameters.

Model Parameters	Nominal Values
Electric motor inductance (L_m)	$200\ \mu h$
Fuel cell capacitance (C)	$200\ \mu F$
Fuel cell delay time constant (τ_e)	$2.0\ sec$
Fuel cell delay gain constant (λ_e)	$0.0033\ V/A$
Propeller Inertial (J)	$0.002\ kg \cdot m^2$

2.6.1 Trim and Linearization

The nonlinear model of a fuel cell powered UAV propulsion system is implemented in MATLAB as shown in Figure 2.13, where the MATLAB function block is the nonlinear equations shown in Equations (2.55) to (2.69). The model is trimmed at different input signal (δ_T) values (from 0.4 to 0.9), and at an air speed of 20 m/s. The steady state propeller rotational speed at different input values is shown in Figure 2.14.

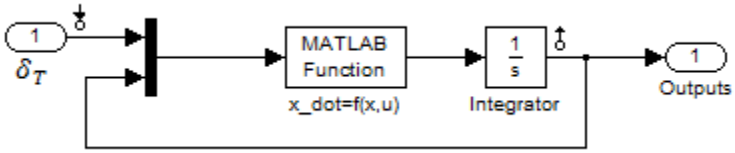

Figure 2.13 MATLAB implementation of the nonlinear model of a fuel cell powered UAV propulsion system.

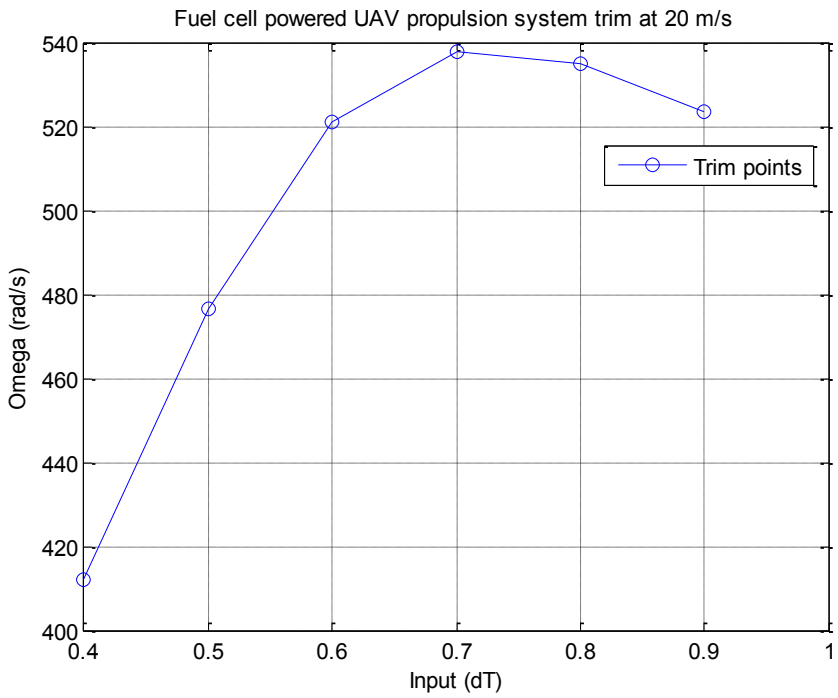

Figure 2.14 Propeller rotational speed at different input values at 20 m/s.

As shown in Figure 2.14, the propeller rotational speed increases with the input value when the input value is less than 0.7. The propeller rotational speed decreases with the input value when the input value is more than 0.7. This can be explained by the fuel cell performance curves shown in Figure 2.15 and Figure 2.16. When the input value increases, more power is required from the fuel cell system, but there is a limit on the maximum power that can be delivered by the fuel cell system. When the operating current of the fuel cell is more than the value that corresponds to the maximum power (marked as * in Figure 2.16), the power available from the fuel cell system drops as the current increases. The drop in the power from the fuel cell system leads to a decrease in the propeller rotational speed.

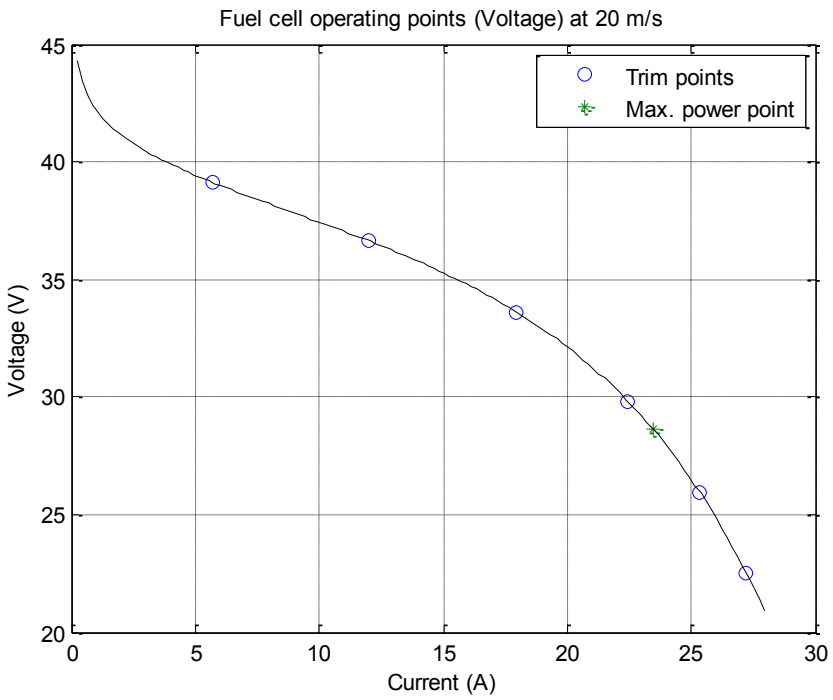

Figure 2.15 Fuel cell operating points on the voltage performance curve.

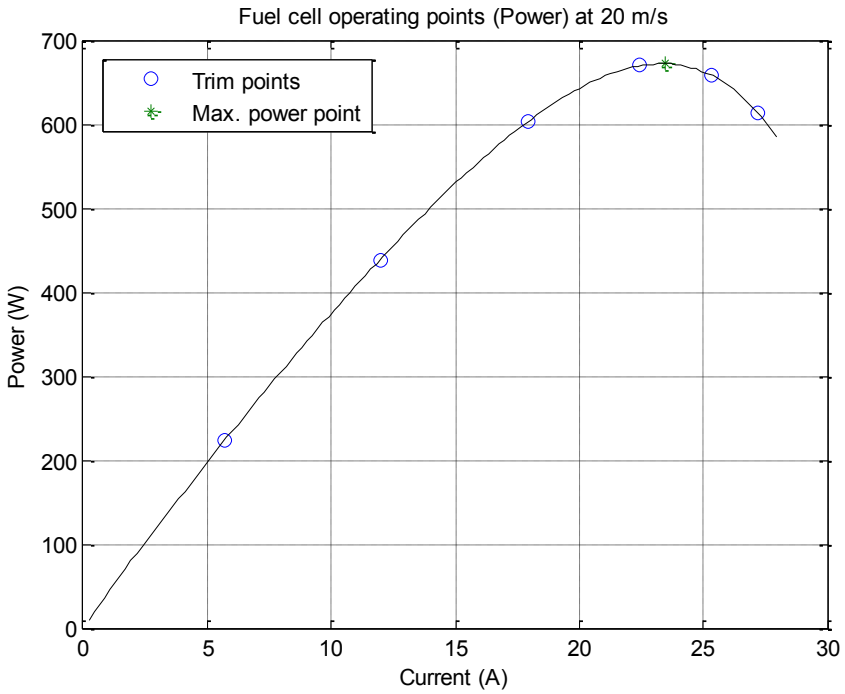

Figure 2.16 Fuel cell operating points on the power performance curve.

When a fuel cell powered UAV propulsion system is integrated with a UAV, the input signal is similar to that of the throttle signal in a conventional gas powered UAV, in which an increase in the throttle signal is expected to lead to an increase in the propeller rotational speed. Hence, the range of the input signal is set between 0.4 and 0.7.

The linearized model of a fuel cell powered UAV propulsion system is obtained by linearizing the nonlinear model shown in Figure 2.13 at different operation points. The time constants (τ_i) of the linearized model are computed by using the eigenvalues (λ_i) as shown in Equation (2.70). The time constants of the nominal system are shown in Table 2.2 at different input values. Among the four time constants, the third time constant, τ_3, is the largest.

$$\tau_i = -\frac{1}{\lambda_i} \tag{2.70}$$

Table 2.2 Time constants of the nominal system.

Input (u)	Time Constants (sec)			
	τ_1	τ_2	τ_3	τ_4
0.4	0.0018	0.0956	2.3421	0.2888
0.5	0.0014	0.0758	2.3455	0.2244
0.6	0.0012	0.0451	2.3053	0.2675
0.7	0.0010	0.0271	2.2336	0.3234

2.6.2 Parametric Study on Time Constants

In the parametric study on the time constants of the fuel cell powered UAV propulsion system, the value of each model parameter, L_m, C, τ_e, λ_e and J , varies between 20% and 500% of the nominal value listed in Table 2.1. The time constants at input value of 0.5 are used in this study.

Table 2.3 Time constants for different motor inductance.

$\frac{L_m}{L_{m,ref}}$	Time Constants (sec)			
	τ_1	τ_2	τ_3	τ_4
0.2	0.0003	0.0766	2.3455	0.2244
0.5	0.0007	0.0763	2.3455	0.2244
1.0	0.0014	0.0758	2.3455	0.2244
2.0	0.0036	0.0745	2.3456	0.2241
5.0	0.0075	0.0722	2.3458	0.2237

Table 2.3 shows the time constants of the linearized model of the fuel cell powered UAV propulsion system for different values of the motor inductance (L_m). The first time constant, τ_1, is significantly influenced by the motor inductance. This suggests that τ_1 is associated with the electric motor current. Since the magnitude of τ_1 is much smaller than that of other time constants, the influence of the motor inductance is insignificant.

Table 2.4 Time constants for different fuel cell capacitance.

$\frac{C}{C_{ref}}$	Time Constants (sec)			
	τ_1	τ_2	τ_3	τ_4
0.2	0.0015	0.0181	2.3485	0.1834
0.5	0.0014	0.0433	2.3474	0.1952
1.0	0.0014	0.0758	2.3455	0.2244
2.0	0.0014	0.1155	2.3390	0.3705
5.0	0.0014	0.1316	2.3583	0.7248

Table 2.4 shows the time constants of the linearized model of the fuel cell powered UAV propulsion system for different values of the fuel cell capacitance (C). Both the second and the fourth time constants are influenced by the fuel cell capacitance. The influence of the fuel cell capacitance is similar to that of an RC circuit, where higher capacitance leads to longer time constants.

Table 2.5 Time constants for different propeller inertial.

$\frac{J}{J_{ref}}$	Time Constants (sec)			
	τ_1	τ_2	τ_3	τ_4
0.2	0.0015	0.0243	2.3823	0.1336
0.5	0.0014	0.0530	2.3690	0.1577
1.0	0.0014	0.0758	2.3455	0.2244
2.0	0.0014	0.0900	2.2607	0.4927
5.0	0.0014	0.0938	2.0191	1.0599

Table 2.5 shows the time constants of the linearized model for different values of the propeller inertia. Similar to the fuel cell capacitance, both the second and fourth time constants are influenced by the propeller inertia. The influence of the propeller inertia to the propeller rotational speed is due to the aerodynamic drag of the propeller, where higher propeller inertia leads to larger time constants.

Table 2.6 Time constants for different fuel cell delay time constants.

$\frac{\tau_e}{\tau_{e,ref}}$	Time Constants (sec)			
	τ_1	τ_2	τ_3	τ_4
0.2	0.0014	0.0809	0.4038	0.2447
0.5	0.0014	0.0769	1.1443	0.2268
1.0	0.0014	0.0758	2.3455	0.2244
2.0	0.0014	0.0752	5.9403	0.2232
5.0	0.0014	0.0750	11.9291	0.2229

Table 2.6 shows the time constants of the linearized model for different values of the fuel cell delay time constant (τ_e). It can be seen that the third time constant, τ_3, is significantly influenced by the fuel cell delay time constant. This suggests that τ_3 is associated with fuel cell delay voltage (E_d). The magnitude of $\tau_3$is slightly larger than that of τ_e. Since $\tau_3$is the largest among the four time constants, the transient response of

the propeller rotational speed is expected to be highly influenced by the fuel cell delay time constant.

Table 2.7 Time constants for different fuel cell delay gain constants.

$\frac{\lambda_e}{\lambda_{e,ref}}$	Time Constants (sec)			
	τ_1	τ_2	τ_3	τ_4
0.2	0.0027	0.0491	2.0677	0.2114
0.5	0.0020	0.0606	2.1707	0.2162
1.0	0.0014	0.0758	2.3455	0.2244
2.0	0.0009	0.0962	2.7047	0.2406
5.0	0.0004	0.1216	3.8262	0.2802

Table 2.7 shows the time constants of the linearized model for different values of the fuel cell delay gain constant (λ_e). As indicated in Equation (2.56), λ_e determines the amount of voltage drop corresponding to the rate of change in the current during the transient. This parameter influences all four time constants.

In summary, the correspondence between the time constants of the linearized model and the four dynamic states is identified. Among the four time constants, the delay due to electric motor current is insignificant, and the delay due to fuel cell delay effect is most significant.

2.6.3 Parametric Study on Step Responses

When the input signal is in the range of 0.4 to 0.7, an increase in the input signal leads to an increase in the propeller rotational speed. Due to the delay in the fuel cell system, a delay in the transient response of the propeller rotational speed is expected. The variations of the model parameters in the parametric study on step responses are the same as those presented in the previous section. In this study, the input signal is stepped from 0.4 to 0.6, and the corresponding propeller rotational speed is increased from 412 rad/s to

521 rad/s. The step response of the propeller rotational speed with ideal voltage supply is also presented for reference.

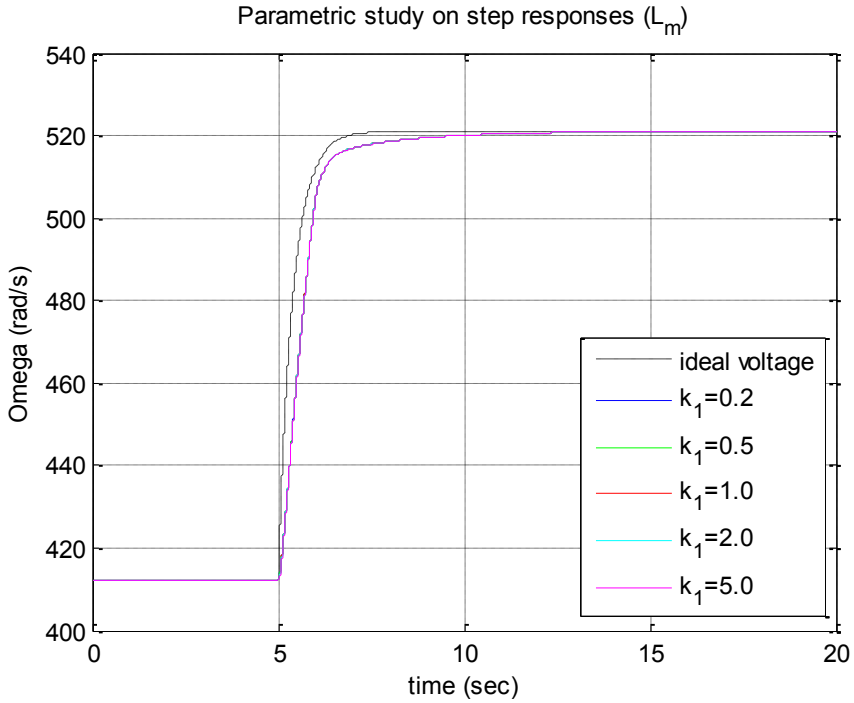

Figure 2.17 Step response variations due to electric motor inductance.

Figure 2.17 shows the propeller rotational speed step responses for different values of the motor inductance, where $k_1 = \frac{L_m}{L_{m,ref}}$. There are no observable differences in the step responses. This agrees with the study on time constants that the influence of motor inductance is expected to be insignificant.

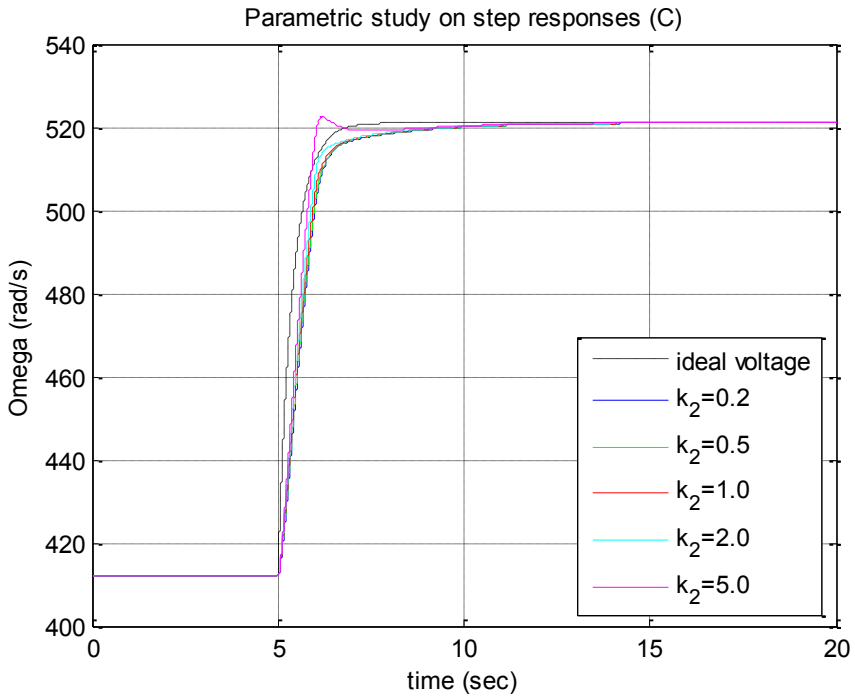

Figure 2.18 Step response variations due to fuel cell capacitance.

Figure 2.18 shows the propeller rotational speed step responses for different values of fuel cell capacitance, where $k_2 = \frac{C}{C_{ref}}$. A capacitor is an energy storage device that stores or releases energy when there is a change in the current. When the input signal is increased from 0.4 to 0.6, energy stored in the fuel cell due to the double-layer charging effect is released. Higher fuel cell capacitance corresponds to more energy storage, which leads to a faster response in the propeller rotational speed.

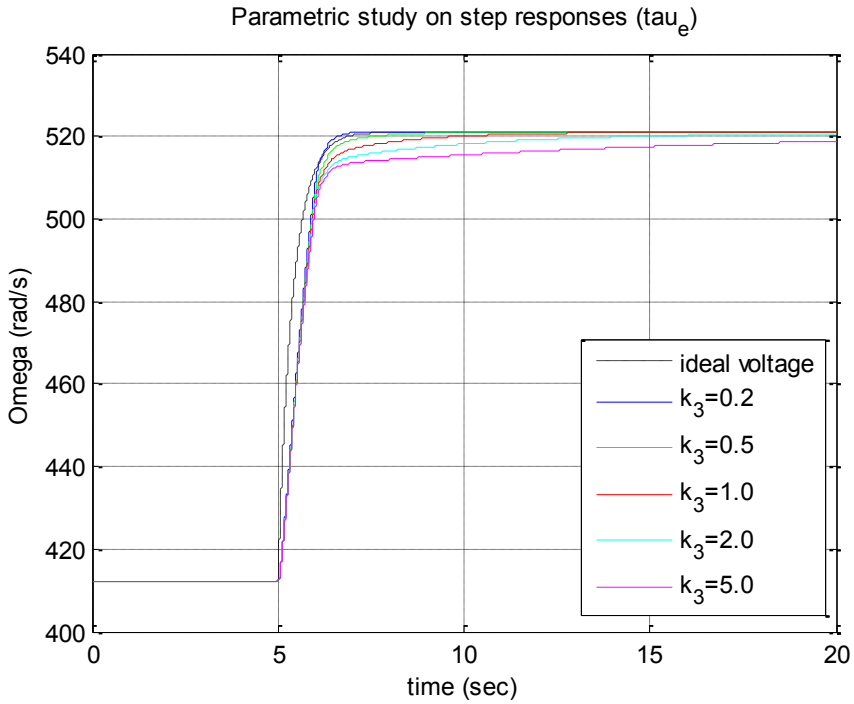

Figure 2.19 Step response variations due to the fuel cell delay time constant.

Figure 2.19 shows the propeller rotational speed step responses for different values of the fuel cell delay time constant, where $k_3 = \frac{\tau_e}{\tau_{e,ref}}$. The fuel cell delay time constant determines the time delay in the voltage drop associated with the rate of change in the current. Additional delay due to the fuel cell delay time constant is observed in the propeller rotational speed. However, the impact of the fuel cell delay time constant appears only after the initial delay due to the propeller aerodynamic drag.

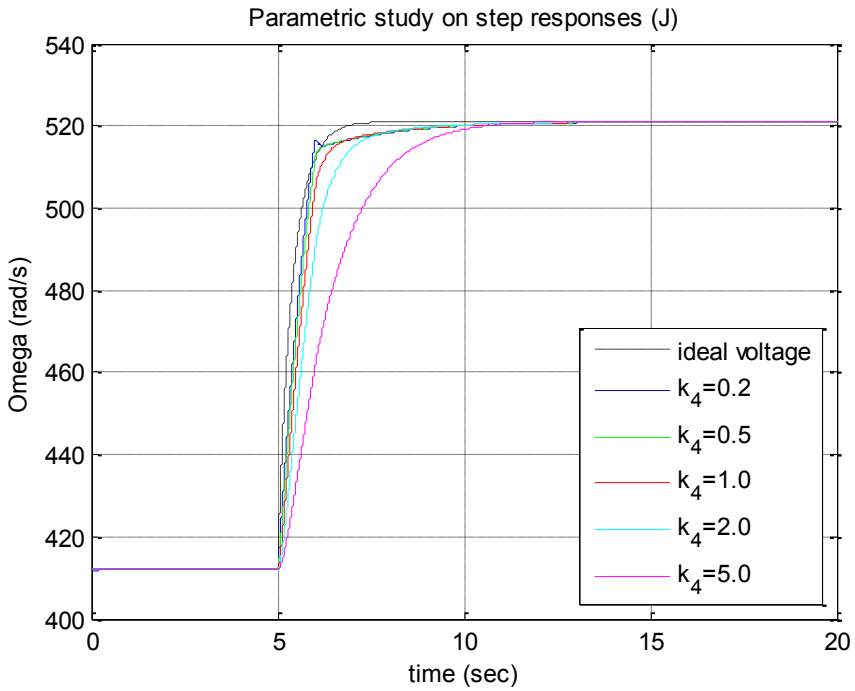

Figure 2.20 Step responses variations due to propeller inertia.

Figure 2.20 shows the propeller rotational speed step responses for different values of the propeller inertia, where $k_4 = \frac{J}{J_{ref}}$. Due to aerodynamic drag, higher propeller inertia leads to a longer time delay in the propeller rotational speed. If time constant τ_4 is smaller than time constant τ_3, the step response of the propeller rotational speed is mainly caused by the fuel cell delay effect. If time constant τ_4 is larger than time constant τ_3, the step response of the propeller rotational speed is mainly due to the aerodynamic drag.

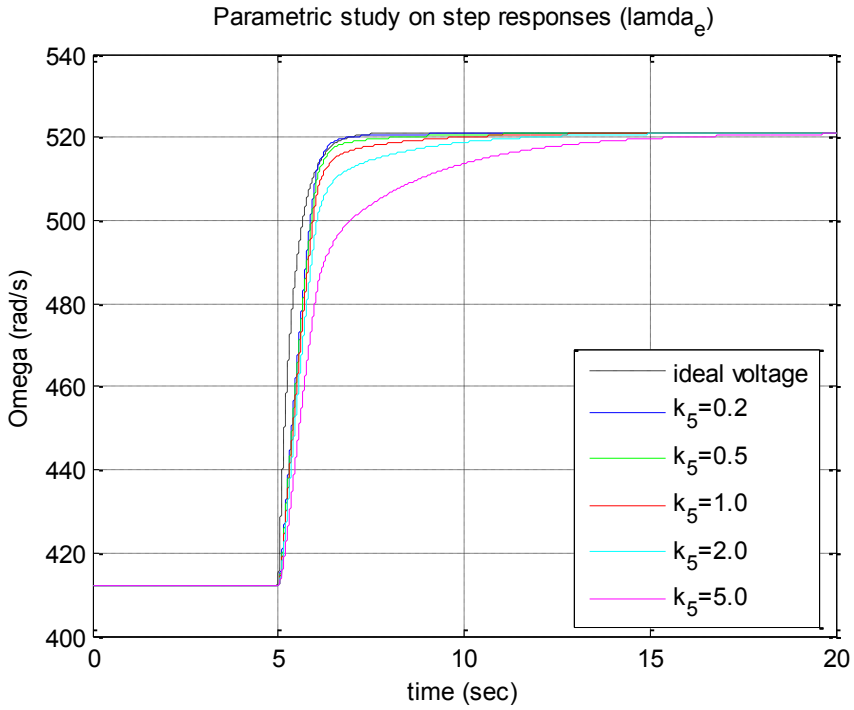

Figure 2.21 Step response variations due to fuel cell delay gain constant.

Figure 2.21 shows the propeller rotational speed step responses for different values of the fuel cell delay gain constant, where $k_5 = \frac{\lambda_e}{\lambda_{e,ref}}$. The fuel cell delay gain constant is proportional to the magnitude of the voltage drop due to the rate of change in the current, which influences the magnitude of the propeller rotational speed delay due to the fuel cell delay effect. When the fuel cell delay gain constant is sufficiently large, the delay in the propeller rotational speed due to the aerodynamic drag becomes insignificant.

In summary, the five model parameters influence the transient response of the propeller rotational speed in different ways. Changes in these parameters may reduce the delays in the propeller rotational speed, which may improve the transient performance of a fuel cell powered UAV.

2.7 Summary

In this chapter, a dynamic model of a fuel cell powered UAV propulsion system was derived by combining the dynamic model of a fuel cell system, the dynamic model of an electric motor, and the performance model of a propeller. In the dynamic model of a fuel cell system, the steady state performance is modeled with a semi-empirical polarization curve, and the transient performance is modeled with a double-layer charging effect and the fuel cell delay effect. The partial pressures of the hydrogen and the air were reduced to steady states, as their variations were insignificant. The influence of the fuel cell system parameters on the transient characteristics of a fuel cell powered UAV propulsion system was investigated through the effective time constants and step command responses, and the influence of the fuel cell delay constants was the most significant.

CHAPTER 3

A FUEL CELL POWERED UAV CONFIGURATION

3.1 Introduction

The Aerosonde UAV (Figure 3.1), developed by Aerosonde Pty Ltd, Australia, is one of the few commercial UAVs in its weight class that offers an endurance of more than 24 hours [79]. It was also the first unmanned aircraft that crossed the Atlantic Ocean with a flight distance of 3,270 kilometers [79]. Its small scale, light weight, and high efficiency engine contribute to its excellent endurance performance. The AeroSim aeronautical simulation blockset is a set of MATLAB Simulink based tools that provide rapid development of nonlinear 6-dof aircraft dynamic models [80]. The Aerosonde UAV model is one of the examples from the AeroSim blockset, which provides open loop simulation of the Aerosonde UAV.

In this chapter, the performance data of the Aerosonde UAV is extracted from the AeroSim blockset to define the benchmark conventional gas powered configuration. Next, the Aerosonde UAV model is modified with a fuel cell propulsion system, where the reciprocating engine with fuel tank is replaced with a fuel cell system, an electric motor and a compressed hydrogen tank. The gross weight of the fuel cell powered configuration remains the same as that of the conventional gas powered configuration. The associated fuel cell specification data needed for the adaptation is listed in this chapter. Towards the end of the chapter, the performance of the fuel cell powered configuration is compared against those of the conventional gas powered configuration.

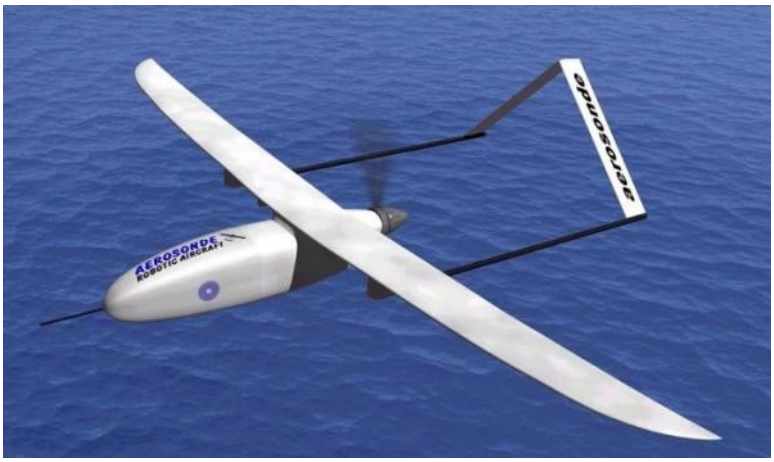

Figure 3.1 Aerosonde UAV from AAI Corporation [79].

3.2 Aerosonde UAV Specifications

The key geometric data of the Aerosonde UAV, extracted from the AeroSim blockset [80], is listed in Table 3.1. The overall lift and draft coefficient as a function of angle of attack is listed in Figure 3.2. The propeller performance data, shown in Figure 3.3, is presented as the non-dimensional thrust coefficient and power coefficient with respect to the propeller inflow ratio. The definitions of the inflow ratio, thrust coefficient, torque coefficient, and power coefficient are given in Equations (3.1) to (3.4). Since the original data from the AeroSim blockset are in the form of discrete data points, polynomial functions have been used to fit the data points to obtain smooth functions for the propeller performance curves.

Inflow ratio:

$$J_{adv} = \frac{\pi V_{\infty}}{\Omega R} \tag{3.1}$$

Thrust coefficient:

$$T = \frac{4}{\pi^2} \rho R^4 \Omega^2 C_T \tag{3.2}$$

Torque coefficient:

$$M = \frac{4}{\pi^3}\rho R^5 \Omega^2 C_P \tag{3.3}$$

Power coefficient:

$$P = \frac{4}{\pi^3}\rho R^5 \Omega^3 C_P \tag{3.4}$$

where V_∞ is the free stream air velocity (m/s), Ω is the propeller rotational speed (rad/s), R is the propeller radius (m), and ρ is the air density (kg/m^3).

Table 3.1 Specifications of the Aerosonde UAV [80].

Empty Weight:	8.5 kg
Gross Weight:	13.5 kg
Wingspan:	2.9 m
Length:	1.74 m
Wing Area:	0.55 m^2

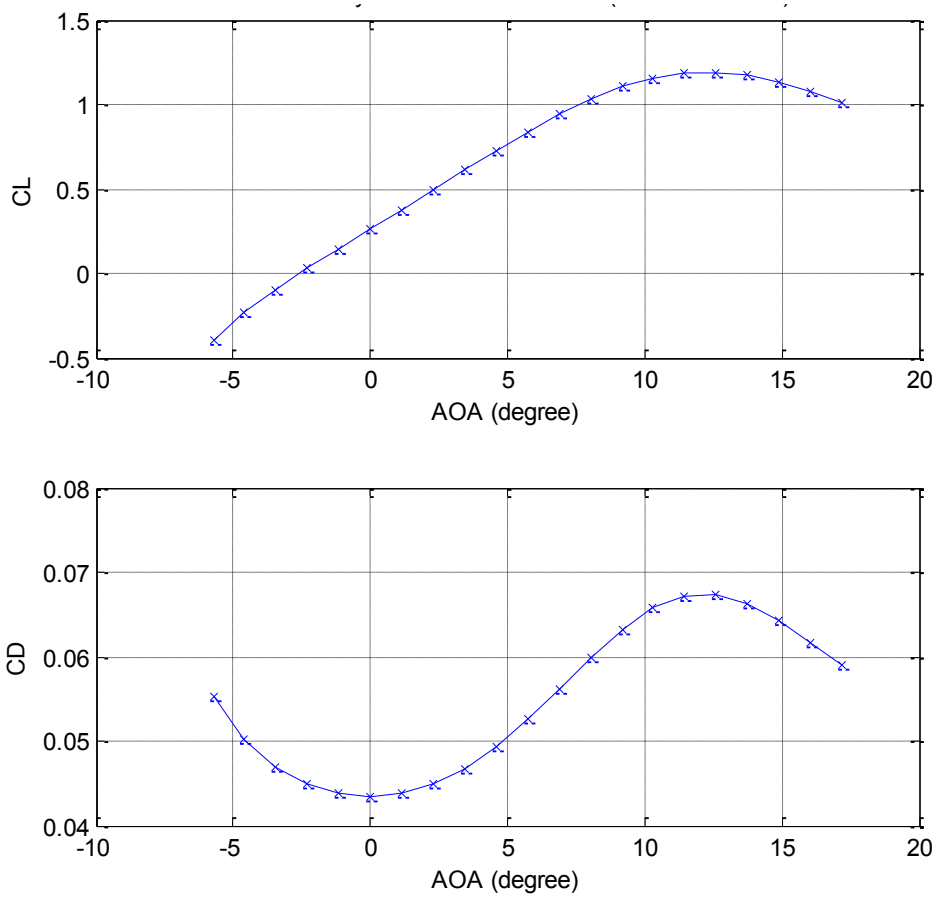

Figure 3.2 Cl, Cd of the Aerosonde UAV model.

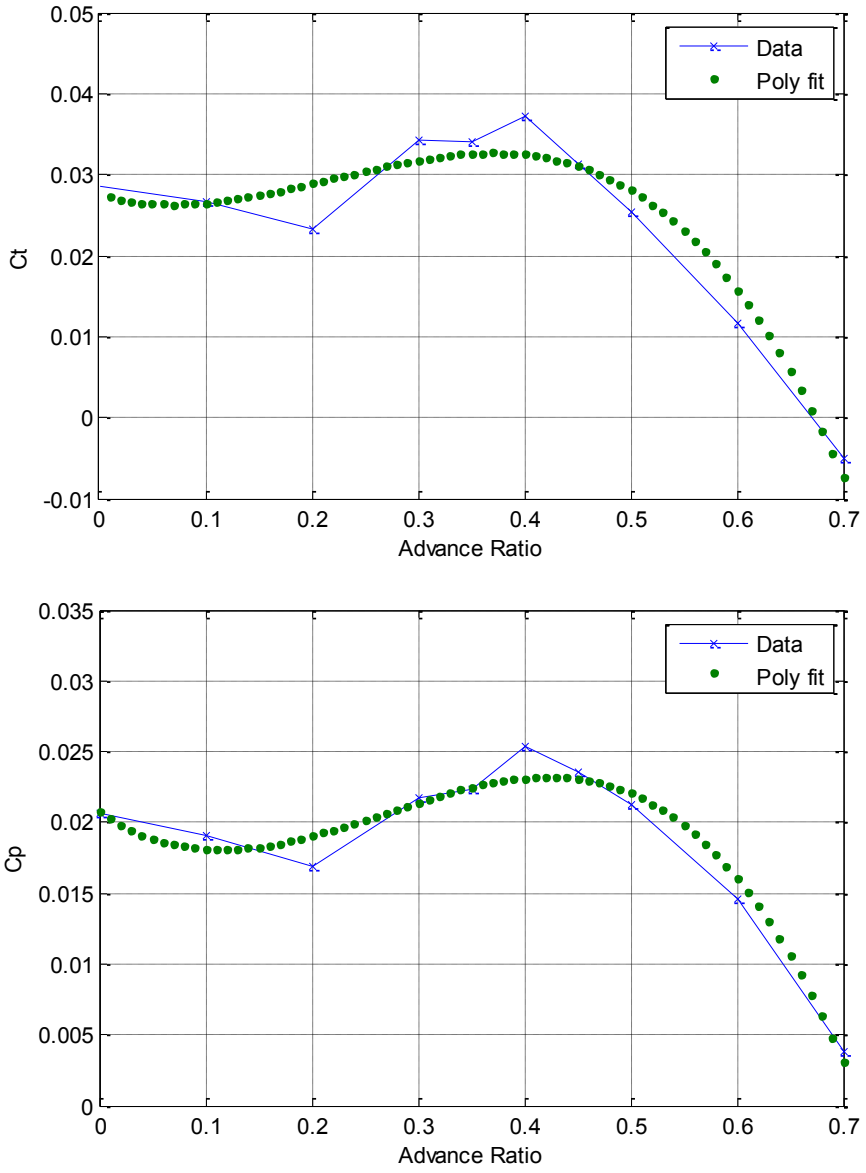

Figure 3.3 Propeller performance data of the Aerosonde UAV.

3.3 Fuel Cell System Selection

To fit an appropriate fuel cell system with the Aerosonde UAV model, information about the weight, size and power is required. Horizon Fuel Cell Technologies offers a wide range of off-the-shelf PEM fuel cell systems from 10W to 5kW [81]. As a fuel cell system can be resized by the number of cells and the cell area, for the current research, a

mass model is developed so that fuel cell systems at other sizes can be used in the analysis. In this study, the cell area is defined as the cross-sectional area (A) of a fuel cell system instead of the active area (A_a). The relation between the cross-sectional area (A) and the active area (A_a) is shown in Equation (3.5), where the coefficients $A_0$and k_c are derived from the manufacturer's data.

$$A_a = A_0 + k_c A \tag{3.5}$$

Table 3.2 shows the physical specifications of the fuel cell systems available from Horizon Fuel Cell Technologies [82], ranging from 100W to 1000W. The weights of different fuel cell system with respect to the number of cells (N) and cell area (A) are used to determine the coefficients in Equation (3.6), and the coefficients are listed in Table 3.3. Figure 3.4 shows the fuel cell weight as a function of the number of cells and the cell area, together with the manufacture's reference data points.

$$M_{fuelcell} = m_0 + m_N * N + m_A * A_c + m_{A,N} * (A * N) \tag{3.6}$$

Table 3.2 Specifications of fuel cell systems from 100W to 1000W [82].

Model	Power (W)	Weight (g)	Cell N (-)	Cell A (cm^2)	Cell Volume (cm^3)	Length (mm)
H-100	100	865	16	108.46	976.14	90.00
H-200	200	1485	32	108.46	1648.59	152.00
H-300	300	2070	48	108.46	2315.62	213.50
H-500	500	2520	24	328.30	5252.80	160.00
H-1000	1000	4000	48	328.30	7189.77	219.00

Table 3.3 Parameters for fuel cell mass model.

m_0 (g)	m_N (g/N)	m_A (g/cm^2)	$m_{A,N}$ (g/(N-cm^2))
-112.4	25.81	3.51	0.11

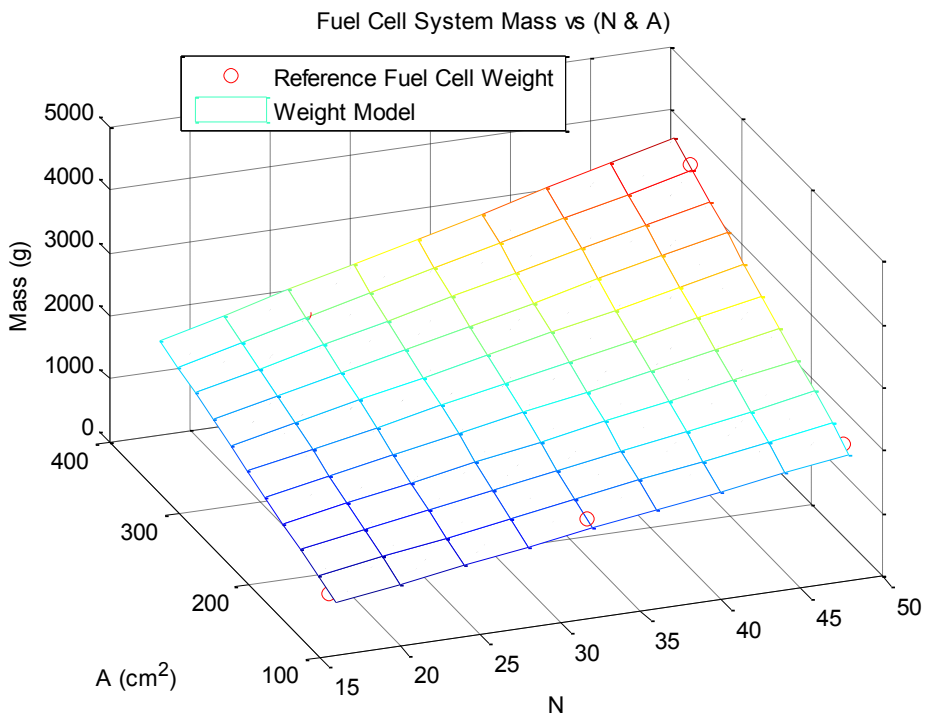

Figure 3.4 Fuel cell system weight model with respect to N and A.

Besides the weight of a fuel cell system, the polarization curve (voltage-current curve) is required to choose an appropriate fuel cell system size. Since the power requirement for the Aerosonde UAV is in the range of 500W to 1000W, for the current research, voltage-current curves of the Horizon H-500 and H-1000 fuel cell systems are used to validate the mathematical model of the fuel cell system. Figure 3.5 shows performance curves of the H-500 and H-1000 fuel cell systems, where the H-500 fuel cell system is rated at 500W maximum power and the H-1000 is rated at 1000W maximum power. Figure 3.6 shows a comparison of the voltage-current curve computed using Equation (2.59) and that of the manufacturer's data. The validated fuel cell performance model is applied to scale the fuel cell system for selecting the appropriate fuel cell system size for the fuel cell powered UAV configuration.

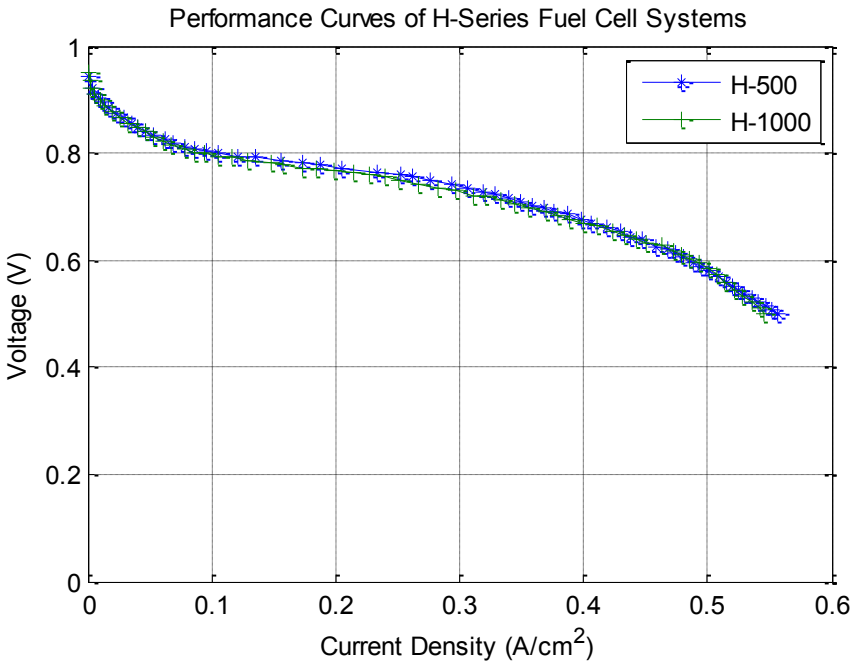

Figure 3.5 Performance curves of H-500 and H-1000 fuel cell systems.

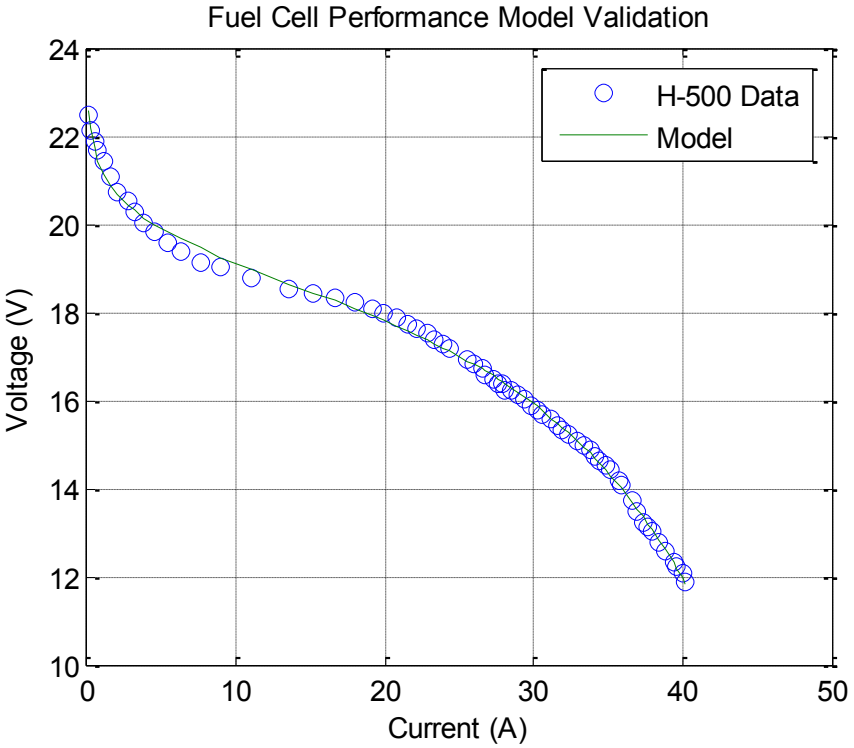

Figure 3.6 Fuel cell performance model validation.

With the fuel cell system mass model (Equation (3.6)) and fuel cell system performance model (Figure 3.6), a few candidate fuel cell systems are selected with the number of cells ranging from 36 to 64 and the cell area from 200 cm^2 to 300 cm^2. The calculated weight and maximum power for the candidate fuel cells are listed in Table 3.4 and Table 3.5. As shown in Figure 3.7, the power capability of a fuel cell system increases with an increase in it weight. The power to weight ratio of the reciprocating engine of the Aerosonde UAV is also shown in Figure 3.7. It can be observed that the power densities of the fuel cell systems are much lower than that of the reciprocating engine.

The same gross weight for the conventional gas powered configuration is maintained for the fuel cell powered configuration. The weight breakdowns are shown in Table 3.6. The weight of the hydrogen tank is referenced from the Ion Tiger fuel cell powered UAV [83]. The weight allowance for the fuel cell system and the electric motor is 3.6 kg, where 0.6 kg is allocated to the electric motor [71]. The corresponding maximum power is less than 700W. The performance of the fuel cell configuration is expected to be poorer than that of the conventional gas powered configuration. The detail performance comparisons of the two configurations are presented in the next section.

Table 3.4 Weight information of candidate fuel cell systems.

Fuel cell system weight (kg)	A=200 cm^2	A=250 cm^2	A=300 cm^2
N=36	2.3	2.7	3.0
N=48	2.9	3.3	3.8
N=64	3.6	4.2	4.7

Table 3.5 Maximum power rating of candidate fuel cell systems.

Fuel cell system Max. Power (W)	A=200 cm^2	A=250 cm^2	A=300 cm^2
N=36	469	586	703
N=48	625	781	937
N=64	833	1041	1250

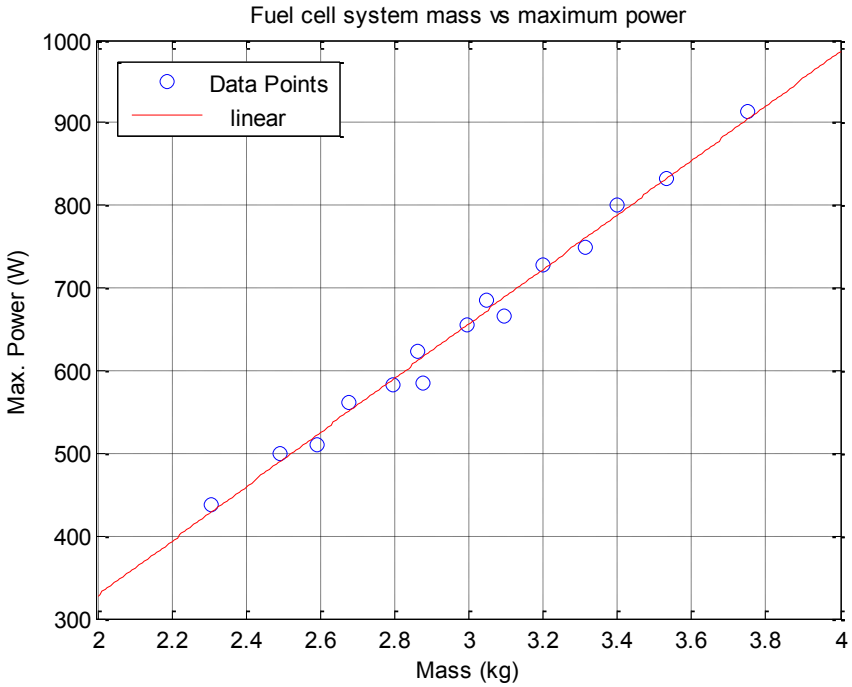

Figure 3.7 Fuel cell system maximum power with respect to weight.

Table 3.6 Weight breakdowns of the conventional gas powered configuration and the fuel cell powered configuration.

	Conventional Gas Powered Configuration	Fuel Cell Powered Configuration
Airframe	3.6 kg	3.6 kg
Avionics/Payload	2.1 kg	2.1 kg
Power Plant	2.2 kg	**3.6 kg (motor and fuel cell)**
Fuel + Tank Weight	5.6 kg (5 kg fuel)	4.2 kg (600 gm H_2)
Gross Weight	13.5 kg	13.5 kg

3.4 Steady State Performance Evaluation

After the Aerosonde UAV model is modified with a fuel cell system, its flight performance is evaluated and compared to that of the conventional gas powered configuration. During the fuel cell adaptation process, the airframe and the gross weight of both configurations are kept identical. It is observed that the two propulsion system of these two configurations differed in both maximum available and specific fuel consumption rate.

The fuel consumption rate of the Aerosonde UAV is obtained from both the AeroSim blockset [80] and the engine development report [84]. The data from both sources are shown in Figure 3.8, where a curve fitting model in the form of Equation (3.7) is applied. It can be observed that the specific fuel consumption rate of the conventional reciprocating engine decreases as the power increases, which reaches to almost constant when the engine power is more than 400W.

$$\dot{m}_{gas} = a\,log(P) + b + \frac{c}{P} \tag{3.7}$$

The polarization curve of the selected fuel cell system is shown in Figure 3.9, and the fuel consumption rate is shown in Figure 3.10. Different from that of the conventional reciprocating engine, the specific fuel consumption rate of a fuel cell increases when the power increases. Because the energy density of hydrogen is much higher than that of gasoline, the fuel consumption rate of the fuel cell system is only a fraction of that of the conventional reciprocating engine. For example, at 400W, the fuel consumption rate of the conventional reciprocating engine is about 140 g/hr. The fuel consumption rate of the fuel cell system at 400W is only 20 g/hr.

The endurance estimations of both the conventional gas powered configuration and the fuel cell powered configuration are presented in Figure 3.11 and Figure 3.12. Although the fuel consumption rate of the fuel cell powered configuration is significantly lower than that of the conventional gas powered configuration, its endurance performance is inferior to that of the conventional gas powered configuration. This is due to the constraint that only 600 grams of fuel (compressed hydrogen) is carried for the fuel cell powered configuration, as compared to 5 kg of fuel for the conventional gas powered configuration.

Since the airframes for both configurations are identical, both the maximum speed and the maximum rate of climb are determined only by the maximum available power. The reciprocating engine of the conventional gas powered configuration is rated at 1000W, and the maximum power of the selected fuel cell system is only 672W. The differences in the maximum speeds for both configurations are shown in Figure 3.13. The comparisons of their maximum rate of climb at different speeds are shown in Figure 3.14. Both the maximum speed and maximum rate of climb of the fuel cell powered configuration are inferior to those of the conventional gas powered configuration.

Due to the lower available power from the fuel cell system, the flight trajectories of the fuel cell powered configuration are more likely to be constrained by the maximum available power. Optimal trajectories that do not consider the propulsion system characteristics are likely to be unfeasible. For example, if the fuel cell powered configuration is to travel from point A to point B and the height difference between these two points is significant, the minimum fuel optimal trajectory obtained for the conventional gas powered configuration is most likely not feasible for the fuel cell

powered configuration. Trajectory optimization considering the fuel cell system dynamics is required to minimize the fuel consumption for a fuel cell powered UAV.

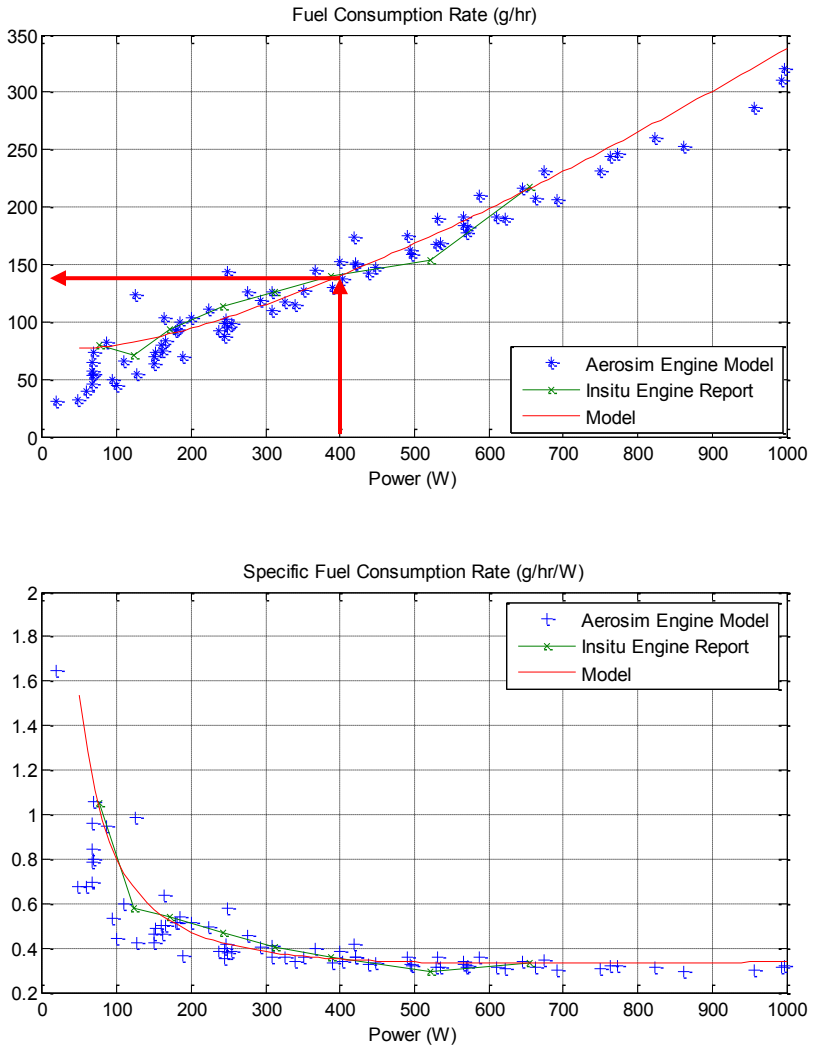

Figure 3.8 Fuel consumption rate and specific fuel consumption rate of the original gas powered internal combustion engine.

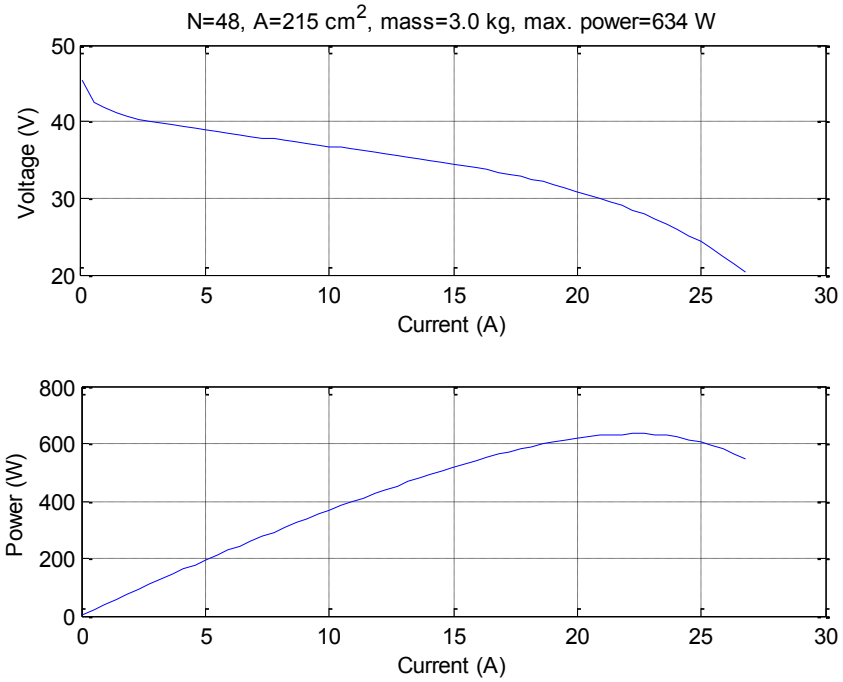

Figure 3.9 Polarization curve of the selected fuel cell system.

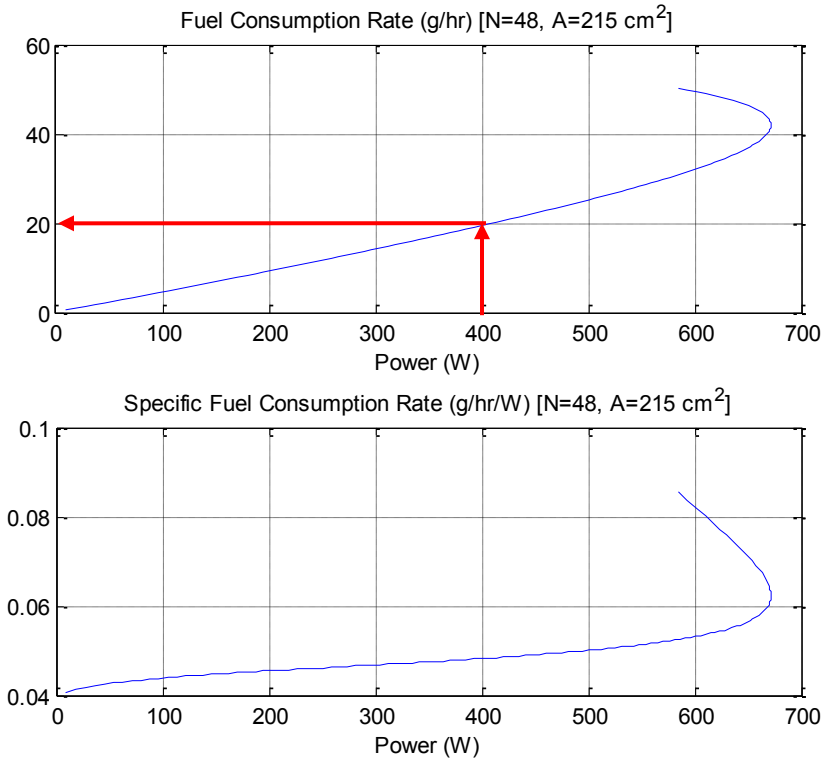

Figure 3.10 Fuel consumption rate and specific fuel consumption rate of the selected fuel cell system.

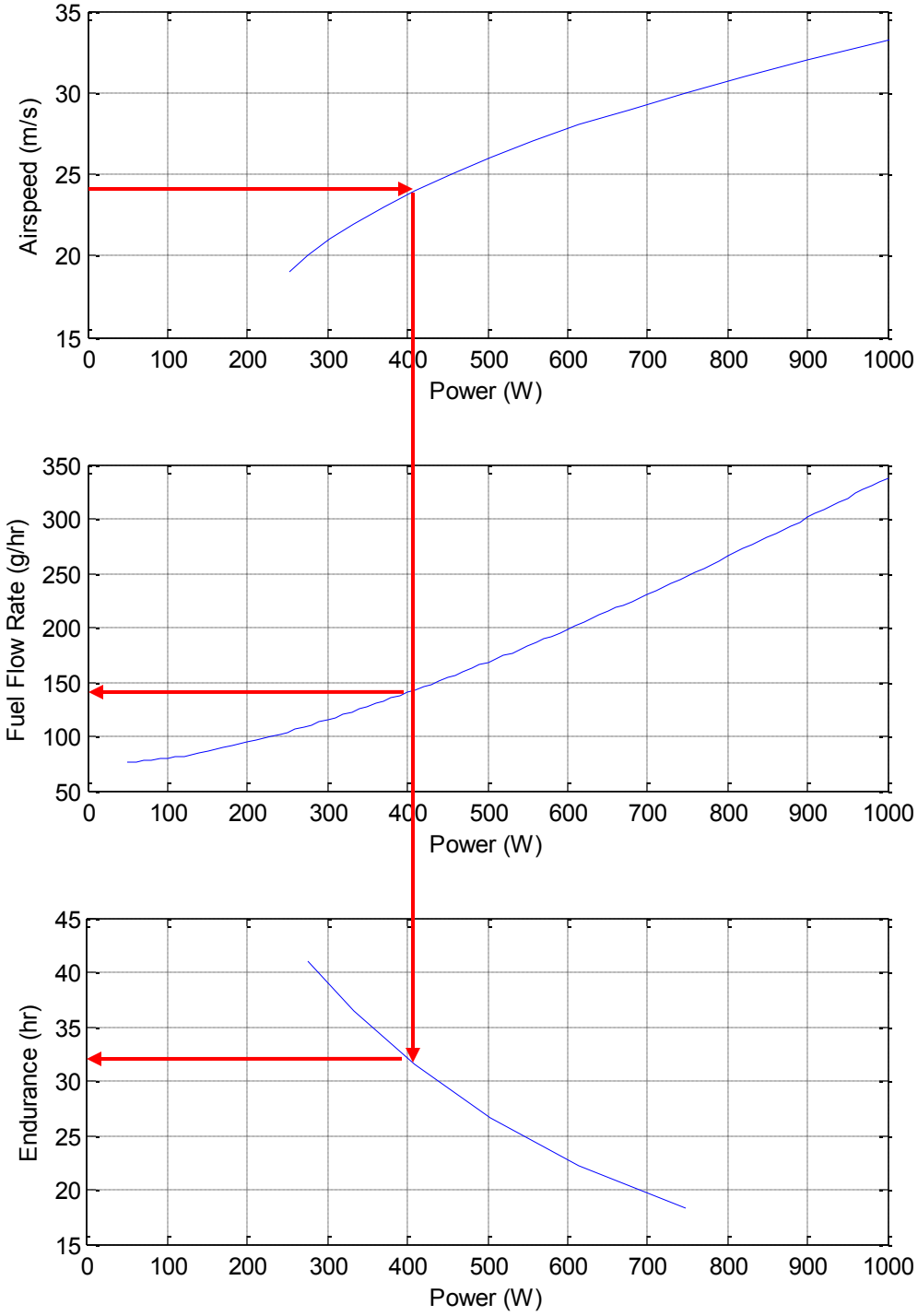

Figure 3.11 Endurance estimation for the conventional gas powered configuration.

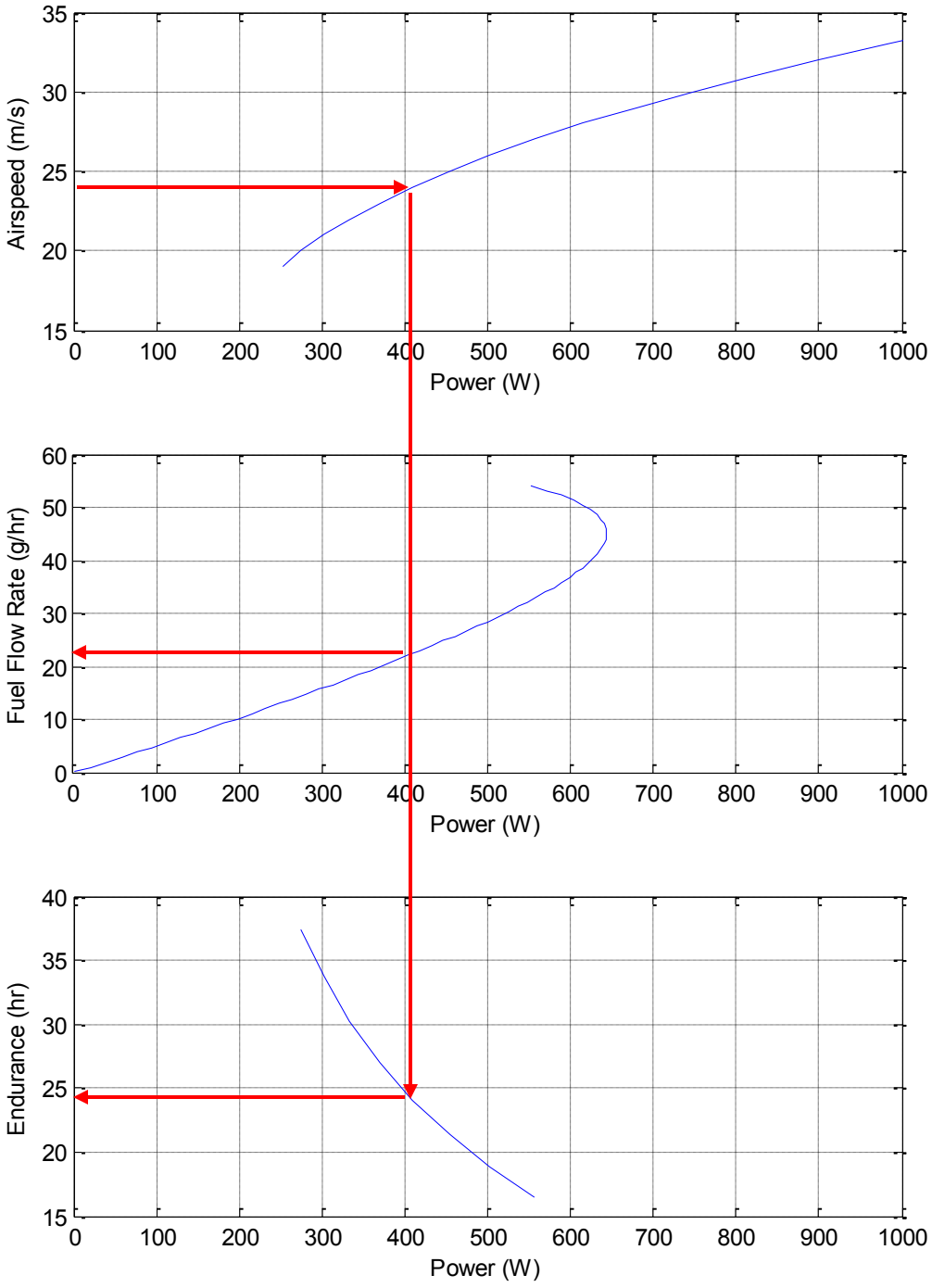

Figure 3.12 Endurance estimation for the fuel cell powered configuration.

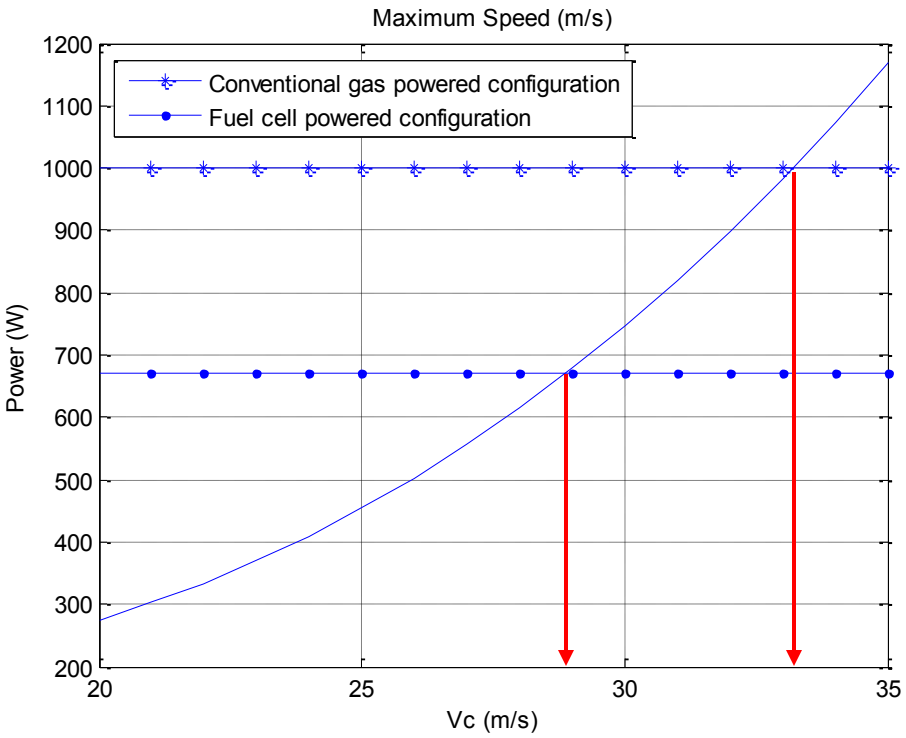

Figure 3.13 Performance comparison (maximum speed).

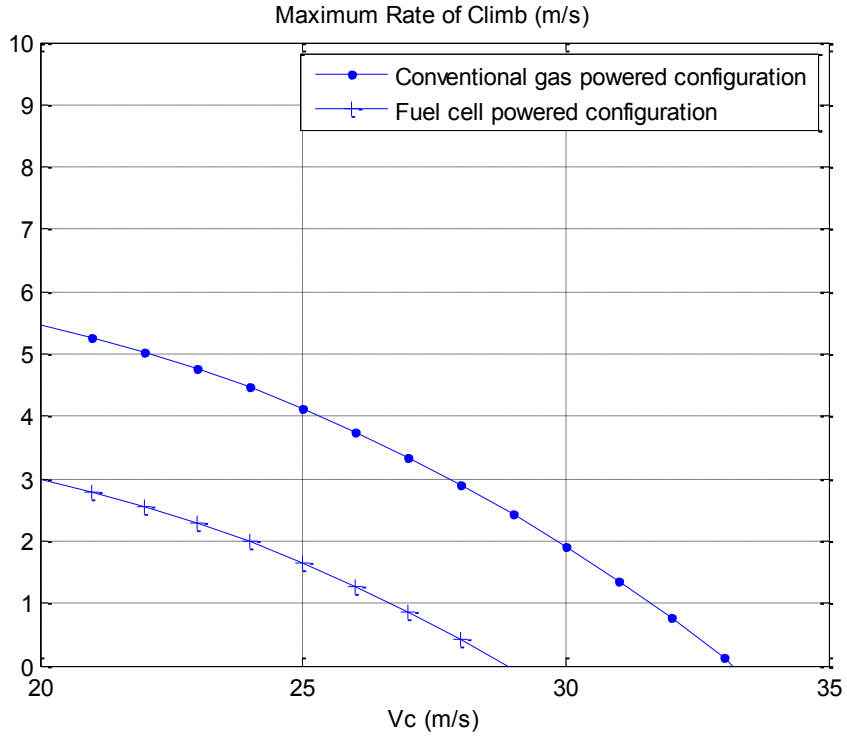

Figure 3.14 Performance comparison (maximum rate of climb).

3.5 Summary

In this chapter, a fuel cell powered UAV configuration was obtained by modifying the Aerosonde UAV with a fuel cell powered propulsion system, where a fuel cell system was sized based on the fuel cell system performance and weight data. The gross weight of the fuel cell powered configuration was kept the same as that of the conventional gas powered configuration. The performance of both configurations was compared, including the specific fuel consumption rates, endurances, maximum speeds, and maximum rates of climb. The performance of the fuel cell configuration was inferior to that of the conventional gas powered configuration due to the lower available power of the fuel cell system. Due to the lower available power, trajectory optimization is more likely required to find feasible flight trajectories.

CHAPTER 4

A GENERALIZED FRAMEWORK FOR PSEUDOSPECTRAL METHODS

4.1 Introduction

An optimal control problem (or a trajectory optimization problem) is to find the control variables that satisfy the dynamic constraints and, at the same time, minimize the performance index function. For a fuel cell powered UAV, the dynamic constraint equations are obtained by combining the point mass UAV model and the dynamic model of a fuel cell powered UAV propulsion system. Due the nonlinearities in these dynamic equations, it is very difficult to find analytic solutions. Instead, numerical methods are used to solve the trajectory optimization problems.

Among the different numerical methods for optimal control problems, pseudospectral methods are a class of state and control parameterization methods, where a finite basis of interpolating polynomials is used to approximate the states and controls. The main difference between a pseudospectral method and other state and control parameterization methods is that the interpolating polynomials are orthogonal at the discretization points. The main advantage of pseudospectral methods is that the approximation of the derivatives and the integrations for smooth functions exhibit spectral accuracy [60].

The first application of spectral methods to optimal control problems was introduced by [85] in 1988, where Chebyshev polynomials were used as the interpolating polynomials. In 1995, Ref. [62] proposed the Legendre pseudospectral method (LPM),

where Lagrange polynomials collocated at the Legendre-Gauss-Lobatto (LGL) points were used as the interpolating polynomials. In 2001, Ref. [86] extended the Legendre pseudospectral method to generate costate estimates. Around the same time, Ref. [61] introduced the Chebyshev pseudospectral method (CPM), where Lagrange polynomials collocated at the Chebyshev-Gauss-Lobatto (CGL) points were used. In 2005, Ref. [87] proposed another pseudospectral method for infinite-horizon nonlinear optimal control problems based on Lagrange polynomials collocated at the Legendre-Gauss-Radau (LGR) points [87]. The Gauss pseudospectral method (GPM) was proposed by [57] in 2005, and the Radau pseudospectral method (RPM) for finite-horizon problems was proposed by [88] in 2011.

Among different pseudospectral methods, there are four pseudospectral methods that are based on Lagrange polynomials, namely, the LPM [62], the CPM [61], the GPM [57], and the RPM [88]. Due to the similarities in these pseudospectral methods, several comparisons and unified frameworks have been discussed in the literature. In [89], the LPM, GPM and RPM were compared with continuous Mayer problems. In [90], a unified view of the LPM, GPM, and RPM was presented to show the similarities and differences in these methods. In [91], pseudospectral methods on arbitrary grids were proposed to unify the LPM and CPM. In [63], a unified framework was presented for the GPM and RPM, where the collocation points of these two methods do not include all the end points.

A pseudospectral method converts an optimal control problem to an NLP problem which requires an NLP solver to find the solution. Software packages based on pseudospectral methods are often available in paired packages of one pseudospectral method and one NLP solver. For example, the PSOPT [65] is a pair package of the

Legendre pseudospectral method and the IPOPT solver, the GPOPS [66] is a paired package of the Radau pseudospectral method and the SNOPT solver, and the DIDO [67] has its own proprietary NLP solver. The solution of an optimal control problem, which is also the solution of a transcribed NLP problem, is highly influenced by the choice of the NLP solver. In addition, the performances of different pseudospectral methods are different for different problems [63]. A generalized framework for different pseudospectral methods with the same NLP solver is desired to evaluate different pseudospectral methods.

This chapter proposes a generalized framework for the four pseudospectral methods based on the Lagrange polynomials. Different from other unified frameworks, the generalized framework includes all four pseudospectral methods, where only the collocation points are required to define a pseudospectral method. The equivalences between the pseudospectral methods implemented with the proposed framework and the original pseudospectral methods are verified through comparisons on the differentiation matrices and the quadrature weights for integration. Example problems are used to compare the performance of different pseudospectral method defined by different collocation points. The proposed framework is also used to evaluate a new pseudospectral method that is based on Lagrange polynomials collocated at new set of collocation points.

4.2 Approximation with Lagrange Polynomials

Lagrange polynomials [92] are commonly used for interpolation. For a given set of N distinct pairs of data points $(t_1, x_1), \cdots, (t_i, x_i), \cdots, (t_N, x_N)$, the interpolation

polynomial in the Lagrange form, $L(t)$, is a linear combination of Lagrange basis polynomials, $\varphi_i(t)$, as follows:

$$x(t) \approx L(t) = \sum_{i=1}^{N} x_i \varphi_i(t) \tag{4.1}$$

$$\varphi_i(t) = \prod_{\substack{j \neq i \\ 1 \leq j \leq N}} \frac{(t - t_j)}{(t_i - t_j)} \tag{4.2}$$

It is the polynomial of the least degree that has exact function values at the given data points.

$$x_i = x(t_i) = L(t_i), \qquad i = 1, \cdots, N \tag{4.3}$$

The basis function $\varphi_i(t)$ has the following property:

$$\varphi_i(t_j) = \begin{cases} 1 & i = j \\ 0 & i \neq j \end{cases} \tag{4.4}$$

Figure 4.1 shows an example of Lagrange polynomials with four collocation points.

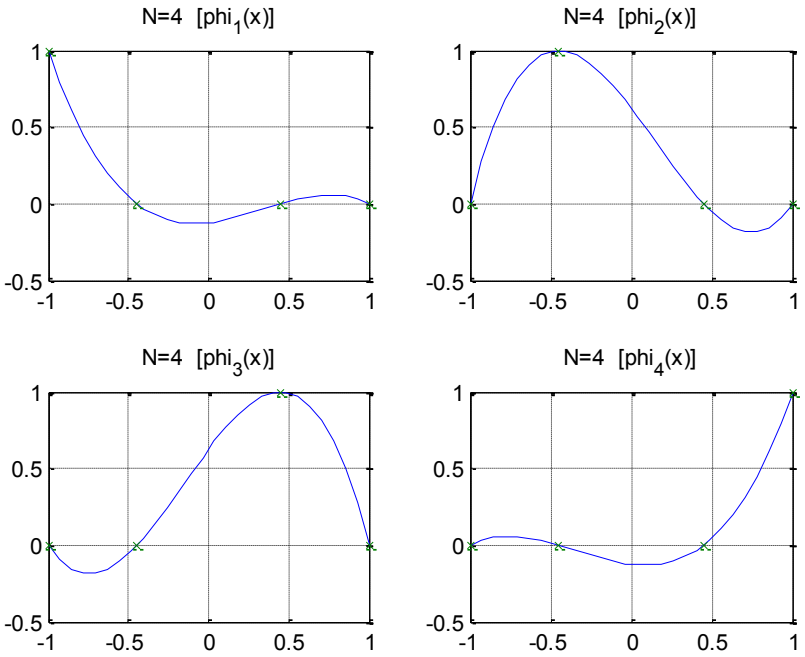

Figure 4.1 Basis functions of Lagrange polynomial.

With a polynomial approximation of $x(t)$, the integration of function $g(x(t),t)$ can be approximated by summation of the function values evaluated at collocation points, $g(x(t_i),t_i)$, weighted by the corresponding quadrature weights for integration [93].

$$\int_{-1}^{1} g(x(t),t)dt \approx \sum_{i=1}^{N} w_i \cdot g(x(t_i),t_i) \tag{4.5}$$

$$w_i = \int_{-1}^{1} \varphi_i(t)dt \tag{4.6}$$

The differentiation of $x(t)$ with respect to time $\dot{x}(t)$ is approximated as follows:

$$\dot{x}(t) \approx \sum_{i=1}^{N} x_i \dot{\varphi}_i(t) \tag{4.7}$$

$$\dot{x}(t_j) \approx \sum_{i=1}^{N} x_i \dot{\varphi}_i(t_j) = \sum_{i=1}^{N} D(j,i) \cdot x_i \tag{4.8}$$

$$\dot{\varphi}_i(t_j) = \frac{\sum_{\substack{j\neq i \\ 1\leq j\leq N}} \left(\prod_{\substack{k\neq i \\ k\neq j \\ 1\leq k\leq N}} (t - t_k) \right)}{\prod_{\substack{j\neq i \\ 1\leq j\leq N}} (t_i - t_j)} \tag{4.9}$$

$$D(j,i) = \dot{\varphi}_i(t_j) = \frac{\sum_{\substack{k\neq i \\ 1\leq k\leq N}} \left(\prod_{\substack{j\neq i \\ j\neq k \\ 1\leq j\leq N}} (t - t_j) \right)}{\prod_{\substack{j\neq i \\ 1\leq j\leq N}} (t_i - t_j)} \tag{4.10}$$

In summary, for a given set of data points, $(t_1,x_1),\cdots,(t_i,x_i),\cdots,(t_N,x_N)$, the function $x(t)$ can be approximated by the summation of a set of Lagrange polynomials. The integration of the function $g(x(t),t)$ can be approximated by weighted summation of the function values. The differentiation of the function with respect to time $\dot{x}(t)$ can be approximated by the product of the differentiation matrix and the associated function values. The quadrature weight (Equation (4.6)) and the differentiation matrix (Equation (4.10)) for an arbitrary grid are computed by using the MATLAB functions developed in [94] and [95].

The data point locations $\{t_1, \cdots, t_N\}$ determine the exact Lagrange polynomial being used for the approximations. The data points $\{t_1, \cdots, t_N\}$ are also known as the collocation points. In the literature of pseudospectral methods for optimal control, there are four sets of well-known collocation points, the Legendre Gauss-Lobatto (LGL) points, the Chebyshev-Gauss-Lobatto (CGL) points, the Legendre-Gauss (LG) points and the Legendre-Gauss-Radau (LGR) points. The LGL, LG, and LGR points are defined based on the zeros of different forms of the Legendre polynomials $L_k(t)$.

The Legendre polynomials $L_k(t),\ k = 0, 1, \cdots$ are the eigenfunctions of the singular Sturm-Liouville problem [93].

$$\left((1 - t^2)L_k'(t)\right)' + k(k+1)L_k(t) = 0 \tag{4.11}$$

The Legendre polynomial $L_k(t)$ satisfies the following recursive relation:

$$\begin{gathered} L_{k+1}(t) = \frac{2k+1}{k+1} t L_k(t) - \frac{k}{k+1} L_{k-1}(t) \\ L_0(t) = 1 \\ L_1(t) = t \end{gathered} \tag{4.12}$$

The grid locations for the four pseudospectral methods are defined as follows:

Legendre-Gauss-Lobatto (LGL) points:

$$t_0 = -1, t_N = 1, t_j\ (j = 1, \cdots, N-1)\ \textit{are zeros of}\ L_N' \tag{4.13}$$

Chebyshev-Gauss-Lobatto (CGL) points:

$$t_j = -cos\left(\frac{j}{N}\pi\right), \qquad j = 0, \cdots, N \tag{4.14}$$

Legendre-Gauss (LG) points:

$$t_j\ (j = 0, \cdots, N)\ \textit{are zeros of}\ L_{N+1} \tag{4.15}$$

Legendre-Gauss-Radau (LGR) points:

$$t_j\ (j = 0, \cdots, N)\ \textit{are zeros of}\ L_N + L_{N+1} \tag{4.16}$$

Figure 4.2 shows the collocation points for the four methods and the uniform grid points. Both the CGL and the LGL points, which include both end points at -1 and 1, are defined in $[-1, 1]$ The LG points, which do not include any of the end points, are defined in $(-1,1)$. The LGR points, which include only the end point at -1, are defined in $[-1,1)$. As compared to the uniformly distributed points, all the other collocation points are denser toward the two ends at -1 and 1.

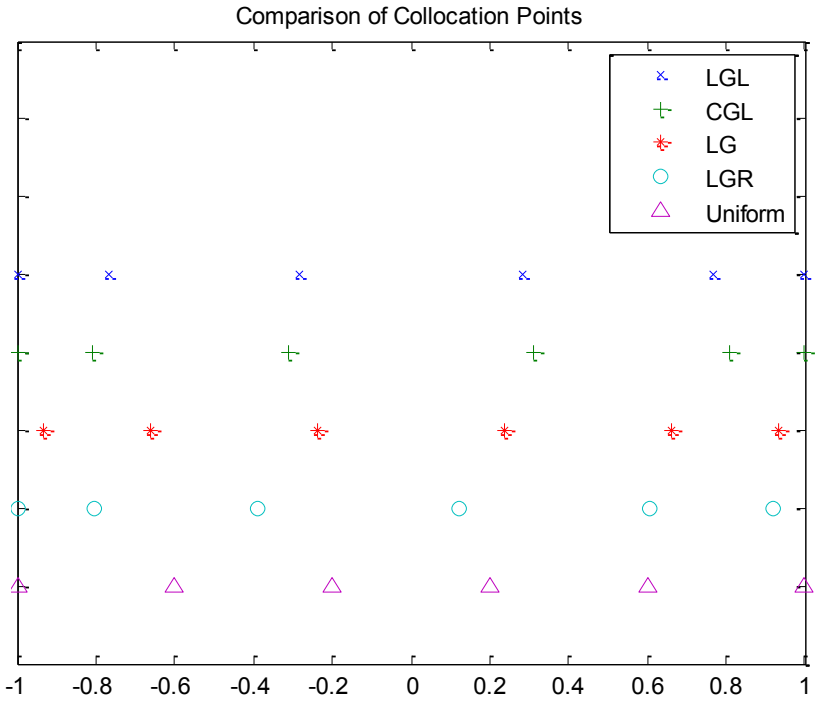

Figure 4.2 Collocation points for different pseudospectral methods.

With the collocation points defined for various methods, the approximation accuracy for interpolation, differentiation, and integration are evaluated using a simple continuous function e^t.

$$\begin{cases} x(t) = e^t \\ \dot{x}(t) = e^t \\ \int_{-1}^{1} x^2(t)dt = 0.5(e^2 - e^{-2}) = 3.6269 \end{cases} \tag{4.17}$$

Figure 4.3 shows the improvement of interpolation error with respect to the number of collocation points. Except the approximation with uniformly distributed points, the interpolation errors for all other methods are close to machine zero (10^{-16}) with more than 15 collocation nodes. The differentiation error shows a similar trend. When the number of the collocation points is more than 13, the results from the uniform grid fails to improve further. This phenomenon is referred to as the Runge phenomenon [96]. From this, it can be concluded that uniformly distributed points are not suitable for a pseudospectral method. The integration error does not achieve machine zero when the interpolation error achieves machine zero. This is due to the numerical error in the computation of integration weights.

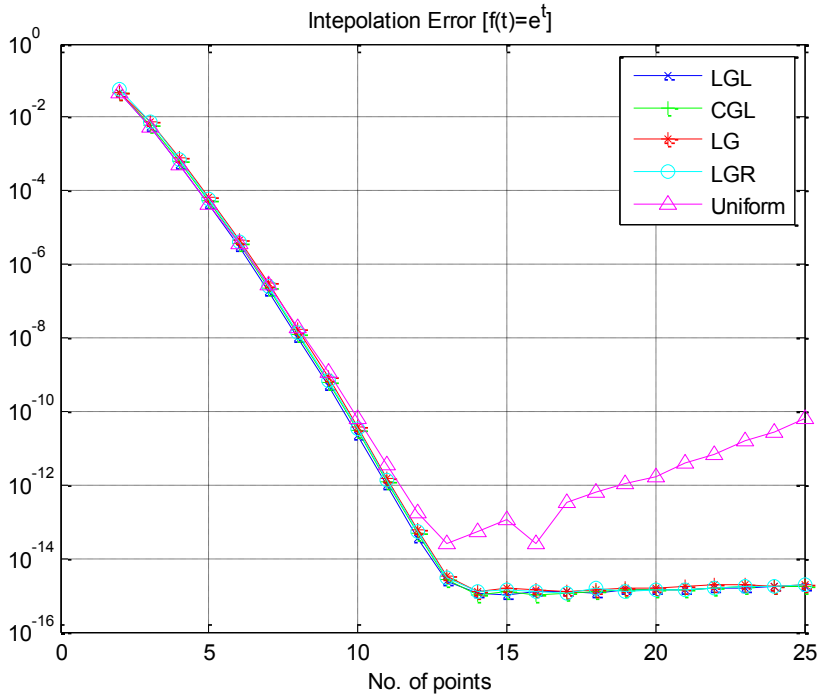

Figure 4.3 Interpolation error trend with respect to number of nodes.

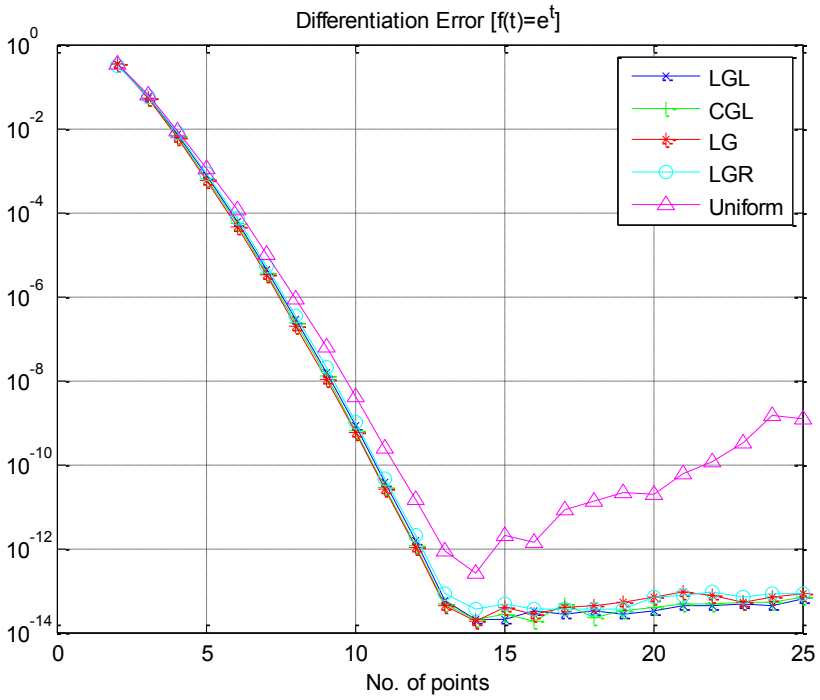

Figure 4.4 Differentiation error trend with respect to number of nodes.

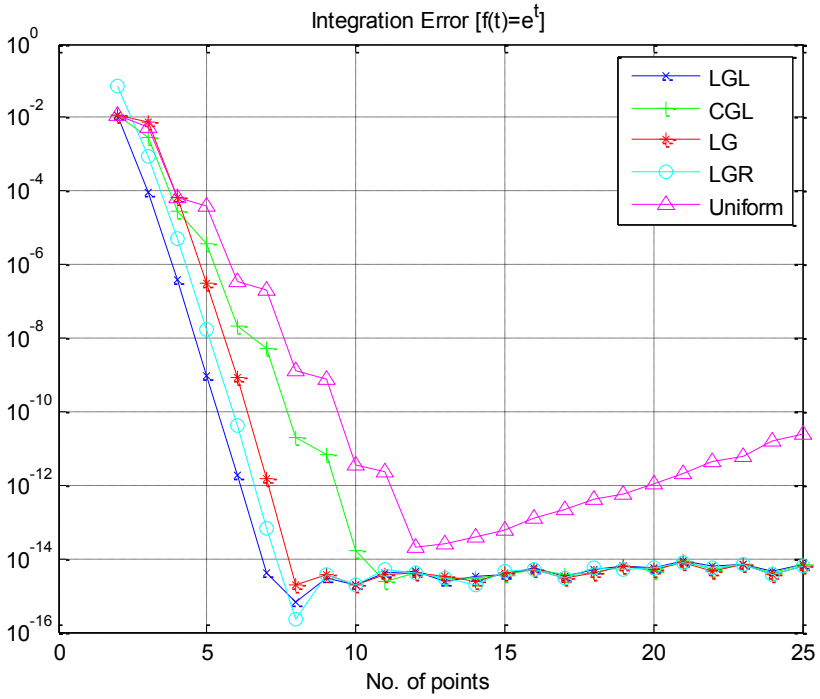

Figure 4.5 Integration error trend with respect to number of nodes.

4.3 Transcription Equations for the Generalized Framework

The proposed generalized framework transcribes an optimal control problem to an NLP problem. The corresponding transcription equations are the same as those for the Legendre pseudospectral method [62].

Consider an optimal control problem where the objective is to find states $x(t) \in \mathcal{R}^n$ and controls $u(t) \in \mathcal{R}^n$ on the interval $t \in [t_0, t_f]$ that minimize a cost in the Bolza form [56]. The cost is

$$J = \Phi\big(x(t_f), t_f\big) + \int_{t_0}^{t_f} g(x(t), u(t), t)\, dt \tag{4.18}$$

where $\Phi: \mathcal{R}^n \times \mathcal{R} \to \mathcal{R}$ is the terminal cost and $g: \mathcal{R}^n \times \mathcal{R}^m \times \mathcal{R} \to \mathcal{R}$ is the integral cost. The states are subject to the differential dynamic constraints,

$$\frac{dx}{dt} = f(x(t), u(t), t) \tag{4.19}$$

where $f: \mathcal{R}^n \times \mathcal{R}^m \times \mathcal{R} \to \mathcal{R}^n$. The states are also subject to the boundary conditions in the form,

$$\psi\big(x(t_0), t_0, x(t_f), t_f\big) = 0 \tag{4.20}$$

where $\psi: \mathcal{R}^n \times \mathcal{R} \times \mathcal{R}^m \times \mathcal{R} \to \mathcal{R}^q$.

The standard grid points are defined on the interval $[-1, 1]$. The first step is to change the time interval of the optimal control problem from $t \in [t_0, t_f]$ to $\tau \in [-1, 1]$. This is done by the linear mapping

$$t = \frac{t_f - t_0}{2}\tau + \frac{t_f + t_0}{2} \tag{4.21}$$

With this mapping, the optimal control problem can be replaced as follows:

Minimize the cost

$$J = \Phi\big(x(1), t_f\big) + \frac{t_f - t_0}{2}\int_{-1}^{1} g(x(\tau), u(\tau), \tau)\, d\tau \tag{4.22}$$

subject to dynamic constraints

$$\frac{dx}{d\tau} = \left(\frac{t_f - t_0}{2}\right) f(x(\tau), u(\tau), \tau) \tag{4.23}$$

and boundary conditions

$$\psi\big(x(-1), t_0, x(1), t_f\big) = 0 \tag{4.24}$$

Discretizing the dynamic constraints requires the states and controls to be approximated by using a set of Lagrange interpolating polynomials at the N collocation points.

$$x(t) \approx X(t) = \sum_{i=1}^{N} x(t_i) \cdot \varphi_i(t) \tag{4.25}$$

$$u(t) \approx U(t) = \sum_{i=1}^{N} u(t_i) \cdot \varphi_i(t) \tag{4.26}$$

where $t_i, i = 1, \cdots, N$, are the grid points and $\varphi_i(t)$ are the Lagrange polynomials of degree N-1. From the property of the Lagrange polynomials, $\varphi_i(t_k) = \delta_{ki}$, it follows that

$$x(t_i) = X(t_i) \tag{4.27}$$

$$u(t_i) = U(t_i) \tag{4.28}$$

The time derivatives of the states are approximated by the time derivatives of the interpolation polynomials. The derivatives at the grid points are evaluated as follows:

$$\frac{dx}{dt}(t_k) \approx \frac{dX}{dt}(t_k) = \sum_{i=1}^{N} X(t_i) \cdot D_{ki} \quad , \qquad k = 1, \cdots, N \tag{4.29}$$

The derivative matrix D is defined by the derivative of the Lagrange polynomials at the grid points.

$$D_{ki} = \frac{d\varphi_i}{dt}(t_k) \tag{4.30}$$

The derivative matrix allows the dynamic equations to be collocated at the grid points. The resulting algebraic constraints are

$$\frac{2}{(t_f - t_0)} \sum_{i=1}^{N} D_{ki} \cdot X_i = f(X_k, U_k, t_k), \qquad k = 1, \cdots, N \tag{4.31}$$

The boundary constrains are enforced as follows:

$$\psi(X_1, t_0, X_N, t_f) = 0 \tag{4.32}$$

The integration in the cost function is discretized using the quadrature rule as follows:

$$J = \Phi(X_N, t_f) + \frac{(t_f - t_0)}{2} \sum_{k=1}^{N} g(X_k, U_k, t_k) \cdot w_k \tag{4.33}$$

where w_k are the integration weights.

In summary, the continuous optimal control problem is discretized to an NLP problem, where the objective is to find the variables, $X_k \in \mathcal{R}^n$, $U_k \in \mathcal{R}^m$, $k = 1, \cdots, N$ and $t_0, t_f \in \mathcal{R}$ that

minimize the cost

$$J = \Phi(X_N, t_f) + \frac{(t_f - t_0)}{2} \sum_{k=0}^{N} g(X_k, U_k, t_k) \cdot w_k \tag{4.34}$$

subject to

$$\frac{2}{(t_f - t_0)} \sum_{k=0}^{N} D_{ki} \cdot X_i = f(X_k, U_k, t_k) \tag{4.35}$$

$$\psi(X_1, t_0, X_N, t_f) = 0 \tag{4.36}$$

4.4 Generalization of Different Pseudospectral Methods

The four pseudospectral methods, the Legendre pseudospectral methods (LPM), the Chebyshev pseudospectral method (CPM), the Gauss pseudospectral method (GPM), and the Radau pseudospectral method (RPM), are based on Lagrange polynomials at different

collocation points. The transcription equations of each method are compared in [97]. In all four pseudospectral methods, the states and controls in the continuous domain from t_0 to t_f are mapped to the discrete domain from $\tau_0$to τ_{N+1}, where $\tau_0 = -1$ and $\tau_{N+1} = 1$. The transcription equations for the differential constraints and the performance index function are summarized below. In addition, the transcription equations of the proposed generalized framework (GFW) are also presented with the same collocation index as in [97].

Discretization of states:

$$\begin{bmatrix} x(t_0) \\ \vdots \\ \vdots \\ \vdots \\ x(t_f) \end{bmatrix} \rightarrow \begin{bmatrix} X(\tau_0) \\ X(\tau_1) \\ \vdots \\ X(\tau_N) \\ X(\tau_{N+1}) \end{bmatrix} \tag{4.37}$$

Differential constraints approximation:

LPM
$$\begin{bmatrix} \dot{X}(\tau_0) \\ \dot{X}(\tau_1) \\ \vdots \\ \dot{X}(\tau_N) \\ \dot{X}(\tau_{N+1}) \end{bmatrix} = [D^{LPM}] \begin{bmatrix} X(\tau_0) \\ X(\tau_1) \\ \vdots \\ X(\tau_N) \\ X(\tau_{N+1}) \end{bmatrix} = \frac{t_f - t_0}{2} \begin{bmatrix} F\big(\tau_0, X(\tau_0), U(\tau_0)\big) \\ F\big(\tau_1, X(\tau_1), U(\tau_1)\big) \\ \vdots \\ F\big(\tau_N, X(\tau_N), U(\tau_N)\big) \\ F\big(\tau_{N+1}, X(\tau_{N+1}), U(\tau_{N+1})\big) \end{bmatrix} \tag{4.38}$$

CPM
$$\begin{bmatrix} \dot{X}(\tau_0) \\ \dot{X}(\tau_1) \\ \vdots \\ \dot{X}(\tau_N) \\ \dot{X}(\tau_{N+1}) \end{bmatrix} = [D^{CPM}] \begin{bmatrix} X(\tau_0) \\ X(\tau_1) \\ \vdots \\ X(\tau_N) \\ X(\tau_{N+1}) \end{bmatrix} = \frac{t_f - t_0}{2} \begin{bmatrix} F(\tau_0, X(\tau_0), U(\tau_0)) \\ F(\tau_1, X(\tau_1), U(\tau_1)) \\ \vdots \\ F(\tau_N, X(\tau_N), U(\tau_N)) \\ F(\tau_{N+1}, X(\tau_{N+1}), U(\tau_{N+1})) \end{bmatrix} \tag{4.39}$$

GPM
$$\begin{bmatrix} \dot{X}(\tau_1) \\ \vdots \\ \dot{X}(\tau_N) \end{bmatrix} = [D^{GPM}] \begin{bmatrix} X(\tau_0) \\ X(\tau_1) \\ \vdots \\ X(\tau_N) \end{bmatrix} = \frac{t_f - t_0}{2} \begin{bmatrix} F\big(\tau_0, X(\tau_0), U(\tau_0)\big) \\ F\big(\tau_1, X(\tau_1), U(\tau_1)\big) \\ \vdots \\ F\big(\tau_N, X(\tau_N), U(\tau_N)\big) \end{bmatrix} \tag{4.40}$$

$$X(t_{N+1}) = X(\tau_0) + \frac{t_f - t_0}{2} [w^{GPM}] \cdot \begin{bmatrix} F\big(\tau_1, X(\tau_1), U(\tau_1)\big) \\ \vdots \\ F\big(\tau_N, X(\tau_N), U(\tau_N)\big) \end{bmatrix} \tag{4.41}$$

RPM
$$\begin{bmatrix}\dot{X}(\tau_0)\\ \dot{X}(\tau_1)\\ \vdots\\ \dot{X}(\tau_N)\end{bmatrix}=[D^{RPM}]\begin{bmatrix}X(\tau_0)\\ X(\tau_1)\\ \vdots\\ X(\tau_N)\\ X(\tau_{N+1})\end{bmatrix}=\frac{t_f-t_0}{2}\begin{bmatrix}F\big(\tau_0,X(\tau_0),U(\tau_0)\big)\\ F\big(\tau_1,X(\tau_1),U(\tau_1)\big)\\ \vdots\\ F\big(\tau_N,X(\tau_N),U(\tau_N)\big)\\ F\big(\tau_{N+1},X(\tau_{N+1}),U(\tau_{N+1})\big)\end{bmatrix} \tag{4.42}$$

GFW
$$\begin{bmatrix}\dot{X}(\tau_0)\\ \dot{X}(\tau_1)\\ \vdots\\ \dot{X}(\tau_N)\\ \dot{X}(\tau_{N+1})\end{bmatrix}=[D^{GFW}]\begin{bmatrix}X(\tau_0)\\ X(\tau_1)\\ \vdots\\ X(\tau_N)\\ X(\tau_{N+1})\end{bmatrix}=\frac{t_f-t_0}{2}\begin{bmatrix}F\big(\tau_0,X(\tau_0),U(\tau_0)\big)\\ F\big(\tau_1,X(\tau_1),U(\tau_1)\big)\\ \vdots\\ F\big(\tau_N,X(\tau_N),U(\tau_N)\big)\\ F\big(\tau_{N+1},X(\tau_{N+1}),U(\tau_{N+1})\big)\end{bmatrix} \tag{4.43}$$

Performance index function approximation:

LPM
$$J=\left(\frac{t_f-t_0}{2}\right)[w^{LPM}]\cdot\begin{bmatrix}F(\tau_0,X(\tau_0),U(\tau_0))\\ F(\tau_1,X(\tau_1),U(\tau_1))\\ \vdots\\ F(\tau_N,X(\tau_N),U(\tau_N))\\ F(\tau_{N+1},X(\tau_{N+1}),U(\tau_{N+1}))\end{bmatrix} \tag{4.44}$$

CPM
$$J=\left(\frac{t_f-t_0}{2}\right)[w^{CPM}]\cdot\begin{bmatrix}F\big(\tau_0,X(\tau_0),U(\tau_0)\big)\\ F\big(\tau_1,X(\tau_1),U(\tau_1)\big)\\ \vdots\\ F\big(\tau_N,X(\tau_N),U(\tau_N)\big)\\ F\big(\tau_{N+1},X(\tau_{N+1}),U(\tau_{N+1})\big)\end{bmatrix} \tag{4.45}$$

GPM
$$J=\left(\frac{t_f-t_0}{2}\right)[w^{GPM}]\cdot\begin{bmatrix}F\big(\tau_1,X(\tau_1),U(\tau_1)\big)\\ \vdots\\ F\big(\tau_N,X(\tau_N),U(\tau_N)\big)\end{bmatrix} \tag{4.46}$$

RPM
$$J=\left(\frac{t_f-t_0}{2}\right)[w^{RPM}]\cdot\begin{bmatrix}F(\tau_0,X(\tau_0),U(\tau_0))\\ F(\tau_1,X(\tau_1),U(\tau_1))\\ \vdots\\ F(\tau_N,X(\tau_N),U(\tau_N))\end{bmatrix} \tag{4.47}$$

GFW
$$J=\left(\frac{t_f-t_0}{2}\right)[w^{GFW}]\cdot\begin{bmatrix}F(\tau_0,X(\tau_0),U(\tau_0))\\ F(\tau_1,X(\tau_1),U(\tau_1))\\ \vdots\\ F(\tau_N,X(\tau_N),U(\tau_N))\\ F(\tau_{N+1},X(\tau_{N+1}),U(\tau_{N+1}))\end{bmatrix} \tag{4.48}$$

4.4.2 Generalization of the Legendre and Chebyshev Pseudospectral Methods

The collocation points of both the Legendre pseudospectral method and the Chebyshev pseudospectral method are defined in $[-1,1]$. These points include both end points at -1 and 1. The collocation points for the proposed framework are also defined in $[-1,1]$ and include both end points at -1 and 1. When the proposed framework is supplied with the Legendre-Gauss-Lobatto points and the Chebyshev-Gauss-Lobatto points, the proposed framework is exactly the same as both the Legendre pseudospectral method and the Chebyshev pseudospectral method.

4.4.3 Generalization of the Gauss Pseudospectral Method

The collocation points of the Gauss pseudospectral method are defined in $(-1,1)$ and do not include the end points at -1 and 1. The differential matrix is derived based on the points at -1 and the interior points, as shown in Equation (4.40). This means the states at final time are not related to the states at other times. An additional equation (Equation (4.41)) is used to ensure that the states at final time satisfy the dynamic constraint. When this additional equation is used, it is equivalent to using both the end points and the interior points to compute the differential matrix. In this way, Equation (4.40) and Equation (4.41) are equivalent to Equation (4.43) if the Legendre-Gauss points, together with the two end points, are supplied to the generalized framework, as shown in Equation (4.49).

$$\tau^{GFW} = \begin{bmatrix} \tau_0 \\ \tau^{GPM} \\ \tau_{N+1} \end{bmatrix} \tag{4.49}$$

Due to the distribution of the Legendre-Gauss points, the associated integration weights at -1 and 1 are exactly zeros, as shown in Equation (4.50). This means the

quadrature approximation of the generalized framework and that of the original Gauss pseudospectral method are the same.

$$w^{GFW} = \begin{bmatrix} 0 \\ w^{GPM} \\ 0 \end{bmatrix} \tag{4.50}$$

4.4.4 Generalization of the Radau Pseudospectral Method

The collocation points of the Radau pseudospectral method are defined in $[-1,1)$ do not include the end point at 1. The differential matrix is derived based on the LGR points and the point at 1, as shown in Equation (4.42). The LGR points, together with the point at 1, are in the same form as the collocation points used in the proposed framework, and include both the end points at -1 and 1. Equation (4.42) is equivalent to Equation (4.43) if the LGR points, together with the end point at 1, are supplied to the generalized framework, as shown in Equation (4.51).

$$\tau^{GFW} = \begin{bmatrix} \tau^{RPM} \\ \tau_{N+1} \end{bmatrix} \tag{4.51}$$

Similar to the Legendre-Gauss points, the associated quadrature weight for the collocation point of the generalized framework at 1 is exactly zero (as shown in Equation (4.52)). This means the quadrature approximation for the generalized Radau pseudospectral method and that of the original Gauss pseudospectral method are the same.

$$w^{GFW} = \begin{bmatrix} w^{GPM} \\ 0 \end{bmatrix} \tag{4.52}$$

4.4.5 Discussion on the Generalized Framework

With the proposed generalized framework, a pseudospectral method is obtained by supplying a set of collocation points defined in $[-1,1]$, where the differentiation matrix and the quadrature weights are computed numerically. Since the collocation points of the Legendre pseudospectral method and the Chebyshev pseudospectral method are also

defined in $[-1,1]$, these two methods are naturally included with the proposed framework. If the original collocation points of the Gauss and Radau pseudospectral methods, together with the end points, are supplied to the proposed framework, the resulting generalized Gauss pseudospectral method and Radau pseudospectral method are the same as the original Gauss pseudospectral method and Radau pseudospectral method, respectively. With the end points included, both the differentiation matrix and quadrature weights for integrations from the proposed framework are the same as those of the original Gauss and Radau pseudospectral methods. In this way, all four pseudospectral methods have been generalized with the proposed framework.

4.5 Comparison of Different Collocation Points with Examples

To solve the transcribed nonlinear programming problems from the proposed generalized framework, the SNOPT NLP solver from [70] is used. Since each pseudospectral method is defined by the corresponding collocation points, which can be supplied to the generalized framework for implementation, the performance of each pseudospectral method can be compared with one NLP solver. For a fair comparison, the initial guesses are kept the same for all the pseudospectral methods. The comparison is based on the ability to find the optimal solution and the NLP execution time. Besides the four sets of collocation points defined in Equations (4.13) to (4.16), a new set of collocation points, based on geometric series, is included in this comparison.

4.5.1 Geometric Collocation Points

One of the motivations for the generalized framework for pseudospectral methods is to evaluate new pseudospectral methods that use different collocation points. Similar motivation was presented in [91], which formulated pseudospectral methods on arbitrary

grids. As highlighted in [91], the collocation points of all the pseudospectral methods share the common property of dense distribution around the end points. In this section, a new set of collocation points, named Geometric Collocation (GC) points, is defined as shown in Figure 4.6 and Figure 4.7. The distance between two consecutive collocation points decreases at a rate of k. In this way, more points are distributed around the end points.

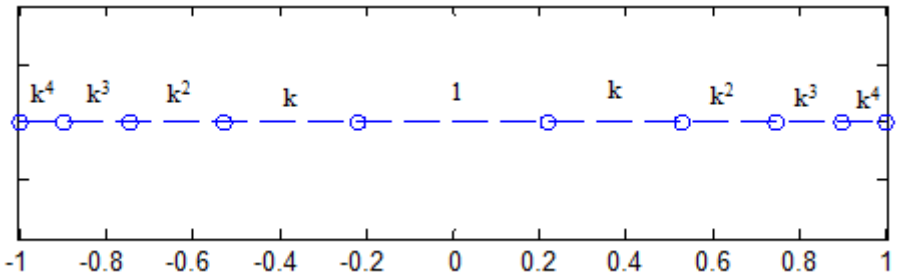

Figure 4.6 Definition for the Geometric Collocation points (N = Even)

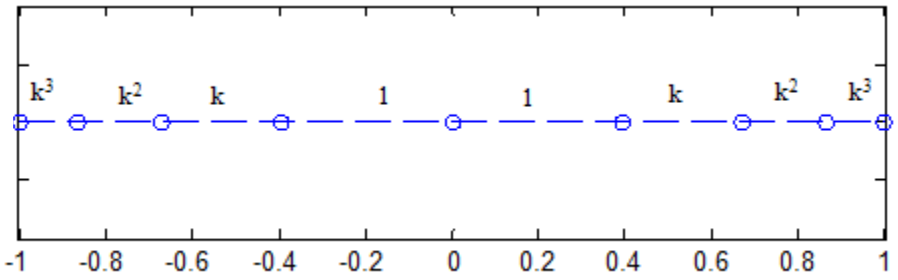

Figure 4.7 Definition for the Geometric Collocation points (N = Odd)

4.5.2 Example 1: Brachistochrone Problem

Consider the following optimal control problem, the Brachistochrone problem, originally formulated by Johann Bernoulli in 1696 [98].

Minimize the cost function

$$J = t_f \tag{4.53}$$

subject to dynamic constraints

$$\begin{cases} \dot{x} = v\,sin(\theta) \\ \dot{y} = v\,cos(\theta) \\ \dot{v} = g\,cos(\theta) \end{cases} \tag{4.54}$$

and boundary conditions

$$\begin{cases} x(0) = 0 \quad y(0) = 0 \quad v(0) = 0 \\ \qquad x(t_f) = 2 \quad y(t_f) = 2 \end{cases} \tag{4.55}$$

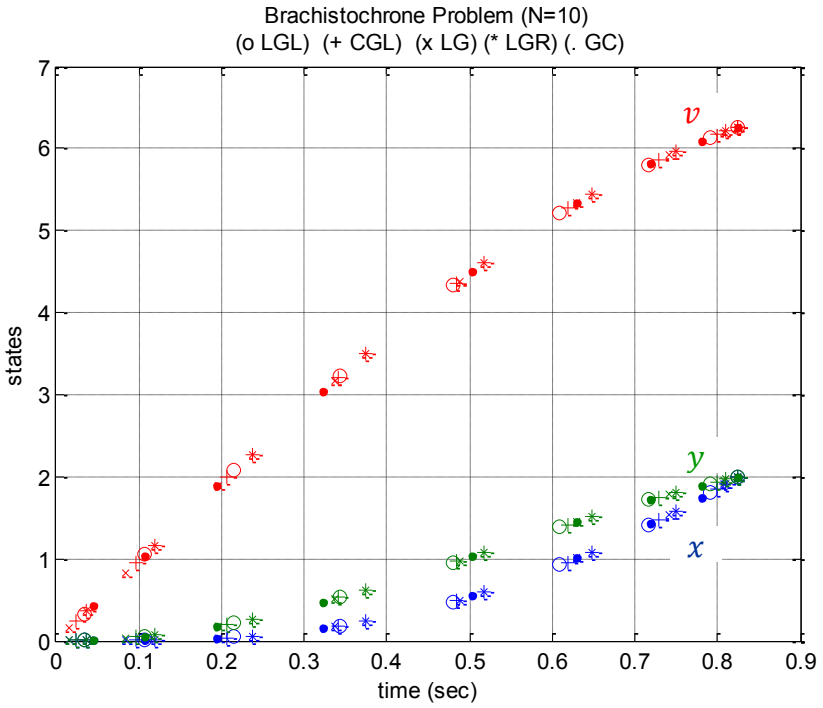

Figure 4.8 Optimal state trajectories for the Brachistochrone problem.

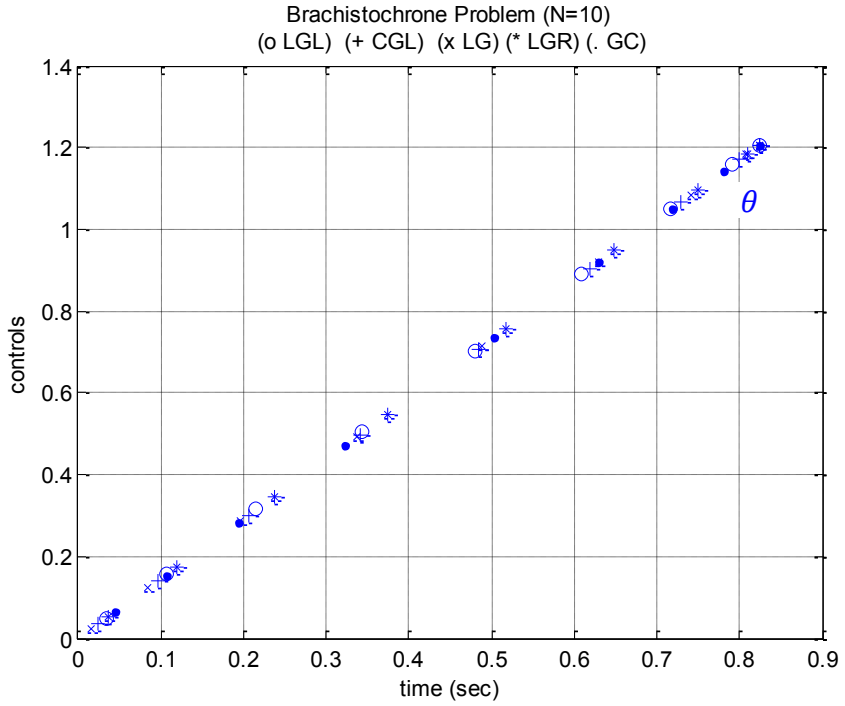

Figure 4.9 Optimal control trajectories for the Brachistochrone problem.

Table 4.1 NLP execution time for the Brachistochrone problem.

Collocation Points	NLP Execution Time (second)
LGL	0.5304
CGL	0.7304
LG	0.6311
LGR	0.9518
GC ($k = 0.7$)	0.5928

Figure 4.8 and Figure 4.9 show the optimal state and control trajectories from the generalized framework with different sets of collocation points for the Brachistochrone problem, and Table 4.1 shows the corresponding NLP execution time. All the pseudospectral methods defined by the five sets collocation points are able to converge to the optimal solution. The NLP execution time of the LGL points is the shortest and that of the LGR points is the longest.

4.5.3 Example 2: Trajectory Optimization for a Dubins Airplane

The three-dimensional Dubins airplane model [99] is often used to study the optimal trajectories for UAVs. A minimum distance point-to-point trajectory optimization problem for a given initial configuration and final configuration is shown as follows:

Minimize the cost function

$$J = \int_{t_0}^{t_f} V \, dt \tag{4.56}$$

subject to dynamic constraints

$$\begin{cases} \dot{x} = V \cos\gamma \cos\psi \\ \dot{y} = V \cos\gamma \sin\psi \\ \dot{z} = V \sin\gamma \\ \dot{\psi} = u_1 \\ \dot{\gamma} = u_2 \end{cases} \tag{4.57}$$

and boundary conditions

$$\begin{cases} t_0 = 0, t_f = free \\ \{x(t_0), y(t_0), z(t_0)\} = \{0,0,0\} \\ \{x(tf), y(tf), z(tf)\} = \{212,212,30\} \\ \psi(t_0) = 0, \psi(t_f) = 0 \\ \gamma(t_0) = 0, \gamma(t_f) = 0 \end{cases} \tag{4.58}$$

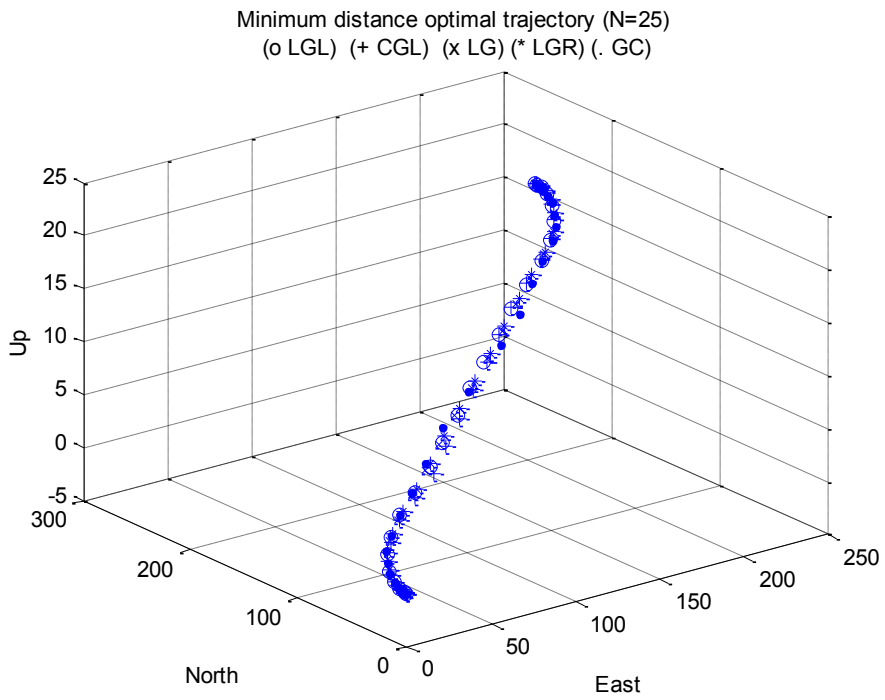

Figure 4.10 Optimal trajectories of the example trajectory optimization problem.

Table 4.2 NLP Execution time of the example trajectory optimization problem.

Collocation Points	NLP Execution Time (second)
LGL	8.51
CGL	8.68
LG	1.71
LGR	1.28
GC ($k = 0.83$)	8.60

Figure 4.10 shows the optimal trajectories from different pseudospectral methods for the example minimum distance trajectory optimization problem, and the corresponding NLP execution time is shown in Table 4.2. All the methods are able to converge to the optimal solution. The NLP execution time of the pseudospectral methods defined by the LG and LGR points is significantly shorter than that of the methods defined by the LGL, CGL, and GC points.

Through examples, the proposed generalized framework provides an easy tool for comparing the performance of different pseudospectral methods. In general, a problem that can be solved by one pseudospectral method can also be solved by another pseudospectral method. However, the NLP execution time for the same problem is usually different depending on the pseudospectral method that is used. An efficient method for one problem may not be efficient for another problem.

4.6 Summary

This chapter proposed a generalized framework for pseudospectral methods to transcribe an optimal control problem as a nonlinear programming (NLP) optimization problem, where only the collocation points were required to define a pseudospectral method. The four pseudospectral methods, namely the Legendre pseudospectral method, the Chebyshev pseudospectral method, the Gauss pseudospectral method, and the Radau pseudospectral method were implemented by supplying the corresponding collocation points to the proposed framework, and the differentiation matrix and quadrature weights for integration were computed automatically for all four methods. With the proposed framework, different pseudospectral methods were compared with the same NLP solver through examples.

CHAPTER 5

TRAJECTORY OPTIMIZATION FOR A FUEL CELL POWERED UAV

5.1 Introduction

This chapter attempts to demonstrate an understanding of the influence of a fuel cell system on the optimal trajectories of a fuel cell powered UAV by formulating the trajectory optimization problems for a fuel cell powered UAV as optimal control problems, where the dynamic equations of a fuel cell powered UAV propulsion system are included as part of the dynamic constraints. The generalized framework for pseudospectral methods presented in the previous chapter is used to transcribe the optimal control problems to nonlinear programming (NLP) problems, which are then solved by using the SNOPT solver [70]. In this chapter, the optimal trajectories of the fuel cell powered configuration and that of the conventional gas powered configuration are compared for point-to-point optimal trajectories with different performance index functions. Among different trajectory optimization problems, the most significant differences are those between the minimum fuel point-to-point optimal trajectories of the fuel cell powered configuration and that of the conventional gas powered configuration. Due to the specific fuel consumption curve of the fuel cell powered configuration, there is an optimal flight path angle when the height difference between the initial position and the final position is significant.

The influence of the fuel cell system model parameters on the minimum fuel point-to-point optimal trajectories is studied here through their influence on the optimal

fuel consumption cost. The influence of the transient parameters (the fuel cell capacitance (C) and the fuel cell delay gain constant (λ_e)) on the optimal fuel consumption cost is insignificant, and the influence of the fuel cell delay time constant (τ_e) is only slightly more significant. These transient parameters are caused by design parameters at the membrane level of the fuel cell system. However, the influence of the fuel cell system size parameters (the number of cells (N) and the cell area (A)) on the optimal fuel consumption cost is significant. This is because the efficiency of a fuel cell system increases as its size increases.

5.2 Trajectory Optimization Problem Formulation

One of the most essential steps in formulating a trajectory optimization problem is the derivation of the dynamic constraint equations. In this section, the dynamic constraint equations for a trajectory optimization problem are obtained by combining the dynamic model of a fuel cell powered UAV propulsion system and the dynamic equations of a point mass UAV model.

The UAV dynamic behavior at the trajectory level can be approximated by a three-dimensional point mass model and the corresponding assumptions are summarized as follows:

- The earth is assumed to be flat.
- The UAV performs coordinated turns.
- The bank angle and the angle of attack of the UAV can be changed instantaneously.
- The lift and drag of the UAV changes instantaneously with respect to the angle of attack.

- The mass of the UAV is assumed to be constant during the time interval of the trajectory optimization problems, as the fuel weight is very small relative to the gross weight of a fuel cell powered UAV.

Figure 5.1 shows the forces in a UAV point mass model are shown in where the UAV is flying at a flight path angle of γ with an air speed of V. The kinematic equations for the three-dimensional point mass model are Equations (5.1) to (5.6). Equations (5.7) to (5.11) are the dynamic equations of a fuel cell powered UAV propulsion system. The link between the UAV states and the propulsion system states is the propeller rotational speed. The complete set of equations, Equations (5.1) to (5.11), is the dynamic constraint equations when formulating the trajectory optimization problems for a fuel cell powered UAV. This set includes both the UAV dynamics and the fuel cell powered propulsion system dynamics.

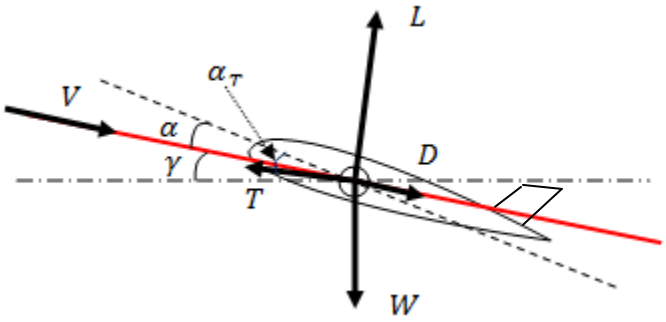

Figure 5.1 Forces in a UAV point mass model.

$$\dot{x} = V \cos\gamma \cos\psi \tag{5.1}$$

$$\dot{y} = V \cos\gamma \sin\psi \tag{5.2}$$

$$\dot{z} = V \sin\gamma \tag{5.3}$$

$$\dot{V} = \frac{T(V,\Omega)\cos(\alpha - \alpha_T) - D}{M} - g \sin\gamma \tag{5.4}$$

$$\dot{\psi} = \frac{(L + T\,sin(\alpha - \alpha_T))\,sin\,\phi}{M\,V\,cos\,\gamma} \tag{5.5}$$

$$\dot{\gamma} = \frac{(L + T\,sin(\alpha - \alpha_T))\,cos\,\phi}{M\,V} - \frac{g}{V}cos\,\gamma \tag{5.6}$$

$$\dot{V_c} = -\frac{1}{(R_{act} + R_{con})C}V_c + \frac{I_{cell}}{C} \tag{5.7}$$

$$\dot{E_d} = -\frac{1}{\tau_e}E_d(t) + \lambda_e \dot{I}_{cell} \tag{5.8}$$

$$\dot{I_m} = \frac{1}{L_m}(V_{in} - I_m\,R_m - V_m) \tag{5.9}$$

$$\dot{\Omega} = \frac{Q_m - Q_p}{J} \tag{5.10}$$

where x, y, z are the UAV positions in inertial axis, V is the air speed, ψ is the heading angle, γ is the flight path angle, Ω is the propeller rotational speed, V_c is the fuel cell capacitance voltage, E_d is the fuel cell voltage drop due to the fuel cell delay, and I_m is the electric motor current. The other parameters were explained in Chapter 4.

In addition to the dynamic constraint equations, the performance index function and the terminal constraints are required to formulate a trajectory optimization problem. The performance index function is determined by the mission requirements. Examples of the performance index functions are total flight time, total fuel consumption, time average fuel consumption, and total flight distance. The UAV states at the initial time and final time are determined by the terminal constraints. The objective of a trajectory optimization problem is to minimize the performance index function, subject to the dynamic constraints, terminal constraints, and path constraints (if applicable).

5.3 Optimal Trajectory Comparisons

As compared to a conventional gas powered UAV, a fuel cell powered UAV has two unique aspects: the transient response delay and the specific fuel consumption curve. The

study of the transient characteristics of a fuel cell powered UAV propulsion system discussed in Chapter 2 has indicated that response delays at the UAV level can be expected due to the delay in the fuel cell system. In the performance comparison of a fuel cell powered configuration and a conventional gas powered configuration presented in Chapter 3, it can be observed the trend of the specific fuel consumption curve of the fuel cell powered configuration is significantly different from that of the conventional gas powered configuration. In this section, the influence of these two aspects is then studied by comparing the optimal trajectories of the fuel cell powered configuration and that of a conventional gas powered configuration of different trajectory optimization problems with different performance index functions.

5.3.1 Model Comparison

The dynamic constraints of the fuel cell powered configuration and that of the conventional gas powered configuration are compared in Table 5.1. The UAV dynamic equations for UAV states $(x, y, z, V, \psi, \gamma)$ are identical for both configurations. The differences in the propulsion systems are reflected by the differences in computing the driving torque. In the fuel cell powered configuration, the driving torque is provided by an electric motor, whose dynamics are coupled with the fuel cell system's dynamics, as discussed in Chapter 4. The driving torque of the conventional gas powered configuration, on the other hand, is provided by a reciprocating engine, and the power available from the reciprocating engine (P_{in}) is modeled as the input parameter.

Table 5.1 Model comparison between the fuel cell powered configuration and the conventional gas powered configuration.

Fuel Cell Powered Configuration	Gas Powered Configuration
$\dot{x} = V\cos\gamma\cos\psi$ $\dot{y} = V\cos\gamma\sin\psi$ $\dot{z} = V\sin\gamma$ $\dot{V} = \frac{T(V,\Omega)\cos(\alpha-\alpha_T) - D}{M} - g\sin\gamma$ $\dot{\psi} = \frac{(L + T\sin(\alpha-\alpha_T))\sin\phi}{M\,V\cos\gamma}$ $\dot{\gamma} = \frac{(L + T\sin(\alpha-\alpha_T))\cos\phi}{M\,V} - \frac{g}{V}\cos\gamma$ $\dot{\Omega} = \frac{Q_m - Q_p}{J}$ $\dot{V}_c = -\frac{1}{(R_{act}+R_{con})C}V_c + \frac{I_{cell}}{C}$ $\dot{E}_d = -\frac{1}{\tau_e}E_d(t) + \lambda_e\dot{I}_{cell}$ $\dot{I}_m = \frac{1}{L_m}(V_{in} - I_m\,R_m - V_m)$	$\dot{x} = V\cos\gamma\cos\psi$ $\dot{y} = V\cos\gamma\sin\psi$ $\dot{z} = V\sin\gamma$ $\dot{V} = \frac{T(V,\Omega)\cos(\alpha-\alpha_T) - D}{M} - g\sin\gamma$ $\dot{\psi} = \frac{(L + T\sin(\alpha-\alpha_T))\sin\phi}{M\,V\cos\gamma}$ $\dot{\gamma} = \frac{(L + T\sin(\alpha-\alpha_T))\cos\phi}{M\,V} - \frac{g}{V}\cos\gamma$ $\dot{\Omega} = \frac{P_{in}/\Omega - Q_p}{J}$

5.3.2 Minimum Fuel Point-to-point Optimal Trajectory Comparison

One of the most commonly studied trajectories is the point-to-point minimum fuel trajectory, where a UAV flies from point A to point B with minimum fuel consumption. In this problem, the UAV states $(x, y, z, V, \psi, \gamma)$ at the initial time and the final time are known. The states associated with the fuel cell propulsion system, $\Omega(t_0), V_c(t_0), E_d(t_0), I_m(t_0)$ and $\Omega(t_f), V_c(t_f), E_d(t_f), I_m(t_f)$ are determined from the rate terminal constraints, where the time derivatives of these variables are zeros at the initial time and the final time. In addition, $\dot{V}(t_0), \dot{\psi}(t_0), \dot{\gamma}(t_0)$ and $\dot{V}(t_f), \dot{\psi}(t_f), \dot{\gamma}(t_f)$ are zeros to ensure that the UAV starts from a steady-state flight condition and finishes at a steady-state flight condition.

To minimize the fuel consumption, the performance index function is defined as the total fuel consumption from the initial time to the final time. The differences in the specific fuel consumption curve of the fuel cell powered configuration and that of the conventional gas powered configuration are illustrated in Figure 3.8 and Figure 3.10. The performance index function and the terminal constraints are summarized as follows:

Minimize:

$$J = \int_{t_0}^{t_f} \dot{m}_{fuel}\, dt \tag{5.11}$$

Terminal Conditions:

$$\begin{cases} t_0 = 0\ sec \\ \{x(t_0), y(t_0), z(t_0)\} = \{x_0, y_0, z_0\} \\ V(t_0) = 20\, m/s \\ \psi(t_0) = \psi_0 \\ \gamma(t_0) = 0 \\ \{\Omega(t_0), V_c(t_0), E_d(t_0), I_m(t_0)\} = free \\ \{\dot{V}(t_0), \dot{\psi}(t_0), \dot{\gamma}(t_0)\} = 0 \\ \{\dot{\Omega}(t_0), \dot{V}_c(t_0), \dot{E}_d(t_0), \dot{I}_m(t_0)\} = 0 \end{cases} \tag{5.12}$$

$$\begin{cases} t_f = free \\ \{x(t_f), y(t_f), z(t_f)\} = \{x_f, y_f, z_f\} \\ V(t_f) = 20\, m/s \\ \psi(t_f) = \psi_f \\ \gamma(t_f) = 0 \\ \{\dot{V}(t_f), \dot{\psi}(t_f), \dot{\gamma}(t_f)\} = 0 \\ \{\dot{\Omega}(t_f), \dot{V}_c(t_f), \dot{E}_d(t_f), \dot{I}_m(t_f)\} = 0 \end{cases} \tag{5.13}$$

Height variations are included between the initial positions and the final positions to demonstrate the influence of the specific consumption rate on the flight trajectory. Figure 5.2 shows the point-to-point minimum fuel optimal trajectories at different height variations for the fuel cell configuration. Only when the height variations are small are the optimal trajectories similar to a straight line flight path. In this dissertation, a straight

line flight path is defined as the flight path that directly connects the initial position and the final position. When the height variation is increased, more power is required to fly at a straight line flight path. As shown in Figure 3.10, the specific fuel consumption rate of the fuel cell system increases significantly in high power regions. This indicates that the minimum fuel optimal trajectory needs to avoid high power regions. Hence, the optimal trajectories are similar to S-shaped flight paths, where lower power is required as compared to the straight line flight paths, which require more power.

Figure 5.3 shows the point-to-point minimum fuel optimal trajectories at different height variations for the conventional gas powered configuration. For most values of the height variations, the optimal trajectories are similar to straight line flight paths. Only when the power requirement of the straight line flight path is more than the capacity of the reciprocating engine do the optimal trajectories are S-shaped flight paths. This can be explained by the specific fuel consumption curve of the reciprocating engine (Figure 3.8). The specific fuel consumption rate is almost constant when the reciprocating engine is running at a power of more than 400W. However, no fuel consumption penalty is experienced for straight line flight paths.

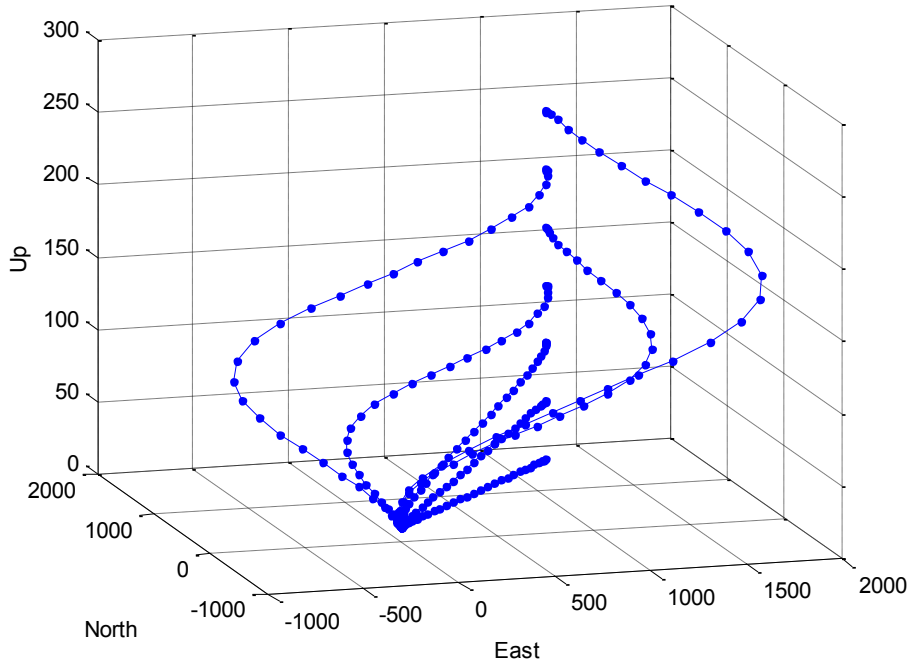

Figure 5.2 Minimum fuel point-to-point optimal trajectories (fuel cell powered configuration).

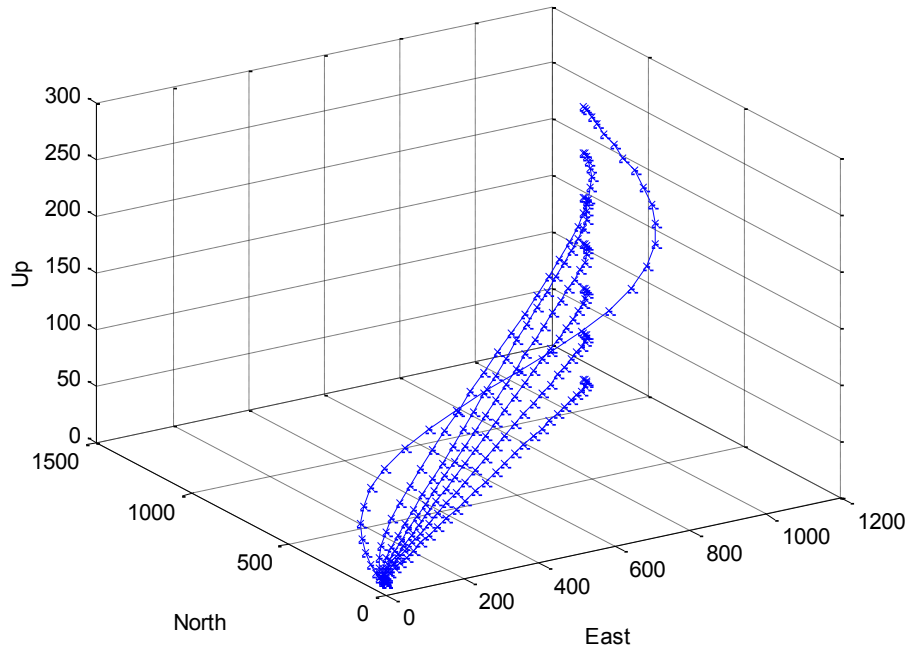

Figure 5.3 Minimum fuel point-to-point optimal trajectories (conventional gas powered configuration).

The optimal fight path angle with respect to the straight line flight path slope for the fuel cell powered configuration is shown in Figure 5.4. The optimal fight path angle for the conventional gas powered configuration increases linearly with the straight line slope until the maximum available power from the reciprocating engine is reached. For the fuel cell powered configuration, the optimal flight path angle increases linearly with the straight line slope until 3.7 degrees. When the straight line slope is more than 3.7 degrees, the UAV needs to climb using S-shaped flight paths to minimize fuel consumption. The fuel consumption in a steady state ascend flight condition can be approximated by Equation (5.14). For a given ΔH, the function $\frac{\dot{m}_{fuel}}{V \sin\gamma}$ determines the minimum fuel optimal flight path angle. Figure 5.5 shows the variation of the function $\frac{\dot{m}_{fuel}}{V \sin\gamma}$ with respect to the flight path angle. When the straight line slope is less than 3.7 degrees, the minimum fuel flight path angle is the straight line slope. When the straight line slope is more than 3.7 degrees, the minimum fuel flight path angle is at 3.7 degrees. This is the reason for the minimum fuel point-to-point optimal trajectories to show S-shaped patterns when the height differences between the initial positions and the final positions are significant.

$$m_{fuel} = \dot{m}_{fuel} \frac{\Delta H}{V \sin\gamma} = \left(\frac{\dot{m}_{fuel}}{V \sin\gamma}\right) \Delta H \tag{5.14}$$

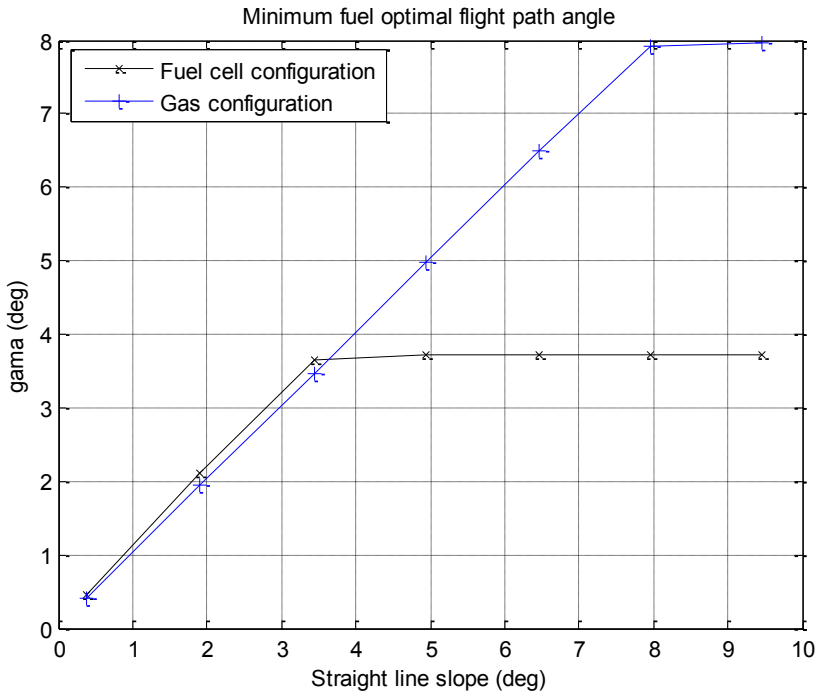

Figure 5.4 Optimal flight path angles at different height variations.

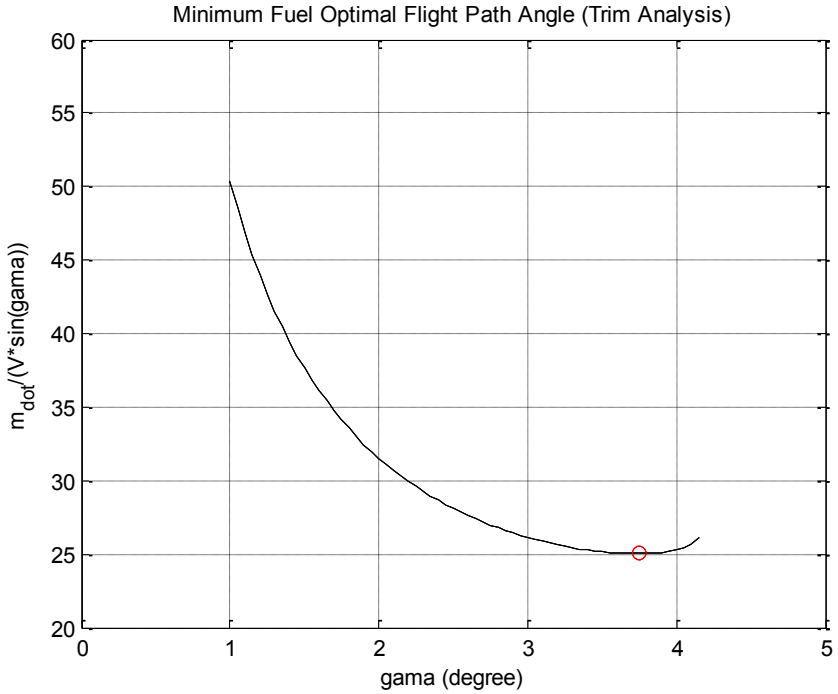

Figure 5.5 Steady state fuel consumption characteristics of the fuel cell powered configuration at different flight path angles.

5.3.3 Minimum Time Point-to-point Optimal Trajectory Comparison

Another commonly used performance index function for point-to-point trajectories is the final time. Figure 5.6 and Figure 5.7 show the minimum time point-to-point optimal trajectories for the fuel cell powered configuration and the conventional gas powered configuration, respectively. The optimal flight trajectories of both configurations are constrained by the maximum power available from their propulsion systems. Since the maximum available power of the fuel cell system is much lower than that of the reciprocating engine, the fuel cell powered configuration needs to use the S-shaped flight paths to reach the final position at much lower flight path angles.

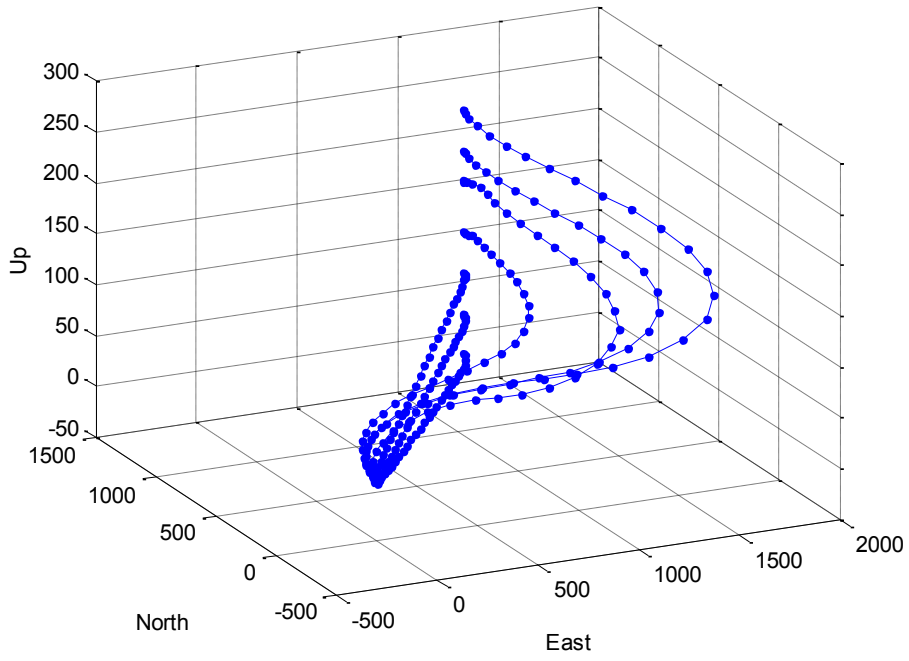

Figure 5.6 Minimum time point-to-point optimal trajectories (fuel cell powered configuration).

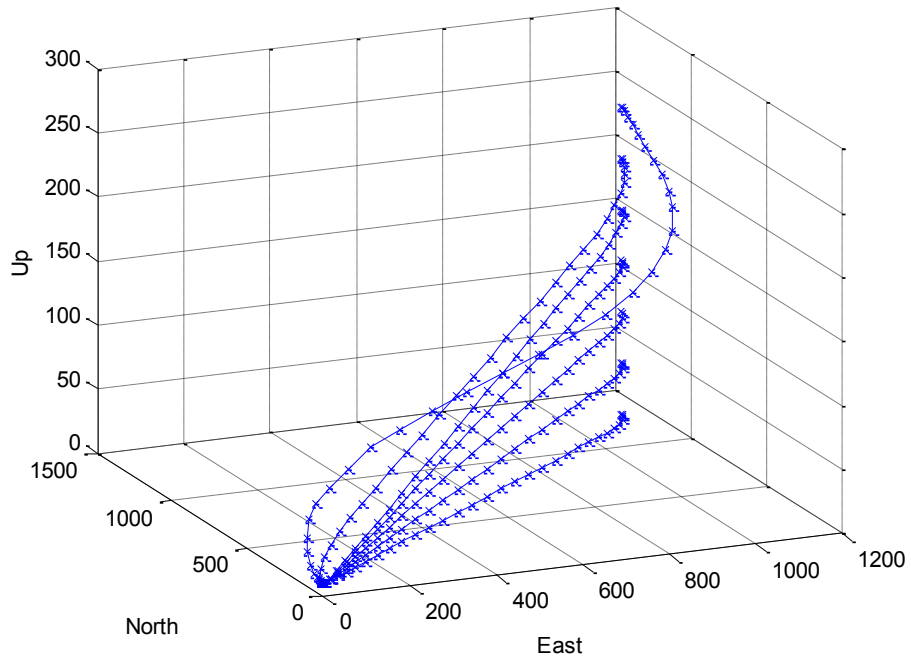

Figure 5.7 Minimum time point-to-point optimal trajectories (conventional gas powered configuration).

5.3.4 Minimum Distance Point-to-point Optimal Trajectory Comparison

Minimum distance point-to-point trajectory optimization problems are also commonly studied. If the flight speed of the UAV is fixed, the minimum distance optimal trajectories are the same as the minimum time optimal trajectories. Figure 5.8 and Figure 5.9 show the minimum distance point-to-point optimal trajectories for the fuel cell powered configuration and the conventional gas powered configuration, respectively. Similar to the minimum time optimal trajectories, the minimum distance optimal flight trajectories of both configurations are constrained by the maximum power available from their propulsion systems. The optimal fight path angle is the straight line slope until maximum powered is reached, and the speed is determined by the spare power.

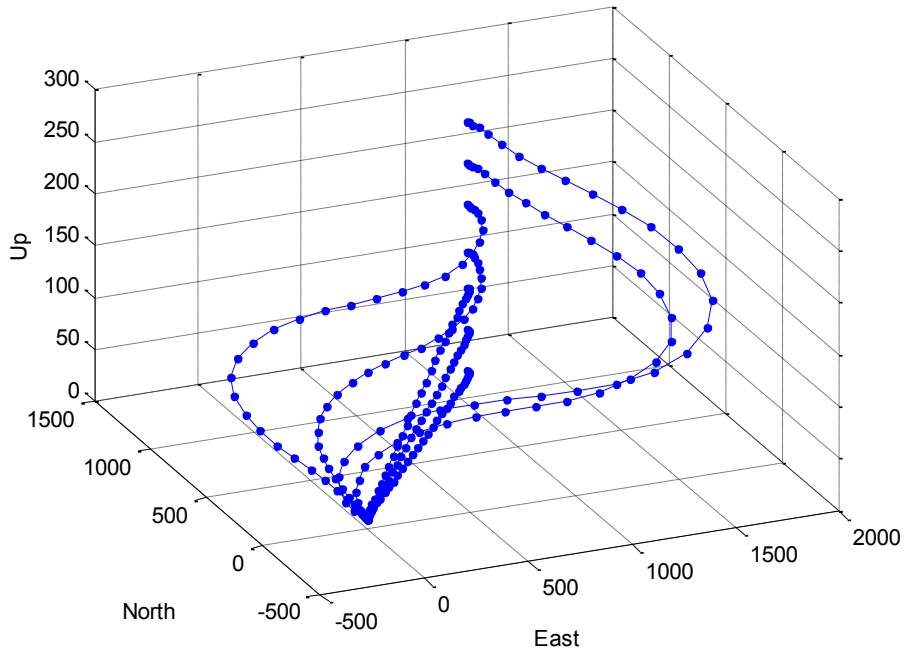

Figure 5.8 Minimum distance point-to-point optimal trajectories (fuel cell powered configuration).

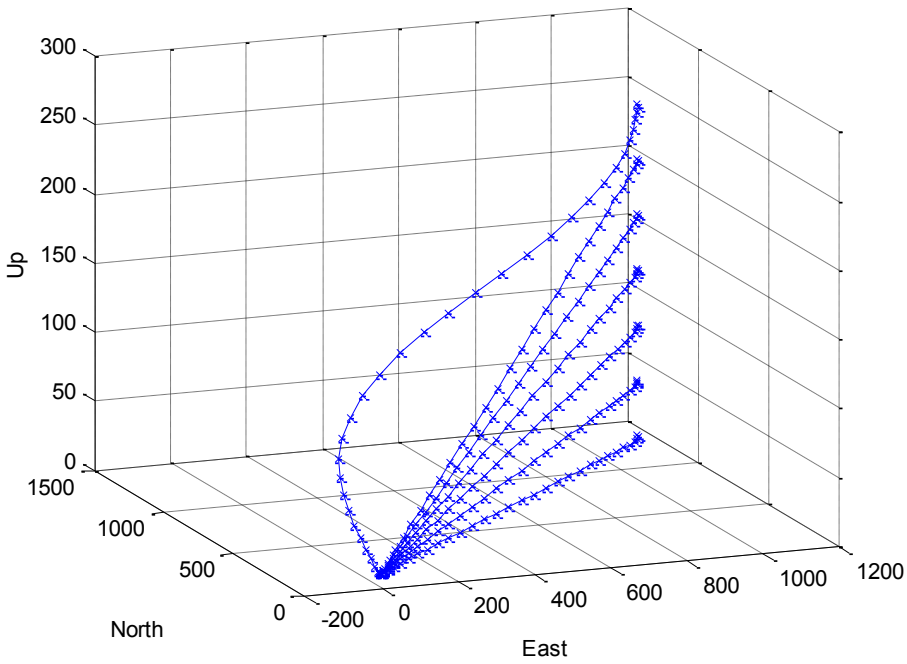

Figure 5.9 Minimum distance point-to-point optimal trajectories (conventional gas powered configuration).

5.3.5 Discussion on Point-to-point Optimal Trajectories

As point-to-point optimal trajectories are often used for flight path planning for UAVs, the differences in the optimal trajectories of different performance index functions for each configuration are discussed in this section. Figure 5.10 shows the optimal flight path angles for the point-to-point flight trajectories of the conventional gas powered configuration with different performance index functions at different straight line slopes. As highlighted in the previous section, for all three performance index functions, the optimal flight path angle is the straight line slope until the maximum power is reached. The differences due to the different performance index functions are the flight speeds associated with the optimal trajectories. As shown in Figure 5.11, the optimal flight speed for the minimum time optimal trajectories and that of the minimum distance trajectories are similar, since both are determined by the spare power available from the propulsion system. The optimal flight speeds for the minimum fuel optimal trajectories, on the other hand, are determined by the specific fuel consumption curve.

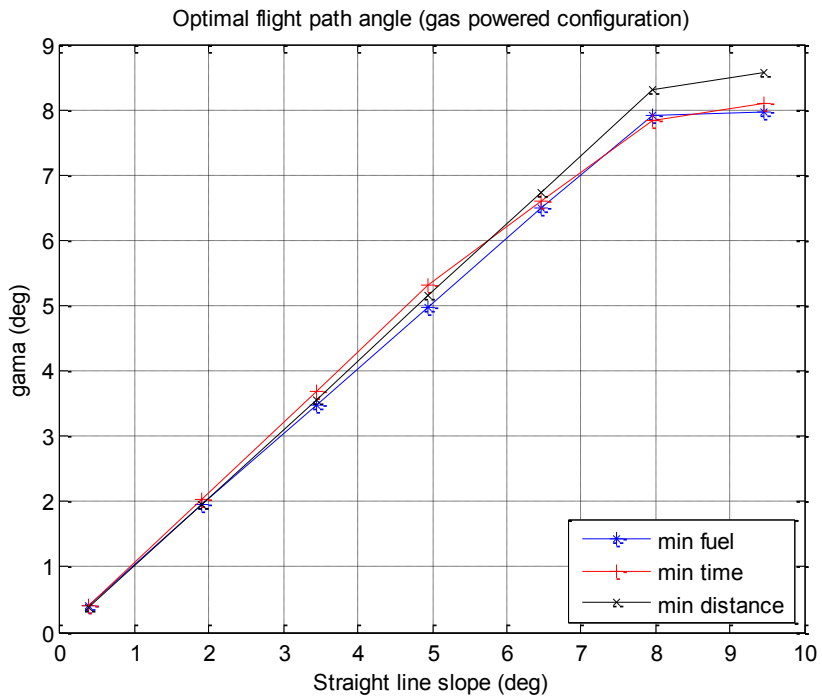

Figure 5.10 Optimal flight path angles for the point-to-point flight trajectories with different performance index functions (conventional gas powered configuration).

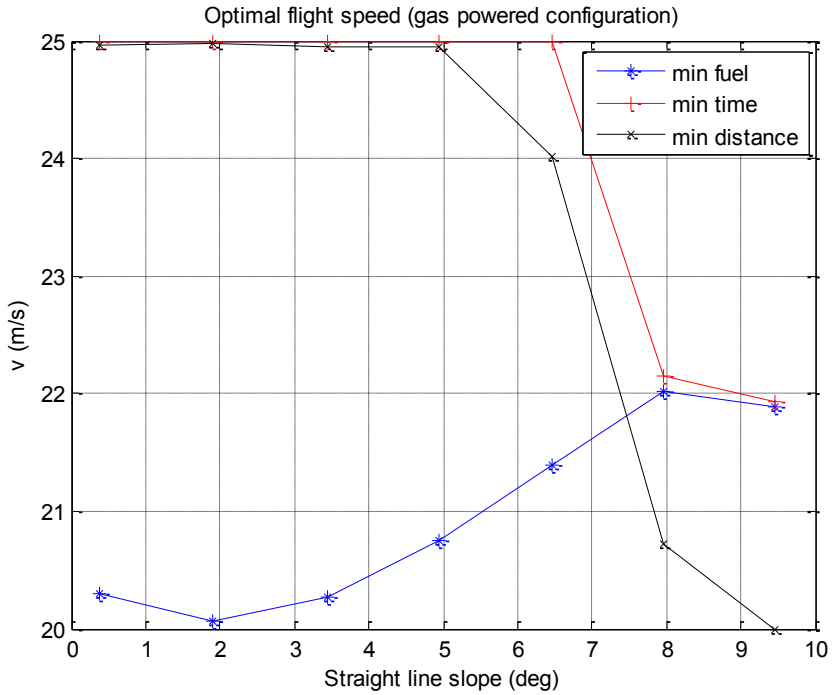

Figure 5.11 Optimal flight speeds for the point-to-point flight trajectories with different performance index functions (conventional gas powered configuration).

The optimal flight path angles of the point-to-point optimal trajectories of the fuel cell powered configuration with different performance index functions at different straight line slopes are shown in Figure 5.12, and the optimal flight speeds are shown in Figure 5.13. The optimal flight path angles of the minimum fuel optimal trajectories are lower than that of the minimum time and minimum distance optimal trajectories. This is due to the specific fuel consumption curve of a fuel cell system, which increases drastically with respect to the operating power when the fuel cell system operates in the region around the maximum power. For the same reason, the optimal fight speeds of minimum fuel optimal trajectories are always the minimum allowable speed, and the optimal flight speeds of both minimum time and minimum distance optimal trajectories are determined by the available spare power.

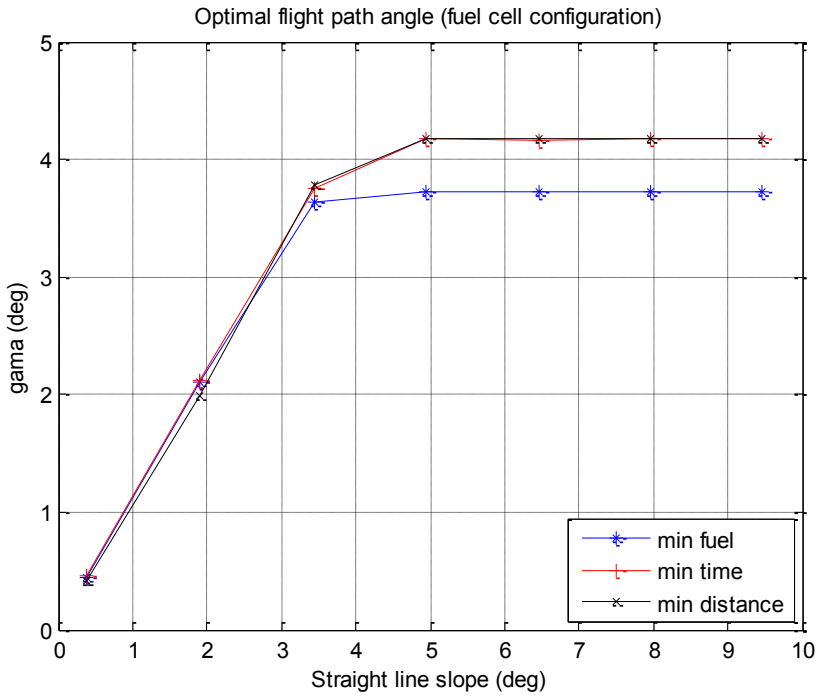

Figure 5.12 Optimal flight path angles for the point-to-point flight trajectories with different performance index functions (fuel cell powered configuration).

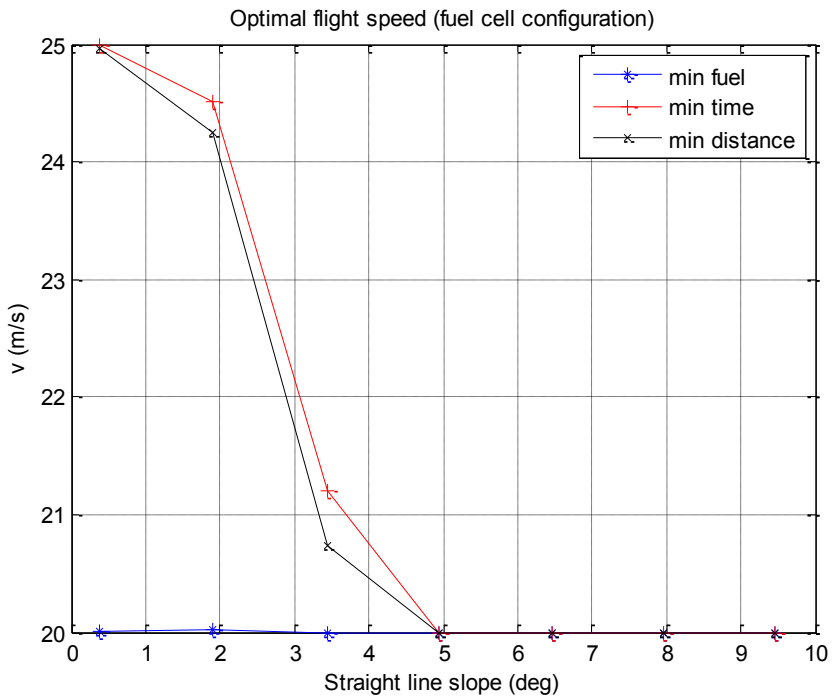

Figure 5.13 Optimal flight speeds for the point-to-point flight trajectories with different performance index functions (fuel cell powered configuration).

The flight trajectories of a UAV are often approximated with Dubins curves, where only geometric constraints are used to model the UAV dynamics and the flight speed is fixed. When the flight speed is fixed, minimum distance and minimum time optimal trajectories are the same. For a conventional gas powered configuration, the point-to-point optimal trajectories of all three performance index functions are similar in the flight path angles. The flight paths generated based on a Dubins vehicle or a Dubins airplane provide a good approximation for all three purposes. However, for the fuel cell powered configuration, the optimal flight path angles of the minimum fuel point-to-point optimal trajectories are significantly different from those of the minimum time and minimum distance optimal trajectories. The flight paths generated based on a Dubins vehicle or a Dubins airplane fails to consider the fuel consumption characteristics of a fuel cell system.

5.4 Influence of Fuel Cell System Parameters on Optimal Trajectories

The previous section demonstrated that the minimum fuel point-to-point optimal trajectories of a fuel cell powered UAV are significantly different from those of a conventional gas powered UAV. Both the steady state performance and the transient performance of a fuel cell system are reflected in the minimum fuel point-to-point optimal trajectories. In this section, the influence of fuel cell system model parameters on the minimum fuel point-to-point optimal trajectories is studied. These parameters are the fuel cell capacitance (C), the fuel cell delay time constant (τ_e), the fuel cell delay gain constant (λ_e), the number of cells (N) of the fuel cell system, and the cell area (A) of the fuel cell system. Since the optimal trajectories are different for problems with different height variations, trajectory optimization problems with two height variations are used to study the influence of the model parameters on the total fuel consumption cost. The optimal trajectories of these two cases with nominal parameters are shown in Figure 5.14 and Figure 5.15.

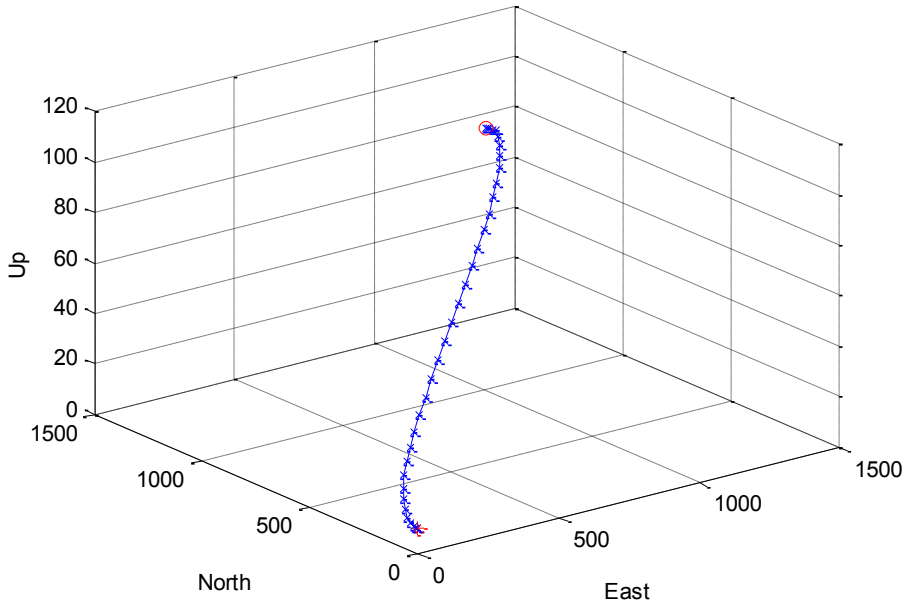

Figure 5.14 Optimal trajectories for nominal parameters at $\gamma = 3.4^{o}$.

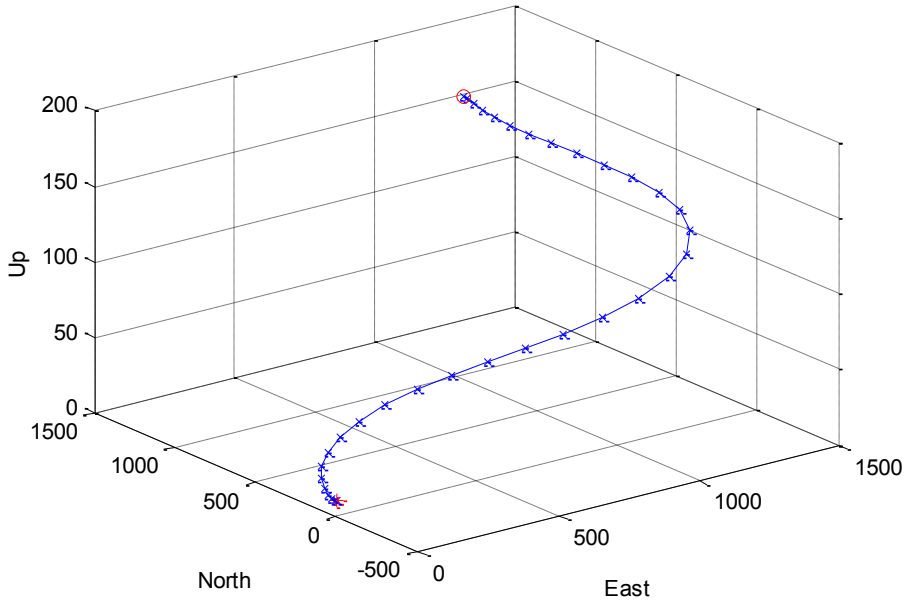

Figure 5.15 Optimal trajectories for nominal parameters at $\gamma = 6.5^{o}$.

The influence of model parameters on the fuel consumption cost associated with the minimum fuel point-to-point optimal trajectories is investigated by varying the model parameters from 20% to 500% of the nominal values. The nominal values are shown in Table 2.1. The variation on the total fuel consumption cost with respect to the variations

in the model parameters at different flight path angles is shown in Table 5.2 to Table 5.6. For all cases, the influence of all the parameters on the total fuel consumption cost is more significant at a higher flight path angle. Among the five model parameters, the influence of the fuel cell capacitance (C) and the fuel cell delay gain constant (λ_e) is insignificant. The influence of the fuel cell delay constant (τ_e) is significant when its magnitude is more than 10 seconds, which is 500% of the nominal value. The fuel cell delay effect, which is the delay between the change between the load current and the flow of fuel and oxidant in the fuel cell system, is caused by the transportation process for the molecular species across the fuel cell membrane. This parameter is influenced by the physical design of each cell of a fuel cell system. The influence of the size of the fuel cell system, the number of cells (N) and the cell area (A), is within 10% of the baseline values. As the size of the fuel cell system increases, either by increasing the number of cells (N) or by increasing the cell area (A), the efficiency of the fuel cell system improves. High efficiency leads to lower total fuel consumption cost, which is illustrated in the results shown in Table 5.5 and Table 5.6.

Table 5.2 Effect of the fuel cell capacitance (C) on the fuel cost of the minimum fuel optimal trajectories.

	$\gamma = 3.4^o$		$\gamma = 6.5^o$	
$\frac{C}{C_{ref}}$	Fuel Consumption (gram)	Difference (%)	Fuel Consumption (gram)	Difference (%)
0.2	0.6222	-0.05%	1.1477	-0.07%
0.5	0.6225	0.01%	1.1481	-0.03%
1.0	0.6225	0.00%	1.1485	0.00%
2.0	0.6246	0.34%	1.1536	0.44%
5.0	0.6257	0.52%	1.1608	1.07%

Table 5.3 Effect of the fuel cell delay time constant (τ_e) on the fuel cost of the minimum fuel optimal trajectories.

	$\gamma = 3.4^o$		$\gamma = 6.5^o$	
$\frac{\tau_e}{\tau_{e,ref}}$	Fuel Consumption (gram)	Difference (%)	Fuel Consumption (gram)	Difference (%)
0.2	0.6149	-1.22%	1.1331	-1.34%
0.5	0.6177	-0.76%	1.1401	-0.73%
1.0	0.6225	0.00%	1.1485	0.00%
2.0	0.6340	1.86%	1.1637	1.32%
5.0	0.6808	9.38%	1.2119	5.52%

Table 5.4 Effect of the fuel cell delay gain constant (λ_e) on the fuel cost of the minimum fuel optimal trajectories

	$\gamma = 3.4^o$		$\gamma = 6.5^o$	
$\frac{\lambda_e}{\lambda_{e,ref}}$	Fuel Consumption (gram)	Difference (%)	Fuel Consumption (gram)	Difference (%)
0.2	0.6222	-0.05%	1.1495	0.09%
0.5	0.6223	-0.03%	1.1505	0.18%
1.0	0.6225	0.00%	1.1485	0.00%
2.0	0.6228	0.06%	1.1492	0.06%
5.0	0.6242	0.28%	1.1521	0.31%

Table 5.5 Effect of the number of cells (N) on the fuel cost of the minimum fuel optimal trajectories

	$\gamma = 3.4^o$		$\gamma = 6.5^o$	
N	Fuel Consumption (gram)	Difference (%)	Fuel Consumption (gram)	Difference (%)
44	0.6383	2.55%	1.1898	3.60%
46	0.6286	0.98%	1.1874	3.39%
48	0.6225	0.00%	1.1485	0.00%
50	0.6187	-0.61%	1.1336	-1.29%
52	0.6164	-0.97%	1.1217	-2.33%

Table 5.6 Effect of the cell area (A) on the fuel cost of the minimum fuel optimal trajectories

	$\gamma = 3.4^{o}$		$\gamma = 6.5^{o}$	
A (cm^2)	Fuel Consumption (gram)	Difference (%)	Fuel Consumption (gram)	Difference (%)
185	0.6646	6.77%	1.2401	7.98%
200	0.6370	2.34%	1.1864	3.31%
215	0.6225	0.00%	1.1485	0.00%
230	0.6151	-1.18%	1.1210	-2.39%
245	0.6116	-1.75%	1.1011	-4.13%

Among the three parameters that have observable influence on the total fuel consumption cost, the fuel cell delay time constant (τ_e) is not easily improved without significant design changes. Both the number of cells (N) and the cell area (A) are variables at the fuel cell system level that determine the size of a fuel cell system. The efficiency of a fuel cell system improves as its size is increased. At the same time, an increase in the fuel cell system size also increases the gross weight of a fuel cell powered UAV, which consumes more fuel for the same flight trajectory. There may exist an optimal fuel cell size for a given flight trajectory.

5.5 Summary

In this chapter, trajectory optimization problems were formulated as optimal control problems and solved by the proposed generalized framework for pseudospectral methods with the SNOPT NLP solver. The influence of the fuel cell system on the optimal trajectories of a fuel cell powered UAV was investigated in two phases. In the first phase, the point-to-point optimal trajectories of the fuel cell powered configuration and that of the conventional gas powered configuration were compared with different performance index functions. Most significant were the differences in the minimum fuel point-to-point

optimal trajectories. In the second phase, the optimal fuel costs of the minimum fuel point-to-point optimal trajectories were compared with regard to different fuel cell system model parameters. Among different fuel cell system model parameters, the fuel cell delay time constant (τ_e), the number of cells (N) of the fuel cell system, and the cell area (A) of the fuel cell system had significant influence on the optimal fuel consumption cost.

CHAPTER 6

3-D MINIMUM FUEL ROUTE PLANNING AND PATH GENERATION

6.1 Introduction

Since endurance is one of the most important performance criteria for UAVs, minimizing fuel consumption is often desired to be incorporated into the route planning process. As the minimum fuel optimal trajectories of conventional gas powered UAVs are similar to their minimum distance optimal trajectories, route planning problems for conventional gas powered UAVs are usually formulated to minimize the distance. Several examples of route planning problems for UAVs are formulated as Traveling Salesman Problems for the Dubins vehicle (DTSP) [100,101,102,103], where the objective is to find the minimum distance tour that satisfies the Dubins vehicle's curvature constraints.

In a route planning problem, a UAV is expected to visit each waypoint exactly once and return to the starting point, and the objective is to find the optimal sequence of waypoints. This problem is similar to the well-known Travelling Salesman Problem (TSP), which is one of the most widely studied combinatorial optimization problems [104]. In [105], various methods for solving TSPs are classified into two categories: exact methods and approximate methods. With an exact method, the solution found is always optimal. Examples of exact methods are the integer programming method [106] and the dynamic programming method [107]. The main disadvantage of an exact method is that the computation time increases significantly when the size of the problem increases. An approximate method, on the other hand, tries to find a solution close to the optimal

solution. Common examples of approximate methods are heuristic methods, which construct an initial solution and improve the solution through iterative procedures such as k-opt algorithms, tabu search algorithms, or genetic algorithms [108]. K-opt algorithms are local optimization techniques that find the optimal solution near the initial solution. Tabu search algorithms perform repeated runs of local optimization algorithm with randomized initial solutions. Genetic algorithms are global optimization techniques that iteratively improve the solutions through crossover and mutation operators.

The purpose of a Euclidean Traveling Salesman Problem (ETSP) is to find the minimum-distance tour for a given set of points in two dimensions. Paths obtained from ETSPs are usually not feasible for UAVs due to the kinematic constraints [109]. The route planning problem for UAVs is often formulated as a TSP for the Dubins vehicle (DTSP). Different from conventional TSPs, DTSPs require the UAV's heading angles at the intermediate waypoints to determine the tour cost. With this additional variable at each waypoint, exact methods for TSPs are very difficult to construct as the costs between the waypoints cannot be calculated when the heading angles at the intermediate waypoints are not yet determined. Hence, almost all the methods for solving the DTSPs are classified as heuristic methods [103,109,110,111]. One of the main differences among different algorithms for DTSPs is the treatment of the UAV heading angles at the intermediated waypoints. In [109], an alternating algorithm was proposed to find the feasible tour for a DTSP based on the optimal solution of an ETSP. In [110], a random heading algorithm was proposed to determine the heading angles at the intermediate waypoints. In [103], the heading angle at each waypoint was encoded as a free variable, which was optimized using a genetic algorithm. The optimal route plans from different

heading algorithms were highly influenced by the density of the waypoints [103,109,110,111].

The minimum fuel point-to-point optimal trajectories and the Dubins curves [112] are similar in some aspects, and they are different in other aspects. The Dubins curves in two dimensions and three dimensions are calculated using closed-form equations. The minimum fuel point-to-point optimal trajectories are obtained by solving trajectory optimization problems, for which much greater computing resources are required. However, a trajectory optimization method can handle more complex UAV dynamic constraints, and it can solve problems with different performance index functions. Since the Dubins curves are optimized only for a minimum distance, the optimal route plan for a DTSP is optimized only for a minimum distance. For a fuel cell powered UAV, a minimum distance route plan may not be fuel optimal when there are height variations between the waypoints. Additional research efforts are required to address the minimum fuel route planning and path generation problems in three dimensions.

This chapter proposes a new method to solve three-dimensional minimum fuel route planning and path generation problems for a fuel cell powered UAV. The problem statement and proposed method are discussed in Section 6.2. In Section 6.3, a fuel consumption cost model for the minimum fuel point-to-point optimal trajectories is developed. In Section 6.4, a genetic algorithm with different heading algorithms is implemented to find the minimum fuel route plan, which is improved by using crossover and mutation operators iteratively. In Section 6.5, optimal fight paths from one waypoint to another waypoint are generated by connecting the waypoints with minimum fuel optimal trajectories, and a simplified model for path generation at negative flight path

angles is proposed due to the nonlinearities in the fuel cell performance model at low current levels. Finally, the proposed method with different heading algorithms is used to investigate a case study with a high waypoint density problem and a low waypoint density problem.

6.2 Problem Statement and Proposed Method

A three-dimensional minimum fuel route planning problem (as shown in Figure 6.1) is defined as follows: For a given set of waypoints $\{P_1, P_2, ..., P_N\}$, a given initial heading angle (ψ_1), and a given final heading angle (ψ_{N+1}) at P_1, what is the optimal sequence of waypoints that a fuel cell powered UAV should fly so that the associated fuel consumption is minimal? The sequence of waypoints must start from P_1 and end at P_1. The waypoints P_2 to P_N are to be visited exactly once. The position of each waypoint (P_i) is specified by its three-dimensional coordinates (x_i, y_i, z_i).

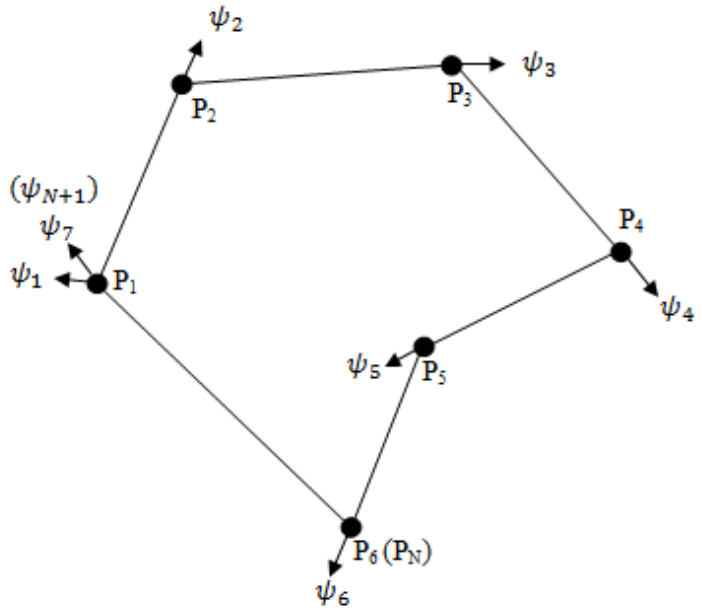

Figure 6.1 Route planning problem definition.

A path generation problem is defined as follows: For a given sequence of waypoints $\{P_1, P_2, ..., P_N, P_1\}$, a given initial heading angle (ψ_1), and a given final heading angle (ψ_{N+1}) at P_1, what is the optimal flight path for a fuel cell powered UAV that is both dynamically feasible and fuel optimal?

Figure 6.2 shows the proposed method to solve three-dimensional minimum fuel route planning and path generation problems for a fuel cell powered UAV. The minimum fuel route planning problem is treated as a variant of the Traveling Salesmen Problem (TSP), where the cost between the waypoints is the corresponding fuel consumption. The first step in the proposed method is to develop a fuel consumption cost model for the point-to-point minimum fuel optimal trajectories so that the fuel consumption cost for each segment $\{P_i$ to $P_{i+1}\}$ can be computed directly without solving a trajectory optimization problem. The cost model is developed by consolidating the fuel consumption characteristics of the minimum fuel point-to-point optimal trajectories. The second step is to find the optimal sequence of waypoints $\{P_1, P_2, ..., P_N, P_1\}$ using a genetic algorithm, where the segmental cost is computed from the developed cost model. The final step is to generate the minimum fuel flight path by connecting the waypoints with minimum fuel point-to-point optimal trajectories. In this step, the point mass model of a fuel cell powered UAV, including the fuel cell dynamics, is formulated as the dynamic constraints.

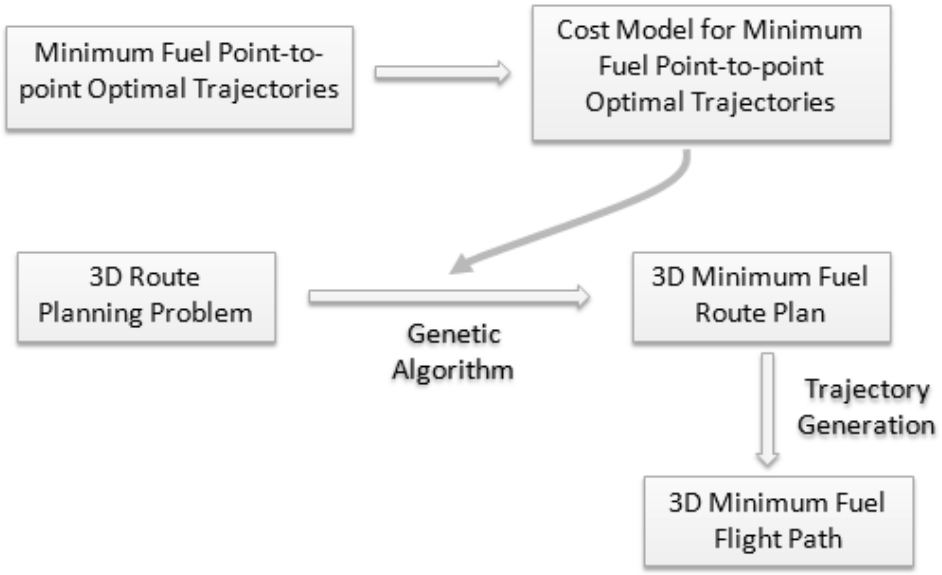

Figure 6.2 Proposed method for a three-dimensional minimum fuel route planning and path generation problem.

6.3 Cost Model for Minimum Fuel Point-to-point Optimal Trajectories

Although the trajectory optimization method discussed in the previous section is capable of finding the minimum fuel optimal trajectory for a given initial position and final position, a significant amount of computing time is required to converge to the optimal solution. It is impractical to solve the segmental optimal cost using the trajectory optimization method during the route planning process. One of the key elements in the proposed method for solving three dimensional minimum fuel route planning problems is the development of a fuel consumption cost model for minimum fuel point-to-point optimal trajectories. This model includes both the steady-state fuel consumption cost and the transient fuel consumption cost. The steady-state fuel consumption cost is calculated from the steady state performance of the UAV and the transient fuel consumption cost is calculated by using an empirical equation derived from the characteristics of the transient cost associated with the optimal trajectories.

6.3.1 Proposed Fuel Consumption Cost Model

A minimum fuel point-to-point trajectory optimization problem is defined by the initial position (p_0), initial heading angle (ψ_0), final position (p_f), and final heading angle (ψ_f). A typical minimum fuel point-to-point optimal trajectory, as shown in Figure 6.3, consists of three phases: the transition from the initial level flight state to an ascend/descend flight state, the steady ascend/descend flight state, and the transition from the ascend/descend flight state to the final level flight state. The first and final phases are transient flight conditions, and the second phase is a steady state flight condition. The fuel consumption cost associated with the optimal trajectories is estimated separately for the transient flight states and the steady state flight state. Equations (6.1)-(6.3) show the proposed fuel consumption cost model, which consists of the steady state fuel consumption cost (m_{fuel_s}) and the transient fuel consumption cost (m_{fuel_t}). The steady state fuel consumption cost is determined using Equation (6.2), in which the fuel consumption rate as a function of flight path angle (γ) is obtained by trimming the UAV model at different flight path angles. The transient fuel consumption cost is estimated using Equation (6.3) with a second order polynomial function of the heading angle changes, $(\theta - \psi_0)$ and $\left(\psi_f - \theta\right)$.

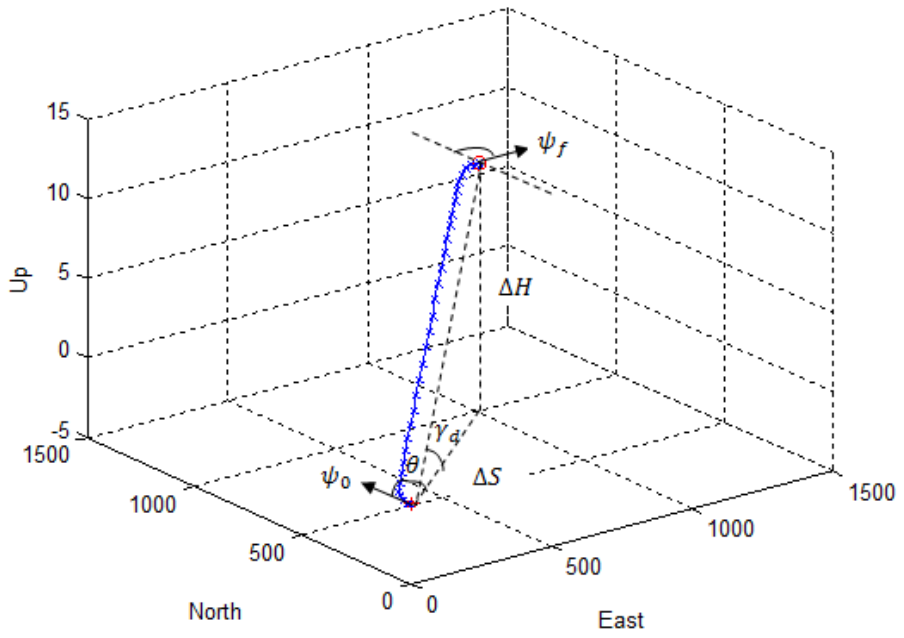

Figure 6.3 A typical optimal trajectory for the minimum fuel trajectory optimization problem.

$$m_{fuel}(p_0,\ p_f, \psi_0, \psi_f) = m_{fuel\_s} + m_{fuel\_t} \tag{6.1}$$

$$m_{fuel\_s} = \dot{m}_{fuel}(\gamma)\frac{\Delta H}{V \sin\gamma} \tag{6.2}$$

$$m_{fuel\_t} = c_1(\gamma)(\theta - \psi_0)^2 + c_1(\gamma)\left(\psi_f - \theta\right)^2 + c_0(\gamma) \tag{6.3}$$

6.3.2 Transient Fuel Consumption Cost at Different Azimuth Angles

The transient fuel consumption cost, shown in Equation (6.3), is a quadratic function of the heading angle change required from the initial position to the final position. Only two variables, c_0 and c_1, are required to determine the transient fuel consumption cost. The variable c_1 is associated with the heading angle changes, $(\theta - \psi_0)$ and $(\psi_f - \theta)$. The variable c_0 represents the discrepancy between the steady state cost (m_{fuel_s}) and the actual fuel consumption cost (m_{fuel}).

Figure 6.4 to Figure 6.7 show the comparisons between the transient fuel consumption cost from Equation (6.3) and that from the optimal trajectories at different azimuth angles (θ) and different final heading angles (ψ_f). In Figure 6.4, the transient fuel consumption cost is calculated with the coefficients, c_0 and c_1, derived from the optimal trajectories at one azimuth angle ($\theta = 0^o$). In Figure 6.5, the transient fuel consumption cost is calculated with coefficients derived from the optimal trajectories at two azimuth angles ($\theta = 0^o$ and $\theta = 45^o$). The transient fuel consumption costs calculated with coefficients from optimal trajectories at three azimuth angles and four azimuth angles are shown in Figure 6.6 and Figure 6.7. As illustrated in these comparisons, Equation (6.3) accurately predicts the transient fuel consumption cost of the optimal trajectories. Since there are only two variables in Equation (6.3), only a small number of optimal trajectories at each flight path angle are required to determine these two coefficients.

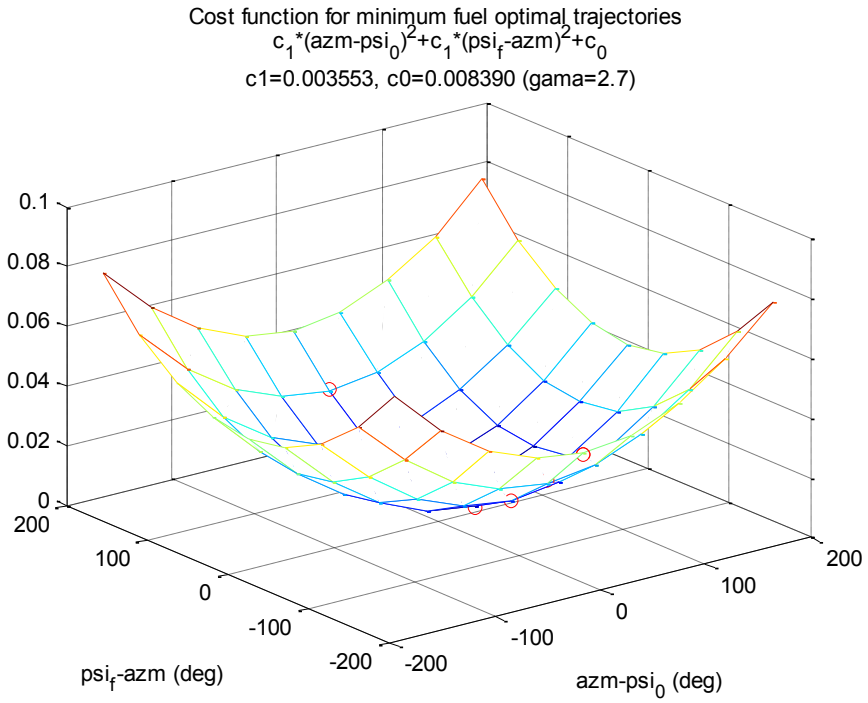

Figure 6.4 Transient fuel consumption cost calculated with coefficients derived from optimal trajectories at one azimuth angle.

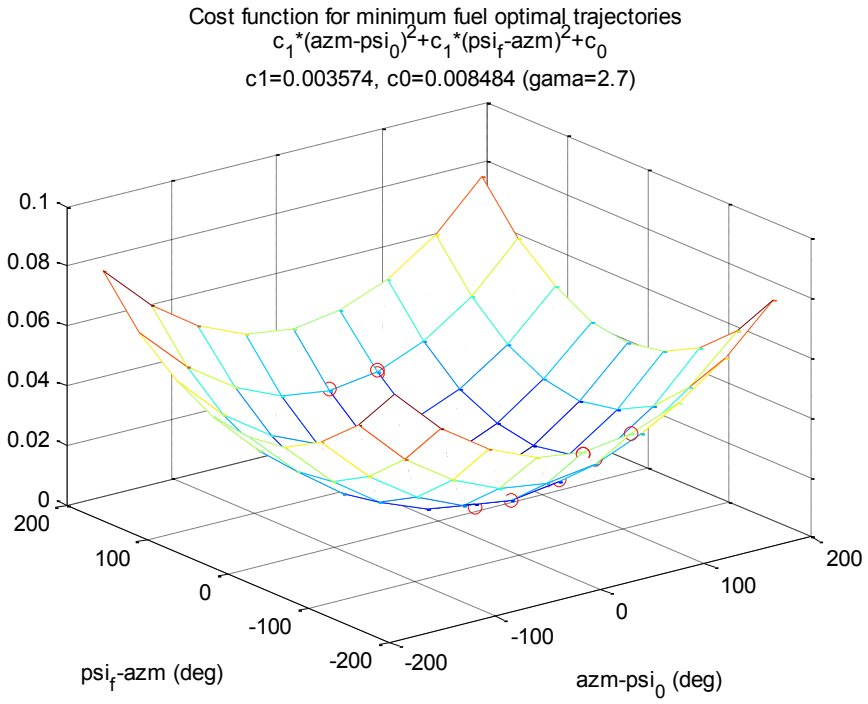

Figure 6.5 Transient fuel consumption cost calculated with coefficients derived from optimal trajectories at two azimuth angles.

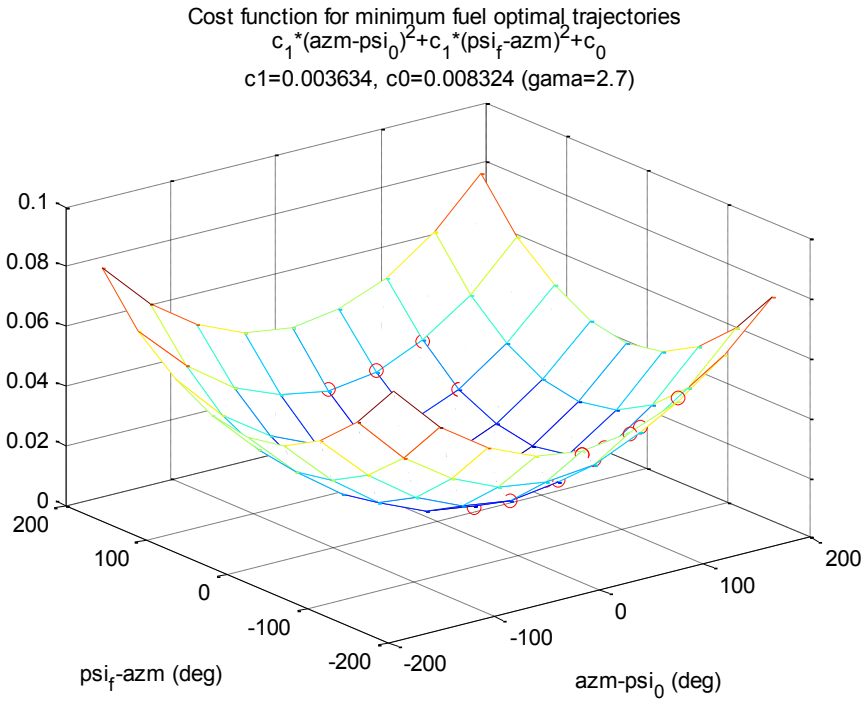

Figure 6.6 Transient fuel consumption cost calculated with coefficients derived from optimal trajectories at three azimuth angles.

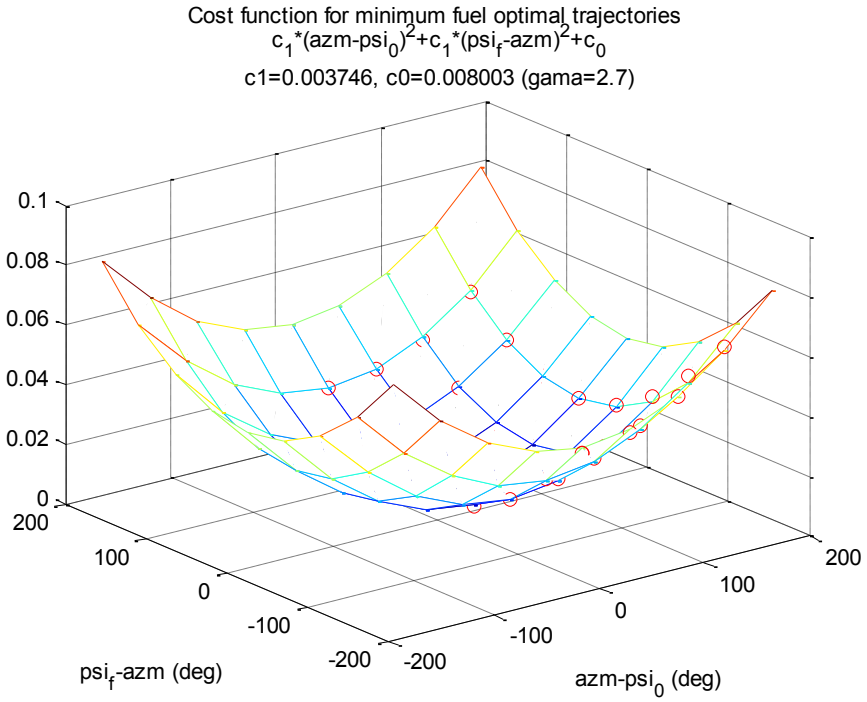

Figure 6.7 Transient fuel consumption cost calculated with coefficients derived from optimal trajectories at four azimuth angles.

6.3.3 Transient Fuel Consumption Cost at Different Flight Path Angles

As shown in Equation (6.3), the coefficients c_0 and c_1 are functions of flight path angles. The transient fuel consumption costs as a function of heading angle changes $(\theta - \psi_0)$ and $(\psi_f - \theta)$ at different flight path angles are shown in Figure 6.8 to Figure 6.13. At low flight path angles, the transient fuel consumption cost associated with heading angle change is more significant. At high flight path angles, the transient fuel consumption cost is mostly caused by the discrepancy between the steady state cost (m_{fuel_s}) and the actual fuel consumption cost (m_{fuel}). When the flight path angle is small, the optimal trajectories are similar to straight line flight paths. The transient fuel consumption cost associated with the heading angle change dominates the total transient cost. When the flight path angle is high, the optimal trajectories are S-shaped flight paths. Cost associated with heading angle change is not significant. Instead, the transient cost is dominated by the flight path angle changes. This trend is shown Figure 6.14 and Figure 6.15. In Figure 6.14, the coefficient c_1 approaches zero when the flight path angle is more than six degree. In Figure 6.15, the coefficient c_0 is almost zero when the flight path angle is less than two degrees.

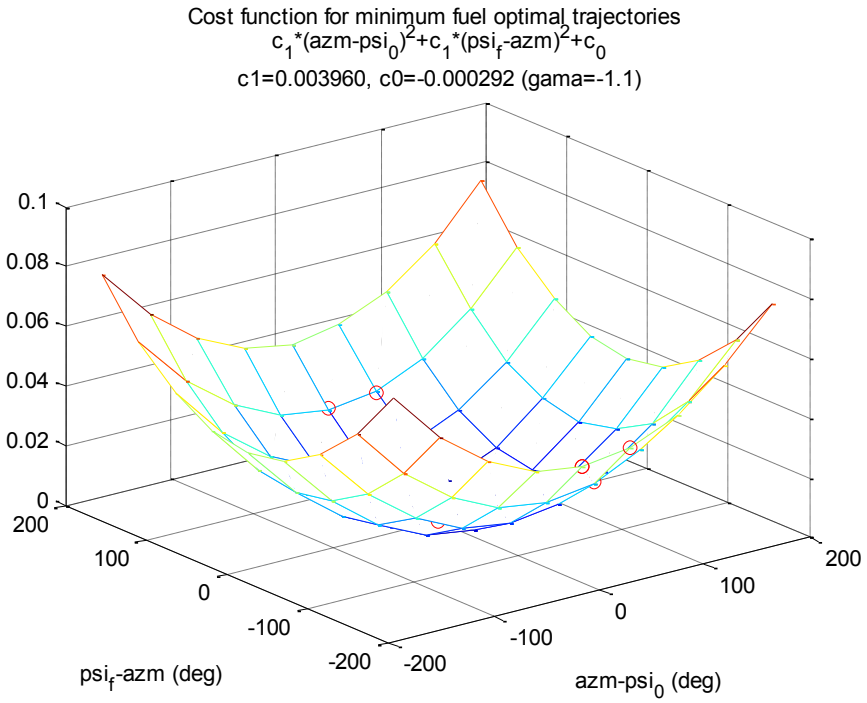

Figure 6.8 Transient fuel consumption cost at $\gamma = -1.1^{o}$.

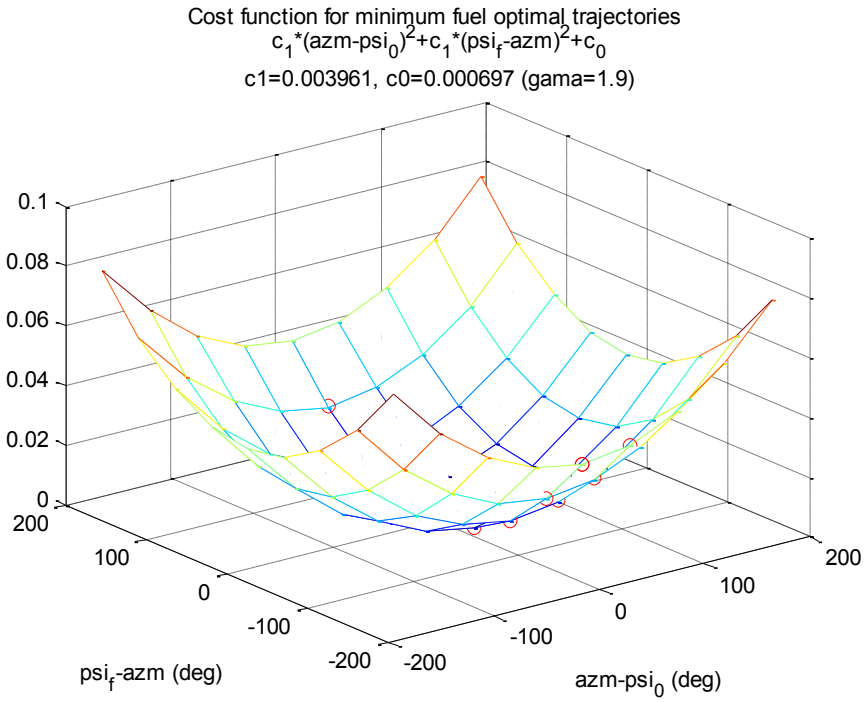

Figure 6.9 Transient fuel consumption cost at $\gamma = 1.9^{o}$.

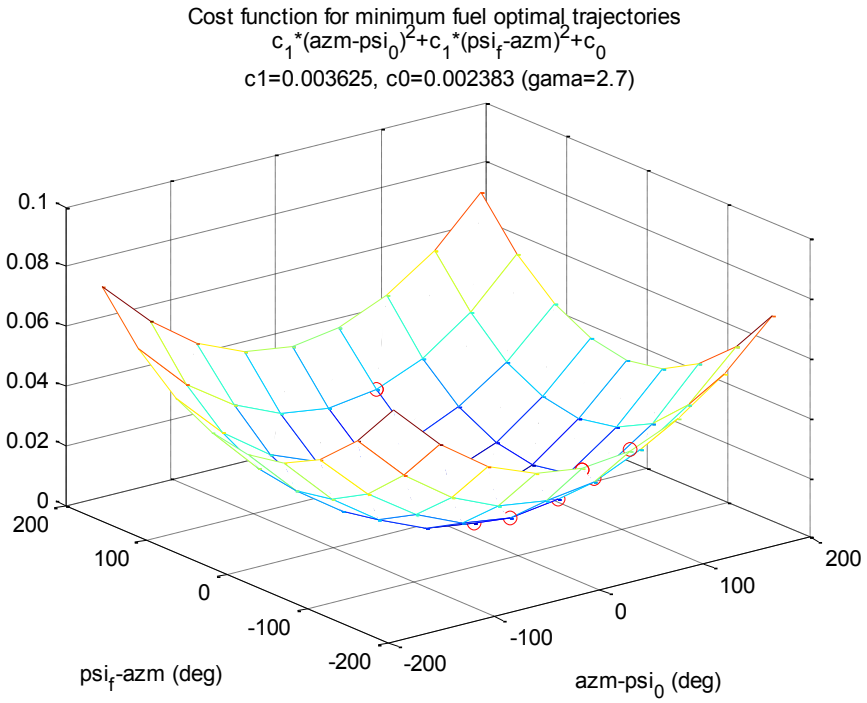

Figure 6.10 Transient fuel consumption cost at $\gamma = 2.7^{o}$.

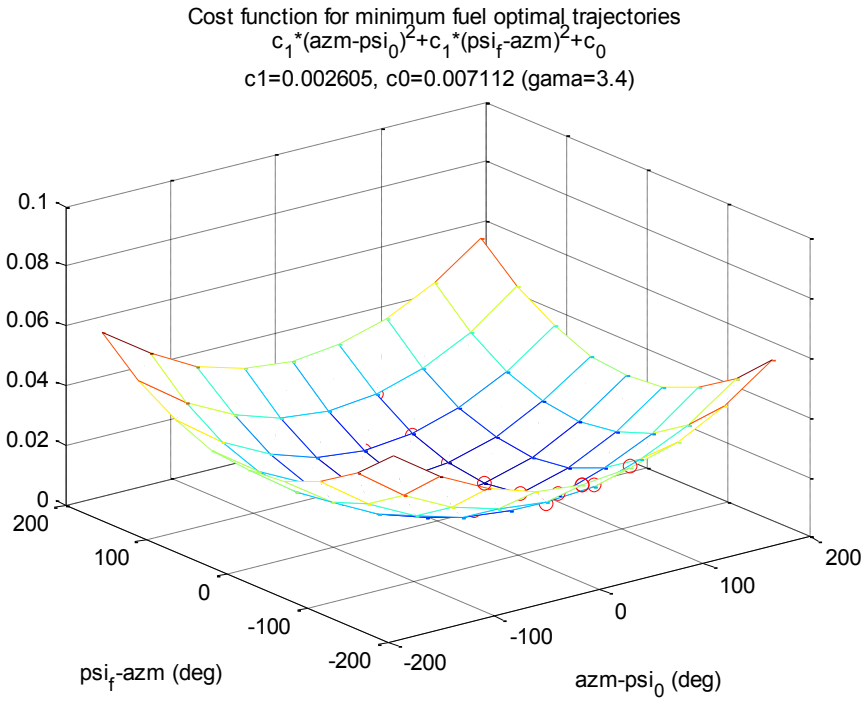

Figure 6.11 Transient fuel consumption cost at $\gamma = 3.4^{o}$.

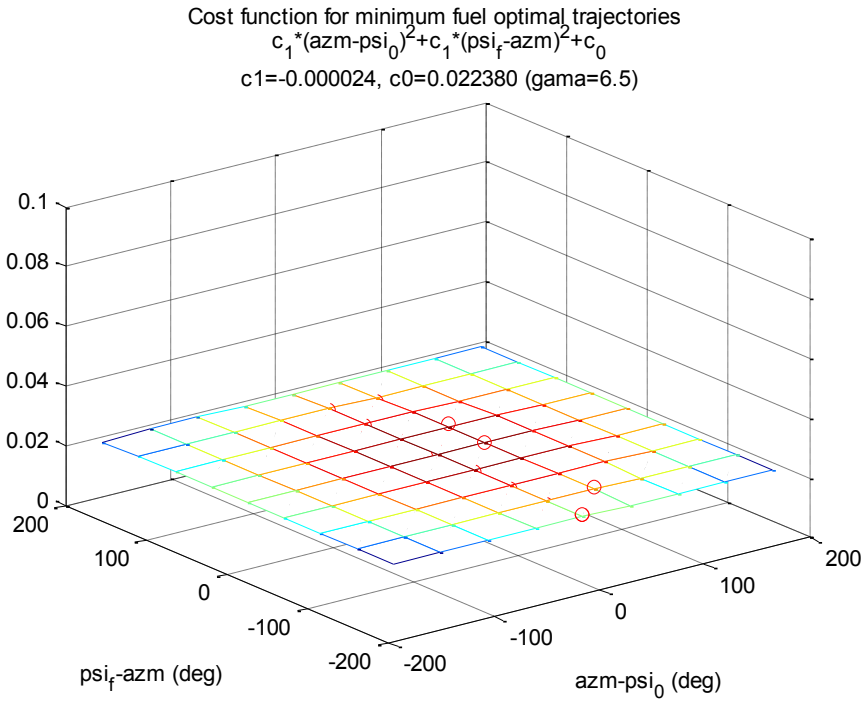

Figure 6.12 Transient fuel consumption cost at $\gamma = 6.5^{o}$.

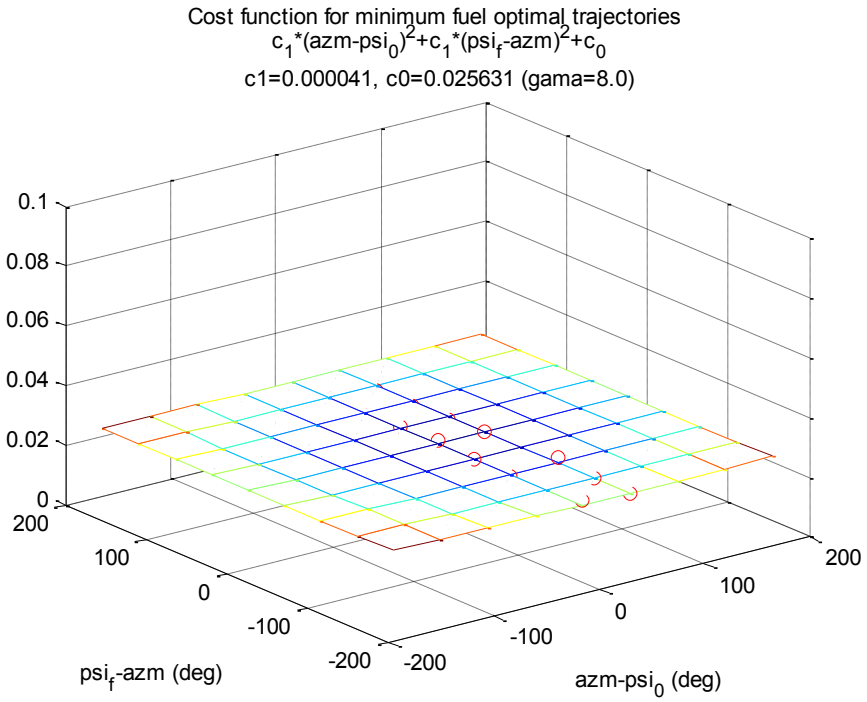

Figure 6.13 Transient fuel consumption cost at $\gamma = 8.0^{o}$.

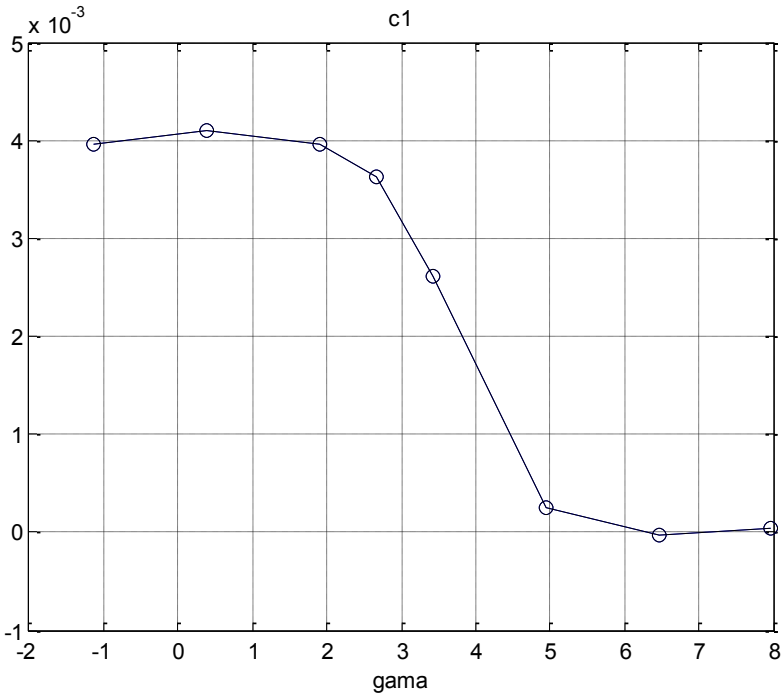

Figure 6.14 Coefficient c_1 at different flight path angles.

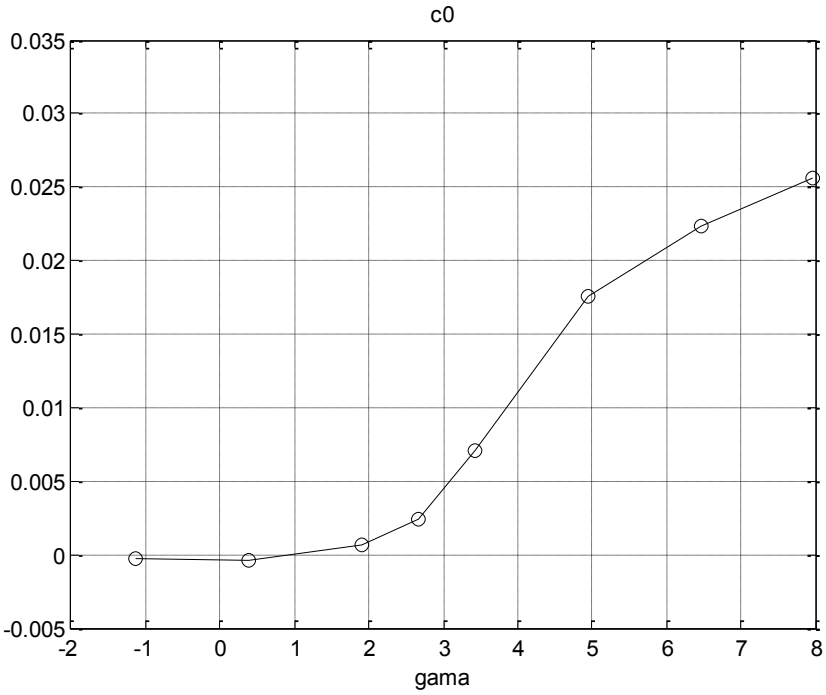

Figure 6.15 Coefficient c_0 at different flight path angles.

6.4 3-D Minimum Fuel Route Planning

As defined in Section 6.2, the solution of a three-dimensional minimum fuel route planning problem is the optimal sequence of waypoints that a fuel cell powered UAV should fly for a given set of waypoints. For any given initial position (p_0), initial heading angle (ψ_0), final position (p_f), and final heading angle (ψ_f), the cost for the minimum fuel optimal trajectory can be directly computed using Equations (6.1) to (6.3). As compared to exact methods, genetic algorithms have the advantage of finding near optimal solutions with relatively fewer iterations, and as compared to other approximate methods, genetic algorithms find the near optimal solutions globally [113]. In this section, a genetic algorithm is implemented to solve three-dimensional route planning problems. Different from conventional combinatorial problems, the three-dimensional minimum fuel route planning problem requires the heading angles at the intermediate waypoints. Different heading algorithms from the literature are implemented in this section. Also discussed in this section is the influence of the transient fuel consumption cost on the optimal route plan.

6.4.1 Genetic Algorithm for 3-D Minimum Fuel Route Planning

Genetic algorithms are evolutionary algorithms that attempt to mimic some of the processes that take place in natural evolution [114]. The first genetic algorithm was introduced by John Holland in 1975, in which he used a string of binary numbers to represent a candidate solution [115]. Since then, many variations of genetic algorithms with different representations and operators have been studied in the literature. Most of these have been comprehensively reviewed in [116]. In this chapter, a string of integer numbers is used to represent a candidate route plan. The ordered crossover operator [117]

and the mutation swap operator [118] are used to generate new route plans during the evolution processes.

The genetic algorithm for minimum fuel route planning problems is shown in Figure 6.16. As defined in Section 6.2, a route plan is a sequence of waypoints, where each waypoint is visited exactly once. A string with integer numbers representing the waypoints is used to encode the candidate route plan. The population is a collection of candidate solutions. The initial population is randomly generated. Different from a conventional TSP, in the genetic algorithm here, the cost between waypoints for a minimum fuel route planning problem can be calculated only when the UAV heading angle at the each waypoint is determined. Hence, a heading algorithm is inserted before the computation of the fitness value of each individual solution. In this paper, the fitness value is the total fuel cost, which is calculated using Equations (6.1) to (6.3). During the evolution process of the genetic algorithm, new populations are generated by applying the crossover and mutation operators to the previous population. Similar to the initial population, the new population also needs to go through a heading algorithm before the fitness value can be calculated. At the end of each iteration, only the individuals with best fitness values are stored in the new population. When the number of iterations reaches the maximum iteration number (N_{max}) the iteration process stops, and the genetic algorithm outputs the best solution as the optimal route plan.

Genetic Algorithm for Minimum Fuel Route Planning Problems

1: Set GA parameters: N_{pop}, N_{max}, R_{cross}, R_{mut}
2: Encode the problem
3: Generate an initial population randomly
4: Execute the heading algorithm on the initial population
5: Calculate the fitness value of each individual in the initial population
6: Sort the initial population by fitness values
7: for idx=1: N_{max}
8: Generation of new population
9: Execute the crossover operator
10: Execute the mutation operator
11: Execute the heading algorithm
12: Calculate the fitness of the new population
13: Update the current population with better solutions
14: end for
15: Output the best solution from the current population

Figure 6.16 Genetic algorithm for a minimum fuel route planning problem.

There are two important steps to generating new populations: the crossover operation and the mutation operation. In the crossover operation, two new strings (N1 and N2) are generated from two parent strings (P1 and P2). A route plan is coded with integer numbers, each of which, except for the first and last number, must appear exactly once. The ordered crossover [117] operator ensures the new individuals are always valid. An ordered crossover operator works in the following steps. In the first step, two random numbers are generated to determine the locations of the crossover points. In the second step, the numbers between the crossover points are kept unchanged. The remaining numbers to fill the first new individual (N1) are from the second parent (P2), as are the remaining numbers to fill the second new individual (N2). In the third step, the remaining numbers are filled in each new individual from the second crossover point onwards by omitting the numbers that have already appeared. For example, number 4 and 5 have already appeared in N1, only the numbers (7 6 3 2) from (7 6 3 4 5 2) are filled in N1.

The second new individual (N2) is generated in the same manner. After the crossover operation, two new individuals (N1 and N2) are generated from the parents (P1 and P2) and are always valid.

Step 1:

```
P1: (1) 2 3 4 5 6 7 (1)
P2: (1) 3 4 5 2 7 6 (1)
              ^     ^
```

Step2:

```
N1: (1) * * | 4 5 | * * (1) Remaining numbers: 7 6 3 4 5 2
N2: (1) * * | 5 2 | * * (1) Remaining numbers: 6 7 2 3 4 5
```

Step 3:

```
N1: (1) 3 2 | 4 5 | 7 6 (1)
N2: (1) 3 4 | 5 2 | 6 7 (1)
```

In the mutation operation, one new individual (N1) is generated from one parent (P1) and the mutation swap operator [118] is used in this chapter. Similar to a crossover operation, a random number is also generated to determine the mutation location. The mutation swap generates a new individual by swapping the numbers before and after the mutation location as follows:

```
P1:  (1) 2 3 4 | 5 6 7 (1)
N1:  (1) 5 6 7 2 3 4 (1)
```

There are two parameters governing the probabilities of the crossover and mutation processes: crossover rate (R_{cross}) and mutation rate (R_{mut}). Both the crossover rate and the mutation rate are in the range of 0 to 1. The crossover rate used in this chapter is 0.85, and the mutation rate used in this chapter is 0.10. These two values are determined by comparing the results obtained for some example route planning problems at different crossover rates and mutation rates. The values of these two parameters are similar to the values used in [103].

6.4.2 Different Heading Algorithms

Similar to a DTSP, computing the fuel consumption cost of a candidate solution for a minimum fuel route planning problem requires the heading angle at each waypoint. In this section, three heading algorithms are presented, the random heading algorithm [110], the alternative heading algorithm [109] and the leg heading algorithm. In the random heading algorithm [110], the heading angle at each waypoint is randomly generated (as shown in Figure 6.17(a)). In the alternative heading algorithm [109], the heading angle at each waypoint is arranged in such a way that the flight path between two alternative segments is perfectly straight (as shown in Figure 6.17(b)). The leg heading algorithm uses the leg direction as the heading angle at each waypoint (as shown in Figure 6.17(c)).

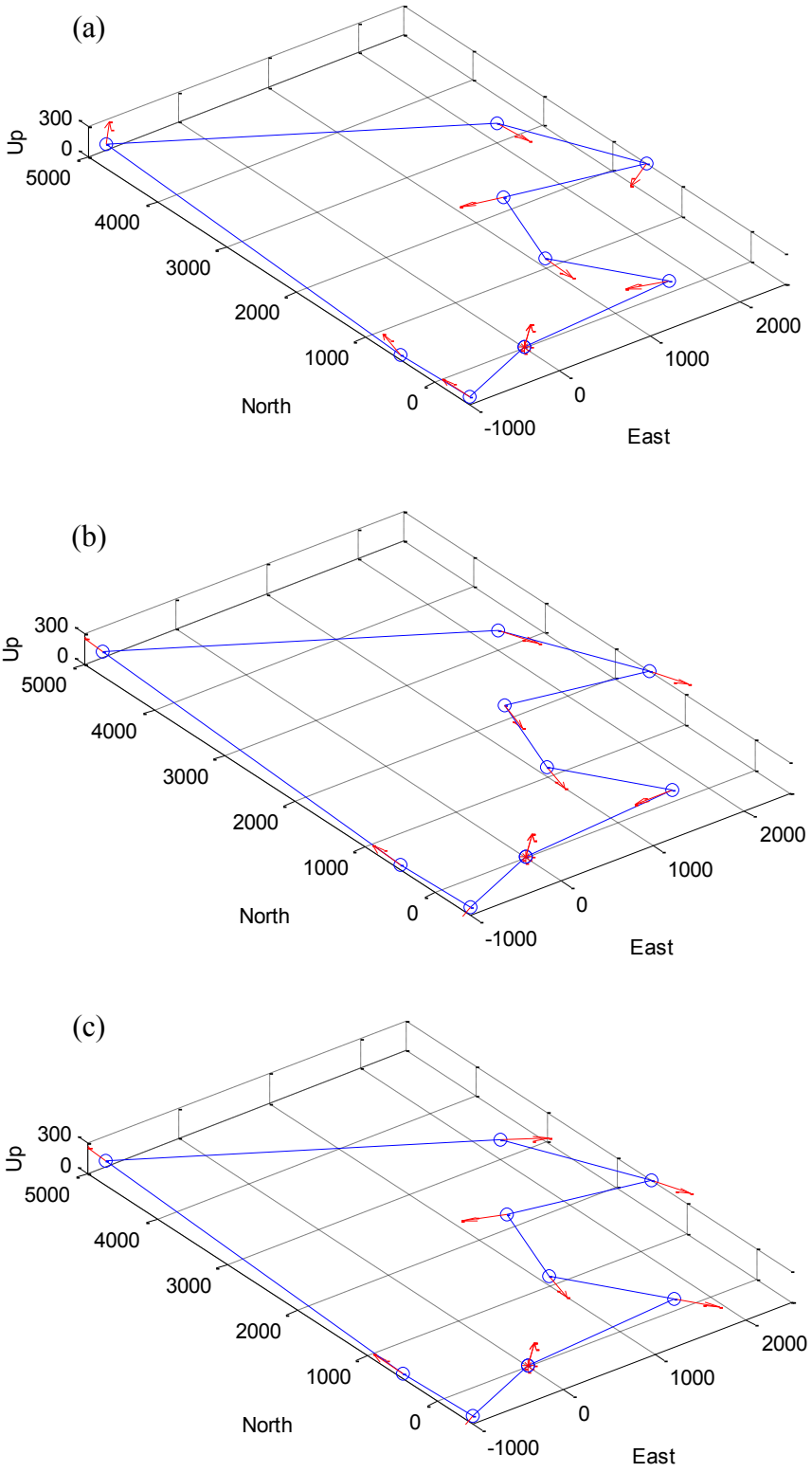

Figure 6.17 Different heading algorithms:
(a) Random heading algorithm, (b) Alternative heading algorithm, (c) Leg heading algorithm.

In the genetic algorithm implemented in this chapter, the heading angles at the intermediate waypoints are determined after the sequence of waypoints is generated. The influence of the random heading algorithm and the alternative heading algorithm on the optimal route plan is different from that in the original implementation in [109] and [110]. In [109] and [110], the heading angles at the intermediate waypoints are computed after the sequence of waypoints is obtained from the ETSP optimization process, in which the heading angles do not influence the sequence of the waypoints. In this chapter, the candidate solutions are sorted after the heading angles are determined. As the fitness values of the same sequence of waypoints with different heading angles are different, the decision of whether a sequence of waypoints is the best solution is influenced by the heading angles at the intermediate waypoints. A similar heading algorithm implementation is presented in [103], in which the heading angles at the intermediate waypoints are formulated as free variables, which are optimized through iterations.

With the proposed fuel consumption cost model (as shown in Equations (6.1) to (6.3)), the heading angles at the intermediate waypoints influence only the transient fuel consumption cost (Equation (6.3)). In the random heading algorithm, both ψ_0 and ψ_f are randomly varied to minimize the function m_{fuel_t} for each segment. In the alternative heading algorithm, the alternative segments are straight segments. This means $\theta - \psi_0 = 0$ and $\psi_f - \theta = 0$ at the alternative segments. In the leg heading algorithm, the final heading angle at each segment is the same as the leg direction. This means $\psi_f - \theta = 0$ for each segment for the leg heading algorithm. Among the three heading methods, only the random heading algorithm requires an iterative procedure to find the optimal heading

angles. Both the alternative heading algorithm and the leg heading algorithm compute the heading angles at the intermediate waypoints deterministically.

6.4.3 Effect of Transient Fuel Consumption Cost

The transient fuel consumption cost model, as shown in Equation (6.3), is an empirical function derived from the minimum fuel point-to-point optimal trajectories. The parameters that influence the cost are the heading angle changes required from the initial position to the final position, $(\theta - \psi_0)$ and $(\psi_f - \theta)$. The transient fuel consumption cost can also be viewed as a penalty function for sharp turn trajectories. The resulting optimal route plan is expected to avoid sharp turn trajectories. Figure 6.18(a) shows the optimal route plan from for an example route planning problem that considers the transient fuel consumption cost, and Figure 6.18(b) shows the optimal route plan that does not consider the transient fuel consumption cost. The route plan shown in Figure 6.18(b) has a very sharp turn, which should be avoided to minimize the fuel consumption. The genetic algorithm with the proposed cost model is expected to find a minimum fuel optimal route plan with less aggressive turning maneuvers.

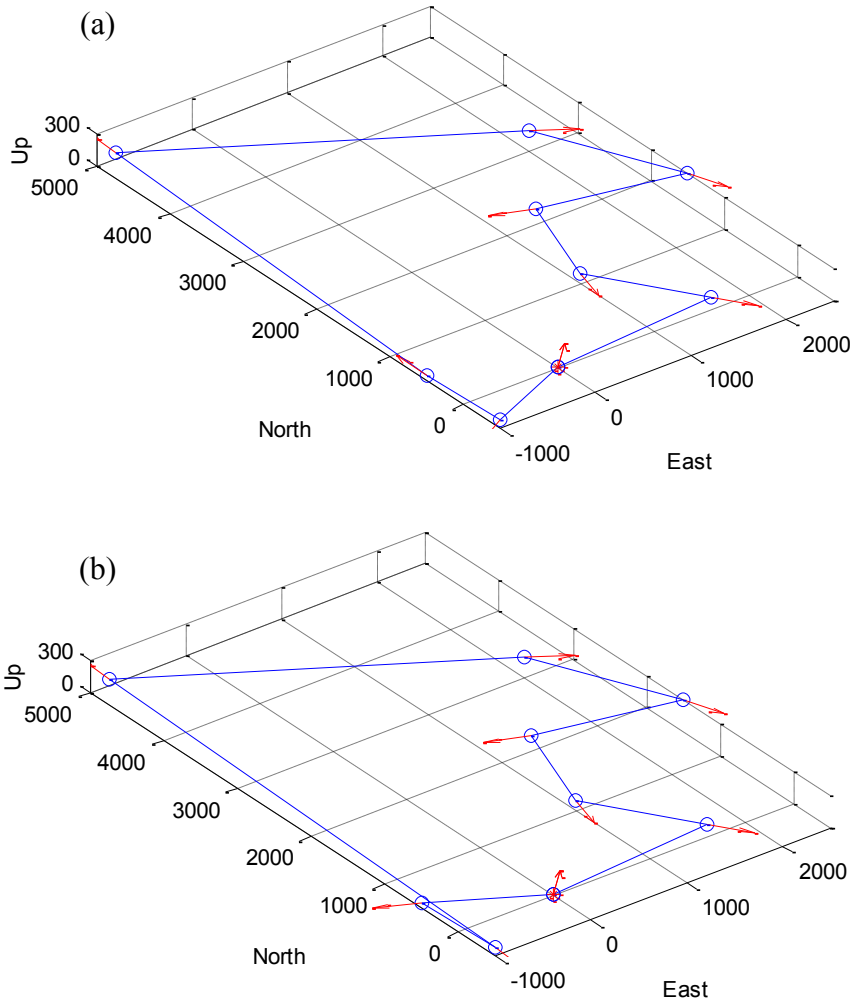

Figure 6.18 Influence of the transient fuel consumption cost on the optimal route plan: (a) with transient fuel consumption cost, (b) without transient fuel consumption cost.

6.5 3-D Minimum Fuel Path Generation

The three-dimensional minimum fuel route planning process presented in the previous section finds the minimum fuel route plan for a given set of waypoints. To ensure the fuel consumption is minimized in the actual flight, a three-dimensional minimum fuel flight path for visiting all the waypoints is required. In this section, the minimum fuel flight path for a given minimum fuel route plan is generated by connecting the waypoints with

the minimum fuel point-to-point optimal trajectories. The fuel consumption cost from the proposed cost model is verified against that of the minimum fuel optimal trajectories.

6.5.1 Path Generation and Fuel Consumption Cost Verification

The three-dimensional minimum fuel flight path of a route plan is generated by connecting the waypoints with minimum fuel optimal trajectories. Figure 6.19(a) shows the optimal route plan obtained using the genetic algorithm with the leg heading algorithm. Figure 6.19(b) is the minimum fuel flight path generated using the minimum fuel point-to-point trajectory optimization methods when the fuel cell powered propulsion system dynamics is considered. If the fuel cell powered UAV follows the fight path shown in Figure 6.19(b) when visiting the waypoints, the fuel consumption is minimized.

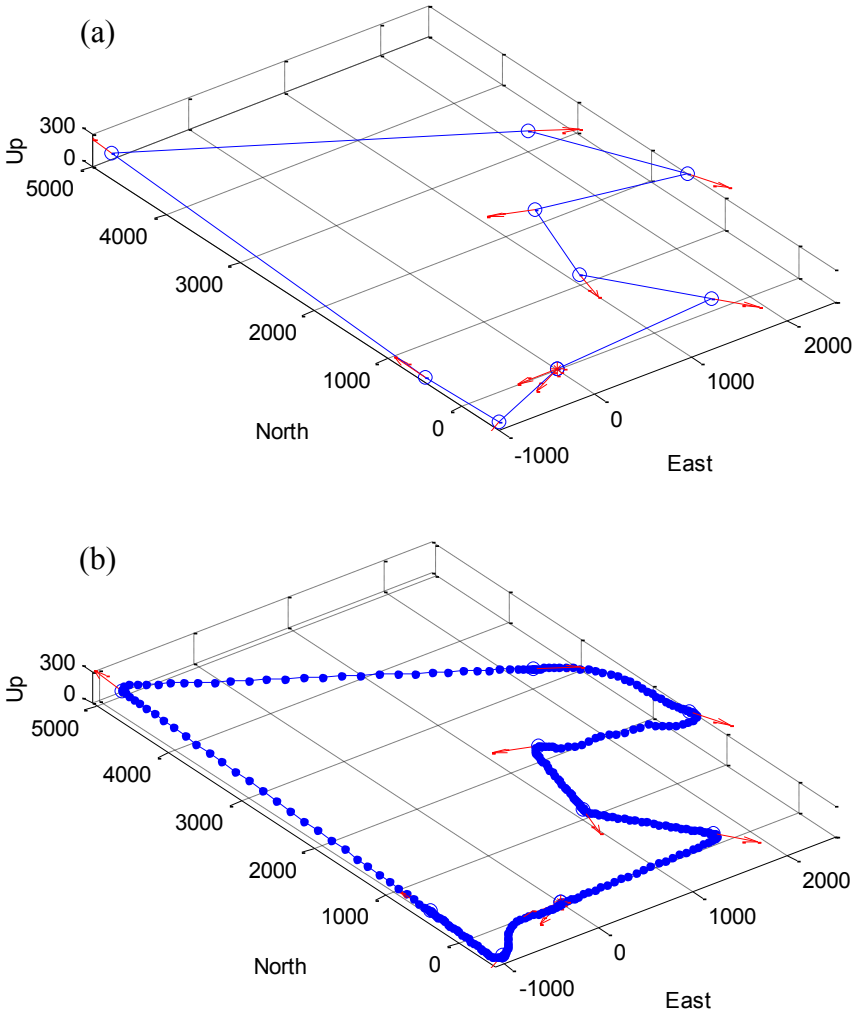

Figure 6.19 Three-dimensional minimum fuel path generation process: (a) minimum fuel route plan, (b) minimum fuel flight path.

Table 6.1 shows the fuel consumption cost for each segment of the minimum fuel flight path shown in Figure 6.19(b). Table 6.1 also shows the fuel consumption cost calculated by using the proposed cost model during the route planning process. A comparison of these two sets of data is shown in Figure 6.20. For the segments with positive flight path angles, the fuel consumption cost calculated using the proposed cost model matches well with the fuel consumption cost from the trajectory generation process. However, for the segments with negative flight path angles, the discrepancy

between the fuel consumption cost calculated using the proposed cost model and that from the trajectory generation process is more significant. This is due to the nonlinearity in the fuel cell performance curve at low current, in which the fuel cell output voltage is very sensitive to the current at low current. This is the main contributing factor to the discrepancies shown in Table 6.1. In the next section, a simplified model for path generation at negative flight path angles is presented in order to ensure successful flight path generation at negative flight path angles.

Table 6.1 Fuel consumption cost for each segment of the minimum fuel flight path. (* segments with large negative flight path angles)

Segments	Gama (degree)	Cost Model	Optimal Cost
1	3.58	0.509	0.513
2	-1.72	0.131	0.131
3	0.00	0.862	0.863
4	2.50	1.197	1.201
5	3.62	0.719	0.724
6*	-6.58	0.021	0.031*
7	-2.74	0.086	0.090
8	0.98	0.289	0.287
9*	-3.93	0.059	0.077*

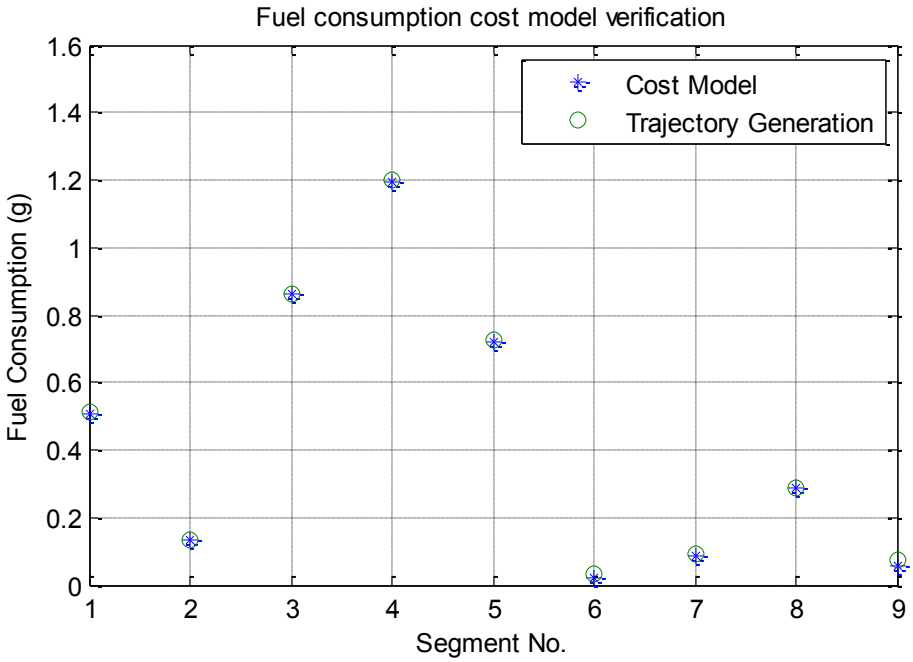

Figure 6.20 Fuel consumption cost model verification.

6.5.2 Path Generation at Negative Fight Path Angle

Since the optimal trajectories of a fuel cell powered UAV at negative flight path angles are similar to minimum distance optimal trajectories, this section uses the Dubins airplane model from [99], which considers only the geometric constraints, for path generation at negative flight path angles. The minimum distance performance index function is shown in Equation (6.4). Equations (6.5) to (6.9) are the three-dimensional kinematic equations of a Dubins airplane, where the flight speed is fixed and the flight trajectory is controlled by the heading angle rate ($\dot{\psi}$) and flight path angle rate ($\dot{\gamma}$).

Minimize:

$$J = \int_{t_0}^{t_f} V \, dt \tag{6.4}$$

Subject to:

$$\dot{x} = V \cos\gamma \cos\psi \tag{6.5}$$

$$\dot{y} = V \cos\gamma \sin\psi \tag{6.6}$$

$$\dot{z} = V \sin\gamma \tag{6.7}$$

$$\dot{\psi} = u_1 \tag{6.8}$$

$$\dot{\gamma} = u_2 \tag{6.9}$$

The optimal trajectories obtained by using the Dubins airplane model and the full model (Equations (5.1) to (5.10)) are compared at different flight path angles (as shown in Figure 6.21 (a) to (f)). In Figure 6.21 (a) to (c), the optimal trajectories of the Dubins airplane model are very similar to that of the full model when the flight path angle is small or negative. When the flight path angle is high (as shown in Figure 6.21 (d)-(f)), the optimal trajectories of the Dubins airplane model are very different from those of the full model. This highlights the importance of minimum fuel trajectory optimization using the full model.

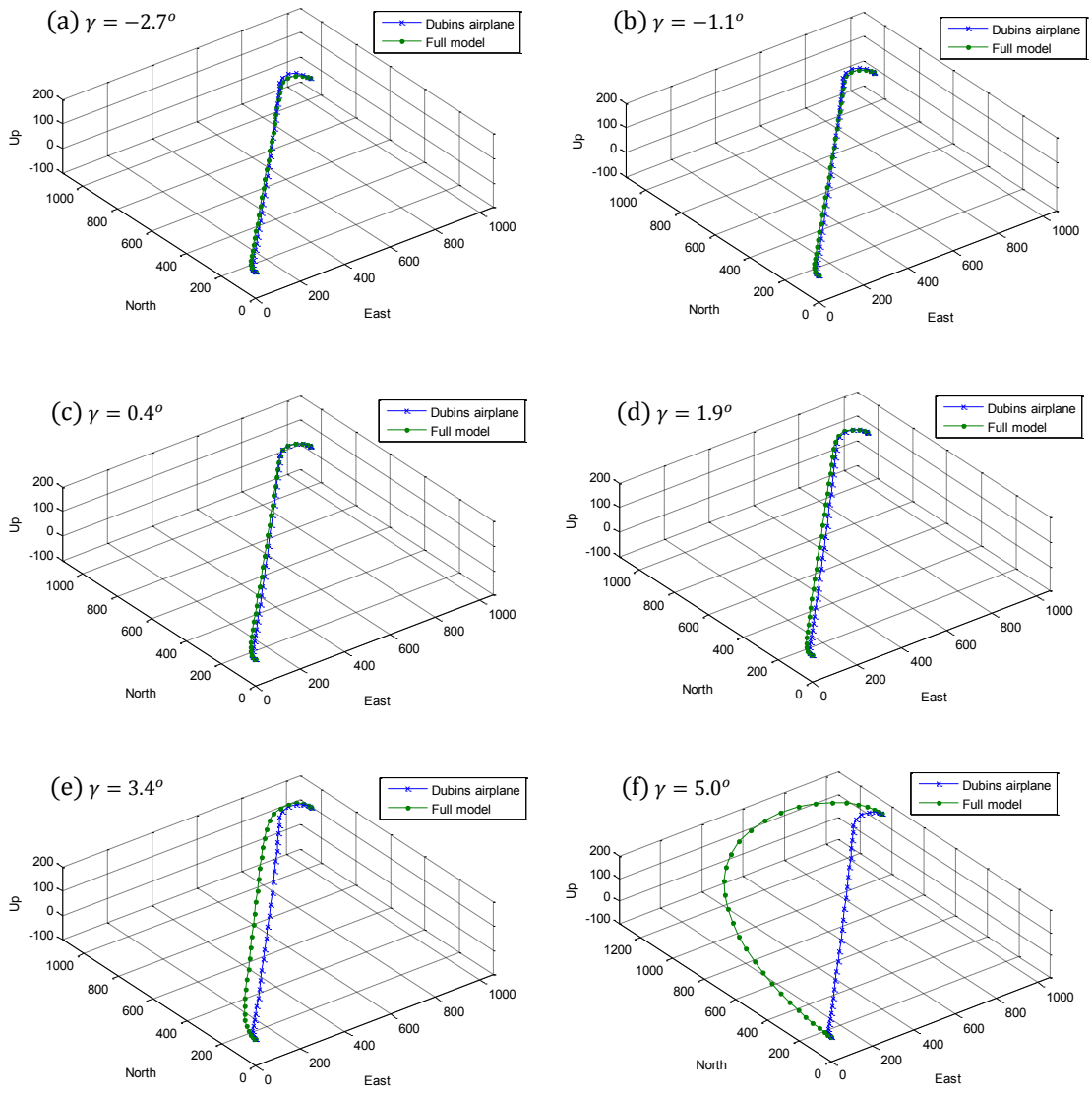

Figure 6.21 (a)-(f) Trajectory optimization using the Dubins airplane model at negative flight path angles.

6.5.3 Case Study with Different Waypoint Densities

Several studies of DTSPs have highlighted that the waypoint density influences the optimal route plan differently for different heading algorithms [103,109,110]. In this section, the proposed method for three-dimensional route planning and path generation problems is used to solve a low waypoint density problem and a high waypoint density problem. The genetic algorithm parameters are summarized in Table 6.2. Since there are

many random elements in the evolution process of a genetic algorithm, the results from a genetic algorithm may be different for different instances of executions. In this section, the best route plan from five different executions of each route planning problem is used for flight path generation.

Table 6.2 Genetic algorithm parameters.

Genetic Algorithm Parameters	
Population Size	10
Maximum Iteration	400
Crossover Rate	0.85
Mutation Rate	0.10
No. of Executions	5

Figure 6.22 (a) to (c) show the optimal flight paths of a route planning problem of a fuel cell powered UAV with different heading algorithms, when the distances between the waypoints are far relative to the UAV turning radius. This represents a typical route planning problem in which the waypoint density is low. When the distances between the waypoints are far relative to the UAV turning radius, the transient fuel consumption cost is less significant as compared to the steady state fuel consumption cost. The minimum fuel route plan is dominated by the influence of the distances between the waypoints. For this reason, the influence of different heading algorithms on the resulting optimal route plans is insignificant. This can be observed in the optimal route plan shown in Figure 6.22 (a) to (c), where the sequences of waypoints from different heading algorithms are the same. Among the three optimal flight paths, the fuel consumption cost associated with the random heading algorithm is the minimum.

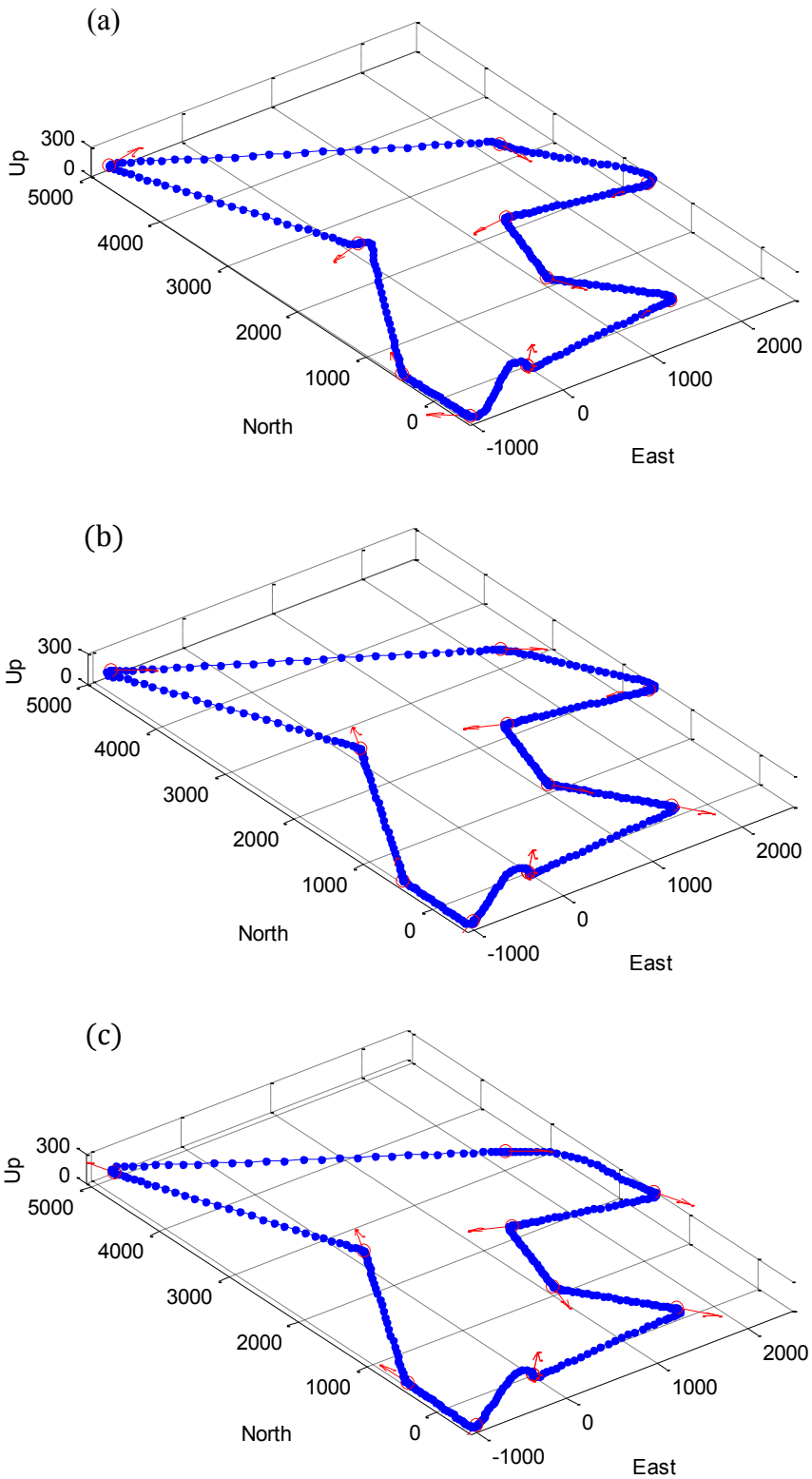

Figure 6.22 Example of a low waypoint density problem:
(a) Random heading algorithm, (b) Alternative heading algorithm, (c) Leg heading algorithm.

Figure 6.23 (a) to (c) show the optimal flight paths from different heading algorithms, in which the distances between the waypoints are short relative to the UAV turning radius. This represents a typical route planning problem in which the waypoint density is high. When the distances between the waypoints are short, the transient fuel consumption cost is significant as compared to steady state fuel consumption cost. The minimum fuel route plan is significantly influenced by the heading angles at the intermediate waypoints. The optimal route plans from the three heading algorithms shown in Figure 6.23 (a) to (c) are different in both the sequences of the waypoints and the heading angles at the intermediate waypoints. Similar to the low density waypoint example, the fuel consumption cost associated with the random heading algorithm is the minimum among the three heading algorithms.

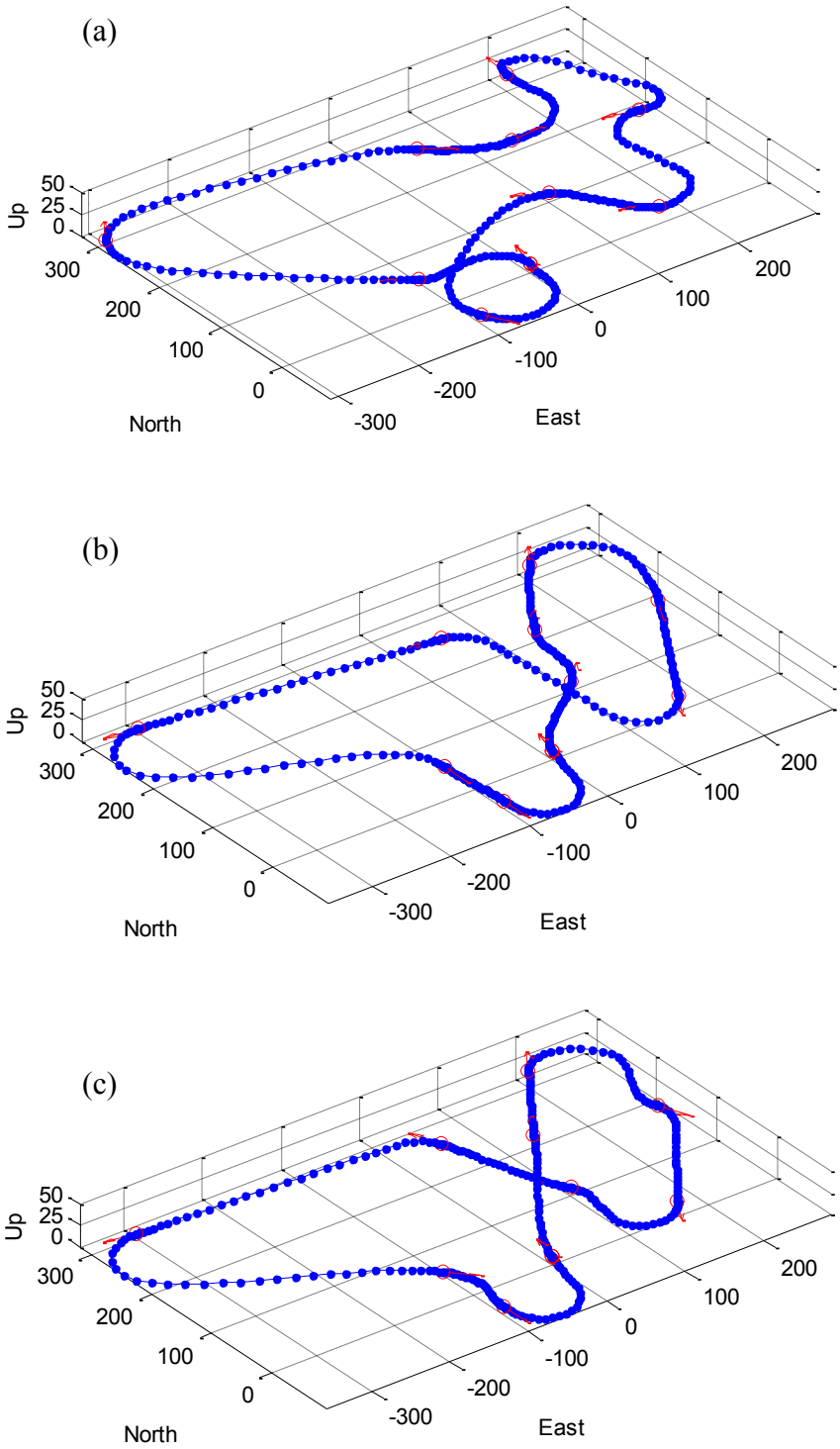

Figure 6.23 Example of a high waypoint density problem:
(a) Random heading algorithm, (b) Alternative heading algorithm, (c) Leg heading algorithm.

From the above examples, it can be concluded that for a low waypoint density route planning problem, the fuel consumption cost is dominated by the steady state fuel consumption cost and the resulting sequences of waypoints from different heading algorithms are likely to be the same. However, for a high waypoint density route planning problem, the transient fuel consumption cost is significant, which results different sequences of waypoints from different heading algorithms. The random heading algorithm minimizes the transient fuel consumption cost by a random search method. The alternative heading algorithm minimizes the transient fuel cost at the alternative segments. The leg heading algorithm minimizes the transient fuel cost at the end of each segment. With sufficient iterations, the fuel consumption cost associated with the route plan from the random heading algorithm is the minimum among the three heading methods.

6.6 Summary

Due to the specific fuel consumption curve of a fuel cell powered UAV, the minimum fuel point-to-point optimal trajectories are different from the minimum distance point-to-point optimal trajectories. To solve three-dimensional minimum fuel routing planning and path generation problems for a fuel cell powered UAV, this chapter proposed a new method, consisting of the development of a fuel consumption cost model, the implementation of a genetic algorithm with different heading algorithms, and the generation of optimal flight paths. The developed fuel consumption cost model for the minimum fuel point-to-point optimal trajectories included both the steady state fuel consumption cost and the transient fuel consumption cost. The minimum fuel route plan was optimized by a genetic algorithm with different heading algorithms. The minimum fuel flight path for a minimum fuel optimal route plan was generated by connecting the

waypoints with minimum fuel point-to-point optimal trajectories. As compared to the literature, this chapter extended the route planning problems from two dimensions to three dimensions. The optimization objective was extended from minimum distance to minimum fuel. The dynamic constraints were extended from the Dubins vehicle's dynamics to a three-dimensional point mass UAV model dynamics including the dynamics of a fuel cell powered UAV propulsion system.

CHAPTER 7

FUEL CELL SYSTEM SIZE OPTIMIZATION

7.1 Introduction

Design optimization is one of the keywords that frequently appear in the UAV literature, as the design of almost every single UAV and its sub-systems needs to be optimized to maximize the design objective and satisfy the design constraints. The design of a UAV involves many disciplinary areas, including aerodynamics, structure, and electronics, etc. Multidisciplinary Design Optimization (MDO) techniques are often applied to handle complex design optimization problems which involve many design variables. Examples of such optimization techniques applied to UAVs can be found in [119,120,121,122].

Several design optimization studies have been conducted to optimize certain performance aspects of a fuel cell powered UAV. In [123], qualitative assessment techniques were used to determine the class of vehicles that would benefit most from the fuel cell technology. In [124], an algorithmic approach was proposed to integrate the fuel cell system design environment to an aircraft sizing framework. In [25], a fuel cell powered UAV prototype was developed from a multidisciplinary design optimization that included the contribution analysis model of a fuel cell power plant. In [125], a validated multidisciplinary analysis was used to find the optimal design of both the UAV and the fuel cell propulsion system for a surveillance mission. Among all of the above design optimization studies, the contributions of various fuel cell system design parameters to the design objectives were studied in steady state flight conditions. However, in none of them was the influence of the transient performance of fuel cell systems included.

As highlighted in [1], a single type of UAV is often deployed for several different missions that require different flight trajectories. A UAV design that is optimal for one mission may not be optimal for another mission. In this chapter, the fuel cell system size parameters and the number of cells (N) and the cell area (A), are optimized with respect to a mission, where the mission is defined as a list of waypoints that a UAV needs to visit exactly once. The fuel cell system size optimization problem for a given mission is stated in Section 7.2, and an iterative method for finding the optimal fuel cell size for a given UAV mission is proposed in the same section. The building blocks of the proposed method are presented in Section 7.3. Example fuel cell system size optimization problems for missions with both high waypoint density and low waypoint density are solved with the proposed method in Section 7.4. It is observed that the optimal fuel cell sizes for different missions are different.

7.2 Problem Statement and Proposed Method

The efficiency of a fuel cell system improves as the system size increases. An increase in the fuel cell system size leads to an increase in the overall weight of a fuel cell powered UAV, which, in turn, increases the power consumption for a given UAV mission. There may be an optimal fuel cell system size for a given UAV mission. The fuel cell system size optimization problem with respect to a given mission is stated as follows.

For a given list of waypoints (whose route plan is to be optimized for minimum fuel consumption) and a given range of fuel cell system size parameters, the number of cells (N) and the cell area (A), what is the optimal fuel cell system size and the associated minimum fuel optimal route plan?

For a given list of waypoints, the total fuel consumption is a function of the fuel cell system size, and the sequence of the waypoints. The influence of the fuel cell system size parameters on the total fuel consumption is a continuous function. However, the influence of the sequence of waypoints is a discrete function. An optimization method for a continuous function cannot be used to optimize the sequence of the waypoints, and an optimization method for finding the optimal sequence of the waypoints is very inefficient for a continuous function. To optimize the fuel cell system size parameters with respect to a given mission, this chapter proposes an iterative method, which uses a genetic algorithm to find the optimal sequence of waypoints for a given fuel cell system size, and uses a nonlinear programming method to find the optimal fuel cell system size for a given sequence of waypoints.

The proposed method for the fuel cell system size optimization is shown in Figure 7.1. For a given fuel cell system, there is an optimal flight path angle for minimum fuel point-to-point trajectories. The minimum fuel optimal flight path angle (γ_{opt}) as a function of the number of cells (N) and the cell area (A) is empirically modeled as a quadratic function. With the optimal flight path angle determined, the database of the fuel consumption data as a function of the number of cells (N) and the cell area (A) at different flight path angles can be generated by trimming the dynamic equations of the fuel cell powered UAV. With an initial guess regarding the fuel cell system size, an optimal route plan is obtained by using the genetic algorithm presented in the previous chapter. For a given route plan, the optimal fuel cell system size is determined by using a nonlinear programming solver, where the fuel consumption cost is minimized within the given ranges of the design parameters. The optimal route plan for the optimal fuel cell

system size is obtained and compared with that from the previous iteration. If the optimal route plan for the optimal fuel cell system size in the current iteration is the same as that of the previous iteration, the iterative procedure stops, and both the optimal fuel cell system size and the optimal route plan are obtained.

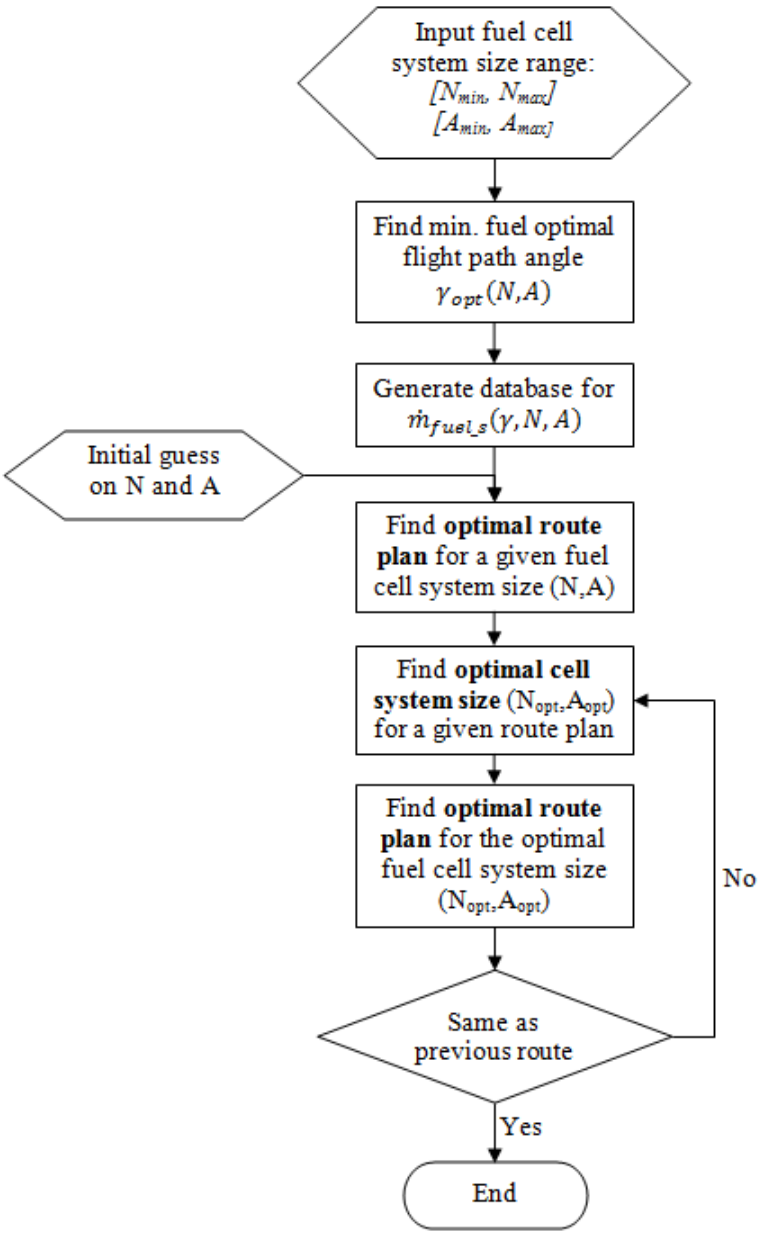

Figure 7.1 Proposed method for fuel cell system size optimization.

7.3 Fuel Cell System Size Optimization Building Blocks

7.3.1 Fuel Consumption Rate Database

The fuel consumption rate $\dot{m}_{fuel}(\gamma, N, A)$ is a function of the flight path angle, the number of cells, and the cell area, and trimming the UAV at any given flight path angle requires iterative procedure. In addition, both the genetic algorithm for route planning and the nonlinear programming method for fuel cell size optimization require iterative procedures. It is very inefficient to use one iterative procedure inside another iterative procedure. Hence, the database for the steady state fuel consumption rate, $\dot{m}_{fuel}(\gamma, N, A)$, at different fuel cell sizes (N and A) is required for fast computation of the steady state fuel consumption cost.

The study of the characteristics of the minimum fuel point-to-point optimal trajectories presented in Chapter 7 concludes that there is an optimal fight path angle for such flight trajectories for a given fuel cell powered UAV. If the straight line flight path angle from the initial position to the final position is more than the optimal flight path angle, the UAV will ascend with an S-shaped flight path to minimize the total fuel consumption cost. As shown in Figure 7.2, the optimal flight path angle is a function of the fuel cell system size, the number of cells (N) and the cell area (A), which can be modeled with a quadratic function, shown in Equation (7.1). The comparison between the optimal flight path angle obtained by trimming the UAV model and that calculated using Equation (7.1) is shown in Figure 7.2. The optimal flight path angles (γ_{opt}) determines the ranges of flight path angles to be trimmed to generate the fuel consumption database.

$$\gamma_{opt} = c_\gamma [1 \quad N \quad A \quad N*A \quad N^2 \quad A^2]^T \tag{7.1}$$

$$c_\gamma = \left[c_{\gamma_1}\, c_{\gamma_2}\, c_{\gamma_3}\, c_{\gamma_4}\, c_{\gamma_5}\, c_{\gamma_6}\right] \tag{7.2}$$

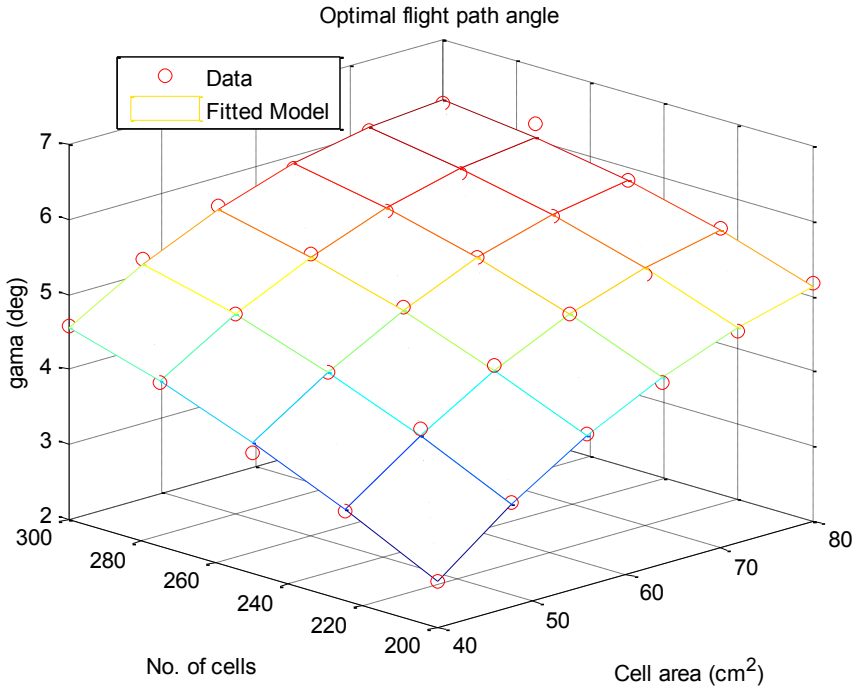

Figure 7.2 Optimal flight path angle as a function of fuel cell system size.

The database for the steady state fuel consumption rate, $\dot{m}_{fuel}(\gamma, N, A)$, at different fuel cell sizes (N and A) is generated by trimming the UAV model with different fuel cell system sizes at different flight path angles. Figure 7.3 shows fuel consumption rate with 48 cells and various cell areas at different flight path angles.

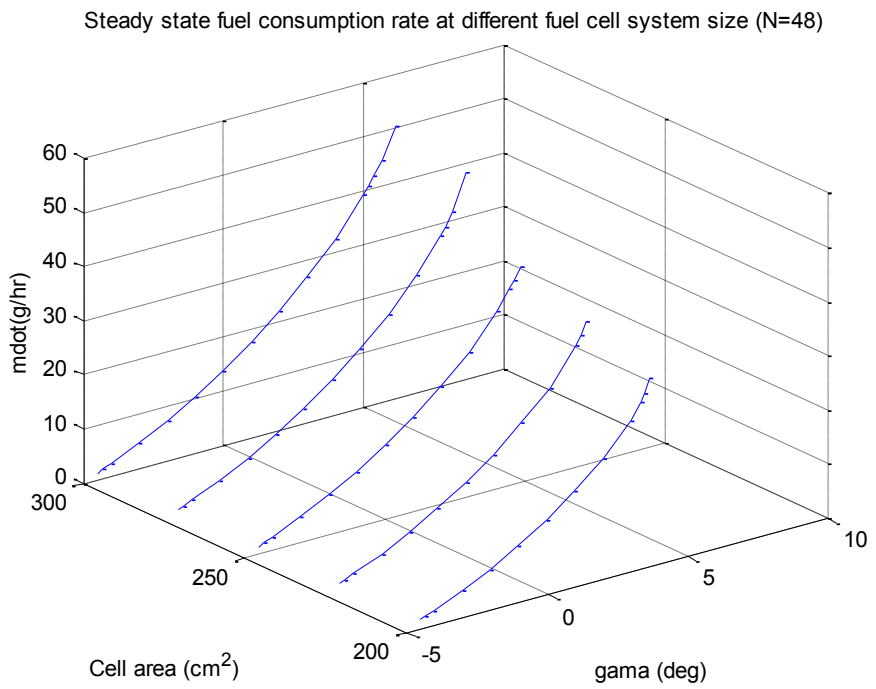

Figure 7.3 Fuel consumption rate database at N=48.

7.3.2 Optimal Fuel Cell System Size for a Given Route Plan

For a given route plan, which is a sequence of waypoints and heading angles at the intermediate waypoints, the total fuel consumption cost is calculated using the proposed cost model from the first segment to the last segment. Since the fuel consumption rate is a function of the number of cells (N) and the cell area (A), the total fuel consumption cost for a given route plan is also a function of the number of cells (N) and the cell area (A). For a given range of the design parameters (N and A), the optimal fuel cell size is found by using the following formulation, which is solved by using the SNOPT solver [70].

$$\begin{aligned} &\min_{N,A} \quad m_{fuel}(N,A) \\ &subject\ to \begin{pmatrix} N_{min} < N < N_{max} \\ A_{min} < A < A_{max} \end{pmatrix} \end{aligned} \tag{7.3}$$

7.4 Case Study on Fuel Cell System Size Optimization

In this section, fuel cell system size optimization problems for missions with both high waypoint density and low waypoint density are solved by using the proposed method shown in Figure 7.1. Since different missions have different optimal fight trajectories, the optimal fuel cell system size for one mission is expected to be different from that of another mission.

7.4.1 Example 1: A Low Waypoint Density Mission

The list of waypoints to be visited by a fuel cell powered UAV is shown in Figure 7.4, where the UAV is expected to start from the first waypoint at a given initial heading angle, and visit each of the remaining waypoints exactly once, and return to the first waypoint at a given final heading angle. The optimal route plan obtained using the genetic algorithm with the leg heading algorithm for the initial guessed fuel cell system size ($N = 48$, $A = 215\ \text{cm}^2$) is shown in Figure 7.5. The optimal fuel cell system size ($N_{opt} = 48$, $A_{opt} = 275\ \text{cm}^2$) is shown in Figure 7.6 together with complete fuel consumption cost map for the given range of fuel cell system size parameters. The optimal route plan for the optimal fuel cell size is shown in Figure 7.7, which is the same as the optimal route plan for the initial guessed fuel cell size. In addition, the minimum fuel optimal flight path is shown in Figure 7.8.

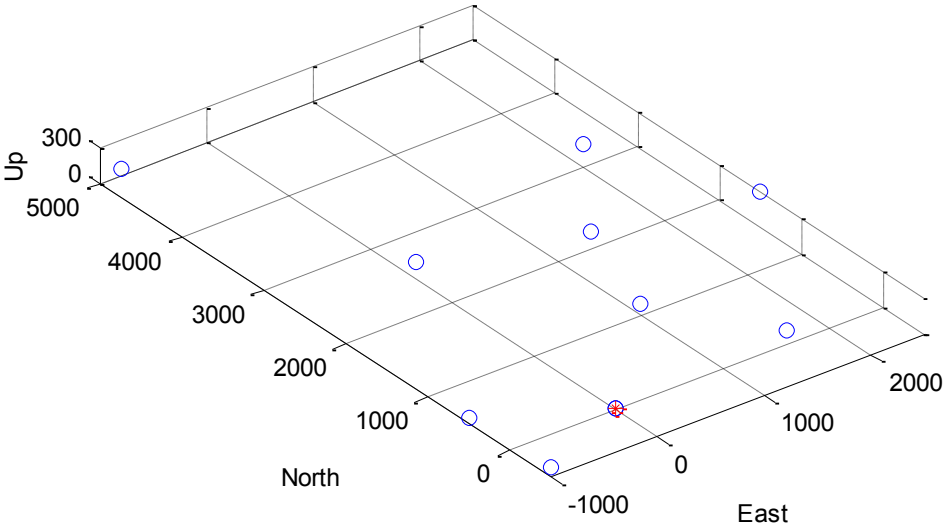

Figure 7.4 Fuel cell system size optimization for a low waypoint density mission: list of waypoints.

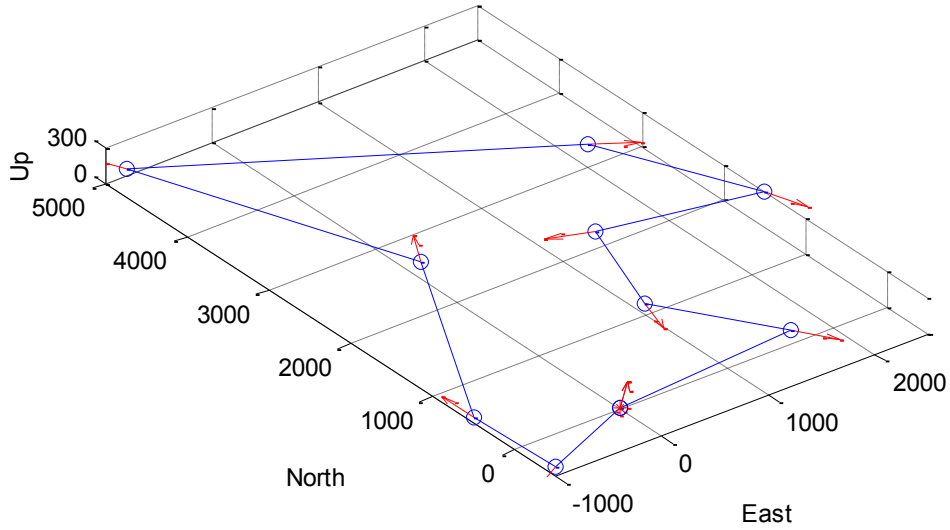

Figure 7.5 Fuel cell system size optimization for a low waypoint density mission: optimal mission plan with initial guess fuel cell system size.

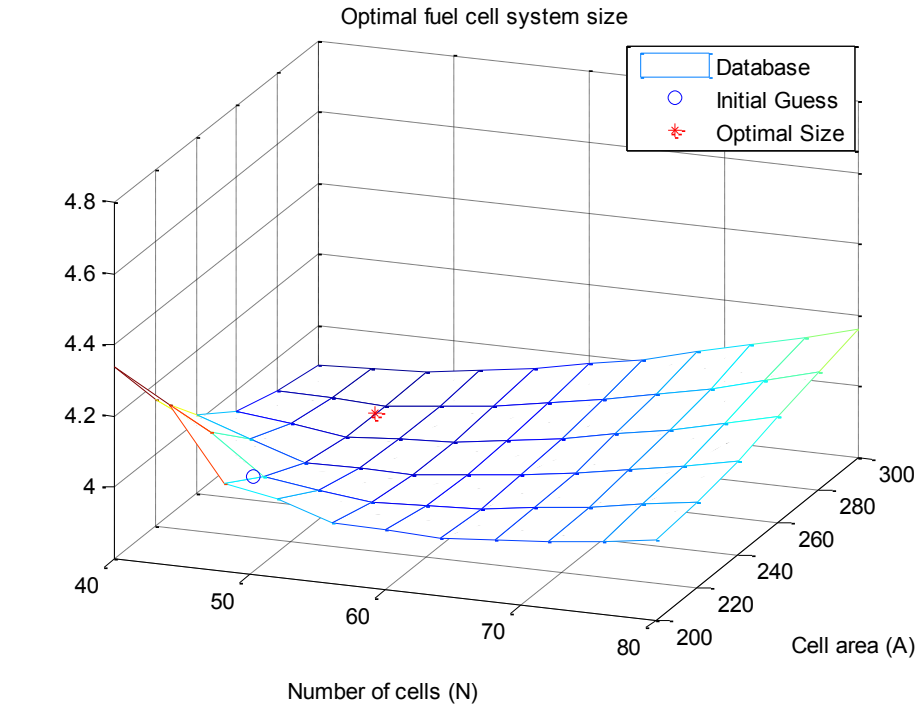

Figure 7.6 Fuel cell size optimization for a low waypoint density mission: optimal fuel cell system size.

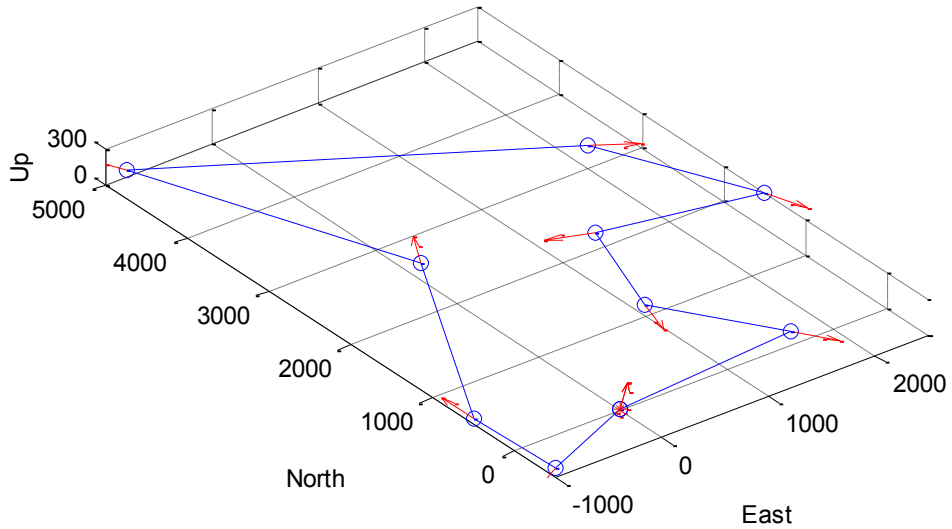

Figure 7.7 Fuel cell system size optimization for a low waypoint density mission: optimal mission plan with optimal fuel cell system size.

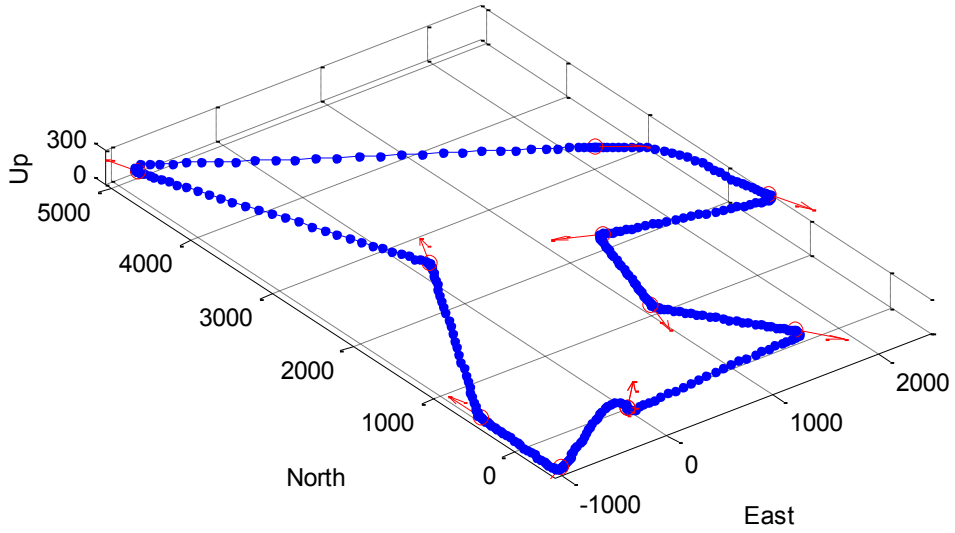

Figure 7.8 Fuel cell system size optimization for a low waypoint density mission: minimum fuel optimal flight path.

7.4.2 Example 2: A High Waypoint Density Mission

The list of waypoints for the fuel cell system size optimization problem for a high waypoint density mission is shown Figure 7.9. The optimal route plan obtained using the genetic algorithm with a leg heading algorithm for the initial guessed fuel cell system size ($N = 48$, $A = 215$ cm^2) is shown in Figure 7.10. The optimal fuel cell system size ($N_{opt} = 40$, $A_{opt} = 300$ cm^2) is shown in Figure 7.11 together with a complete fuel consumption cost map for the given range of fuel cell system size parameters. The optimal route plan for the optimal fuel cell size is shown in Figure 7.12, which is the same as the optimal route plan for the initial guessed fuel cell size. The minimum fuel optimal flight path for the optimal route plan is shown in Figure 7.13.

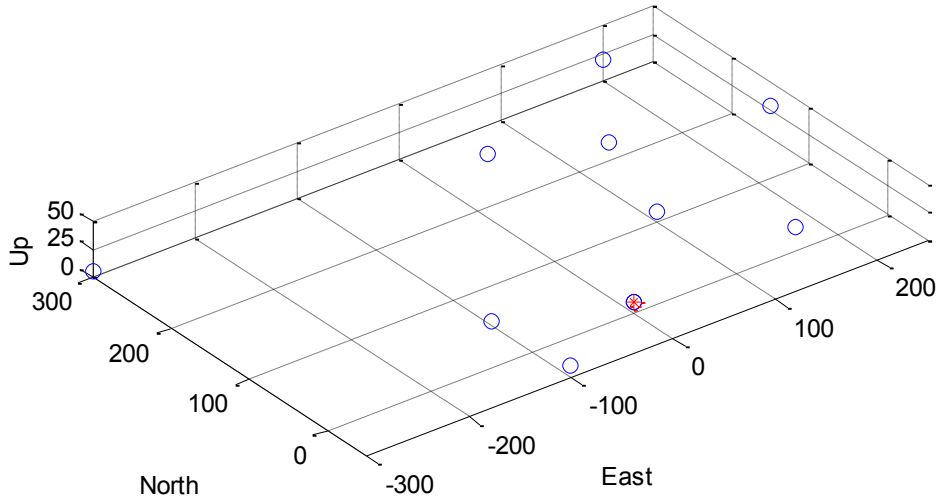

Figure 7.9 Fuel cell system size optimization for a high waypoint density mission: list of waypoints.

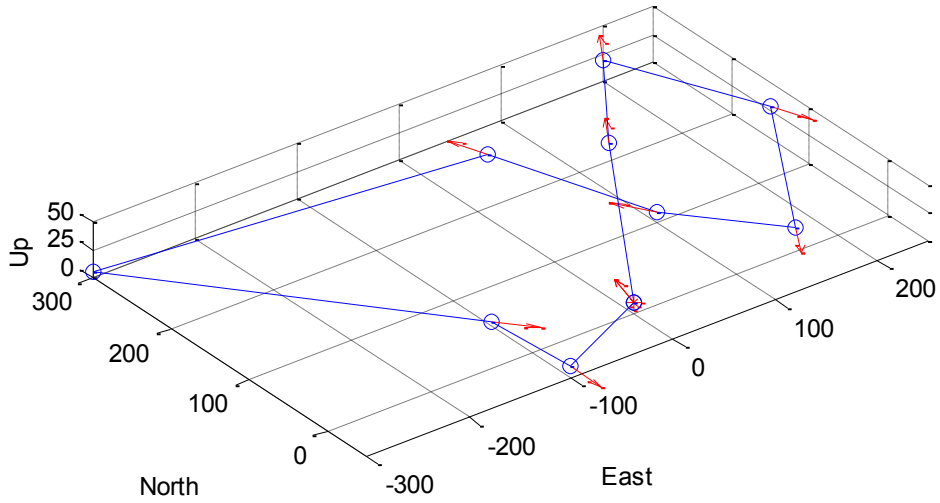

Figure 7.10 Fuel cell system size optimization for a high waypoint density mission: optimal mission plan with initial guess fuel cell system size.

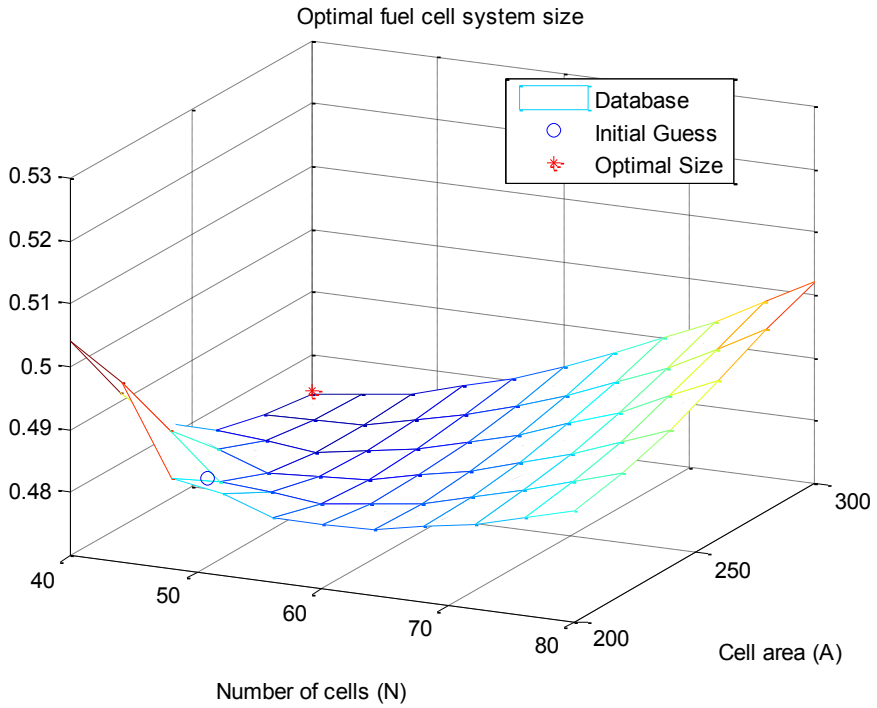

Figure 7.11 Fuel cell size optimization for a high waypoint density mission: optimal fuel cell system size.

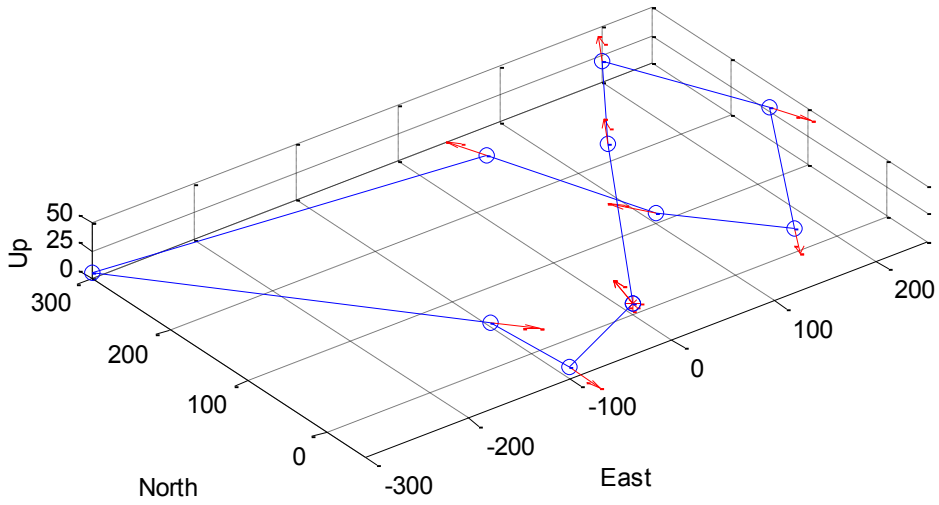

Figure 7.12 Fuel cell system size optimization for a low waypoint density mission: optimal mission plan with optimal fuel cell system size.

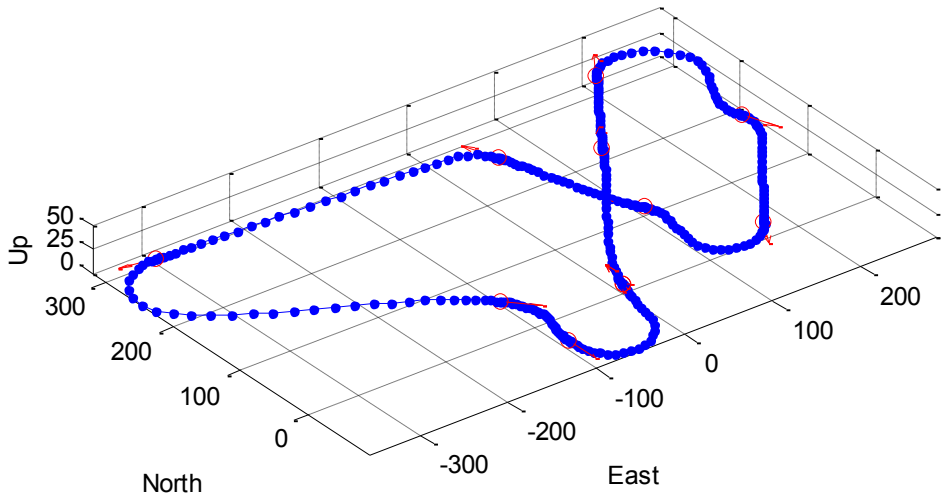

Figure 7.13 Fuel cell system size optimization for a low waypoint density mission: minimum fuel optimal flight path.

From these two examples, it is observed that the optimal fuel cell system size for different missions is different. In addition, the fuel cell system size does not seem to influence the optimal route plan for a given list of waypoints. As shown in Figure 7.3, for different fuel cell system sizes, the trend of the fuel consumption curves is the same in that the fuel consumption rate increases monotonically with the flight path angle. A flight trajectory that is fuel optimal for one fuel system size is also optimal for another fuel cell system size.

7.5 Summary

In this chapter, an iterative method was proposed to find the optimal fuel cell system size for a given mission, which was defined as a list of waypoints that a UAV needed to visit. With the proposed method, both the fuel cell system size and the route plan were optimized for a given mission. Through examples, it was demonstrated that there are different optimal fuel cell system sizes for different missions. Since the optimal route

plan for one fuel cell system size was also optimal for another fuel cell system size, the optimal fuel cell system size for a given mission was found after only one iteration.

CHAPTER 8

CONCLUSIONS, CONTRIBUTIONS AND RECOMMENDATIONS

8.1 Conclusions

This dissertation has extensively investigated research questions related to trajectory optimization problems for fuel cell powered UAVs considering the fuel cell system dynamics. A dynamic model for a fuel cell powered UAV propulsion system has been developed to understand the influence of the fuel cell system dynamics on the dynamic behavior of a fuel cell powered UAV. This model has been also used as the dynamic constraints of trajectory optimization problems to study the characteristics of the optimal trajectories. Based on the characteristics of the minimum fuel point-to-point optimal trajectories of a fuel cell powered UAV, a method has been proposed to solve the three-dimensional minimum fuel route planning and path generation problems, and the obtained flight paths are both fuel optimal and dynamically feasible. Finally, an iterative method has been proposed to find the optimal fuel cell system size for any given mission. Through examples, it has been observed that the optimal fuel cell system sizes for different UAV missions will vary.

The conclusions drawn from the studies presented in this dissertation are given as follows:

1) In a fuel cell powered UAV propulsion system, the fuel cell delay effect from the fuel cell system causes additional delay in the propeller rotational speed. Among different fuel cell system parameters, the fuel cell delay time constant has the most significant influence on the effect time

constants and the step command responses of a fuel cell powered UAV propulsion system.

2) The maximum speed and maximum rate of climb of a fuel cell powered UAV are inferior to those of a conventional gas powered UAV with the same gross weight and airframe. This is due to the lower power density of a fuel cell system as compared to that of a conventional reciprocating engine. The absolute fuel consumption rate of a fuel cell powered UAV is significantly lower than that of a conventional gas powered UAV. This means the flight endurance of a fuel cell powered UAV can be extended easily with only a very small increase in the gross weight.

3) Different pseudospectral methods based on different sets of collocation points can be generalized as one framework, despite differences in the collocation points. With the proposed generalized framework, many new pseudospectral methods based on new sets of collocation points can be more easily evaluated.

4) The optimal flight path angles of the minimum time and minimum distance point-to-point optimal trajectories are constrained by the maximum available power for both the conventional gas powered UAV configuration and the fuel cell powered UAV configuration. However, the optimal flight path angles of the minimum fuel point-to-point optimal trajectories are not determined by the maximum available power for the fuel cell powered UAV configuration.

5) For conventional gas powered UAVs, minimum distance, minimum time, and minimum fuel point-to-point optimal trajectories are similar. However, the minimum fuel optimal trajectories of a fuel cell powered UAV are different from the minimum time and minimum fuel point-to-point optimal trajectories. Simplified minimum distance route planning methods based on the Dubins vehicle cannot generate a minimum fuel optimal route plan and flight path for a fuel cell powered UAVs. However, the method proposed in this dissertation is able to find the optimal route plan and flight path that are both dynamically feasible and fuel optimal for fuel cell powered UAVs.

6) In a route planning and path generation problem, the heading angles at the intermediate waypoints influence only the transient fuel consumption cost. The optimal route plans obtained by using different heading algorithms for a high waypoint density problem are different in both the sequence of the waypoints and the heading angles at the intermediate waypoints. However, for a low waypoint density problem, the sequences of waypoints of the optimal route plans obtained by using different heading algorithms are likely the same. Among the fuel consumption costs of the optimal flight paths from different heading algorithms, the one from the random heading algorithm is minimal.

7) The influence of fuel cell system size parameters (the number of cells and the cell area) on the fuel consumption cost of a minimum fuel point-to-point optimal trajectory is significant. The influence of other design

parameters on the fuel consumption cost is insignificant. With the proposed method for fuel cell system size optimization with respect to a mission, the impacts of both the steady state performance and the transient performance of the fuel cell system can be brought to the mission level. It is expected that the optimal fuel cell system sizes for different missions will be different.

8.2 Summary of Contributions

While investigating the research questions related to the trajectory optimization problems for fuel cell powered UAVs, the current research has made several original contributions to the literature. These contributions are summarized as follows:

1) A dynamic model of a fuel cell powered UAV propulsion system

This research develops a dynamic model of a fuel cell powered UAV propulsion system by combining the dynamic model of a fuel cell system, the dynamic model of an electric motor and the performance model of a propeller. Although each element in the developed model is not new, the overall developed model for a fuel cell powered UAV propulsion system is the first of its kind in the literature. This model can be used for different applications. It can be used to conduct transient response analysis, as a linearized model for control synthesis, and as a comprehensive simulation model, etc.

2) *A generalized framework for pseudospectral methods*

The generalized framework for pseudospectral methods proposed in this dissertation transcribes an optimal control problem to a nonlinear programming (NLP) optimization problem with any set of collocation points. Different from other unified frameworks in the literature, the proposed framework generalizes all four pseudospectral methods, the Legendre pseudospectral method, the Chebyshev pseudospectral method, the Gauss pseudospectral method, and the Radau pseudospectral method, with one set of transcription equations. With the proposed framework, different pseudospectral methods can be compared with the same NLP solver. This feature is important as optimal control solvers available in the literature are often in the form of paired packages of one pseudospectral method and one NLP solver. It is difficult to compare two pseudospectral methods with two different NLP solvers. In addition, with the proposed framework, a pseudospectral method with a new set of collocation points can be readily evaluated.

3) *A method for 3-D minimum fuel route planning and path generation*

Route planning problems for UAVs in the literature are often formulated as minimum distance problems subject to the path curvature constraint of a UAV. In a three-dimensional minimum fuel route planning and path generation problem, the effects of both the dynamic constraints and the fuel consumption cost on the optimal route plan are embedded in the problem formulation. With the cost model extracted from the minimum

fuel point-to-point optimal trajectories, the proposed method successfully utilized the trajectory optimization results to the route planning process. As a trajectory optimization problem can be formulated with different dynamic constraints and different performance index functions, the proposed method can be extended to route planning and path generation problems to different UAVs or different objectives.

4) A method for propulsion system size optimization with respect to mission

The design optimization method presented here, with respect to a given mission, and considering both the steady state cost and the transient cost, is the first in the literature. With the proposed method, the impacts of the propulsion system design parameters are brought to the mission level. This design optimization method is important in that a single UAV is often used in many different missions, and the optimal trajectories of different missions are usually different. As the proposed method for propulsion system optimization is developed by extracting the results from trajectory optimization analysis, design optimization with respect to missions with different performance measures can be handled by using the proposed method with different trajectory optimization analyses.

8.3 Recommendations for Future Work

Although the research problems around the trajectory optimizations for fuel cell powered UAVs were studied extensively in this dissertation, there are several extensions that

could be applied to the models, methods, or problems presented... The recommendations for future work are listed as follows.

1) *Validation of the transient parameters of the dynamic model of a fuel cell powered UAV propulsion system*

The dynamic model of a fuel cell powered UAV propulsion system derived in this dissertation models both the steady state performance and transient performance. In this dissertation, the steady state parameters were validated against the manufacturer's data. The transient parameters were referenced from similar systems from the literature. The validation of the transient parameters against experimental data would certainly increase the confidence level of the derived model. In addition, transient experimental data can also be used to validate the study on the transient characteristics of a fuel cell powered UAV propulsion system.

2) *Extension to real-time route planning and path generation*

In the proposed method for three-dimensional route planning and path generation problems discussed in this dissertation, a genetic algorithm was implemented with different heading algorithms to find the optimal route plan, and the optimal flight path was generated using the trajectory optimization method. The cost estimation of a given route plan with the derived cost model is not computationally expensive. A genetic algorithm modified with smaller number of iterations may be able to meet the real-time requirement. The most computationally expensive and time consuming process in the proposed method is the flight path generation

with optimal trajectories, where the dynamic equations of a fuel cell powered UAV propulsion system and the point mass UAV model are formulated as dynamic constraints. These ten dynamic constraint equations are the main barriers for path generation in real-time. However, these equations are required to ensure that the flight paths generated are both dynamically feasible and fuel optimal. If the desired optimal flight path can be generated directly without solving the trajectory optimization problems, the route planning and path generation process can be extended to real-time applications.

3) Extension to terrain collision avoidance

The proposed method for route planning and path generation, and the proposed method for fuel cell system size optimization are based on the fuel consumption cost model of the minimum fuel point-to-point optimal trajectories in a collision free environment. This certainly limits the capability of the proposed model. Including appropriate path constraints with respect to a terrain database can extend the trajectory optimization problems to terrain collision avoidance. If the characterization of such optimal trajectories can be obtained, the proposed method can then be extended to terrain collision avoidance, which can be used to address more practical practical path planning problems.

4) Extension to fuel cell system size optimization for multiple missions

The case study on fuel cell system size optimization has concluded that the optimal fuel cell system sizes for different missions are different.

However, it may not be possible to optimize the fuel cell system size for every mission. One of the alternative options is to find the optimal fuel cell system size with respect to multiple missions. In this dissertation, UAV routes are optimized by a genetic algorithm, in which the route plan is represented by a sequence of numbers. Such integer representation of waypoints can be extended to multiple missions. Special crossover and mutation operators, considering the routing constraints for multiple missions, can be used to generate the optimal route plan for multiple missions. In such way, the proposed iterative method for fuel cell system size optimization can be extended to multiple missions.

REFERENCES

[1] "Unmanned Aircraft Systems Roadmap 2005-2030," Office of the Secretary of Defense, 2005.

[2] Andrew Dicks James Larminie, *Fuel Cell Systems Explained*, Second Edition ed. Chichester, UK: John Wiley & Sons Ltd, 2003.

[3] Bei Gou, Woon Ki Na, and Bill Diong, *Fuel Cells - Modeling, Control, and Applications*. Boca Raton, FL: CRC Press, 2009.

[4] Frano Barbir, *PEM Fuel Cells: Theory and Practice*. London: Elsevier Academic Press, 2005.

[5] Suddhasatwa Basu, *Recent Trends in Fuel Cell Science and Technology*. New Delhi, India: Anamaya Publishers, 2007.

[6] Kar Kordesch and Gunter Simade, *Fuel Cells and Their Application*. New York: Weinheim, 1996.

[7] Colleen Spiegel, *PEM Fuel Cell - Modeling and Simulation Using MATLAB*. London, UK: Academic Press, 2008.

[8] Suddhasatwa Basu, *Recent Trend in Fuel Cell Science and Technology*. New York: Springer, 2007.

[9] Chrysler Ecovoyager. [Online]. http://www.chrysler.com/en/autoshow/concept_vehicles/ecovoyager/

[10] Honda FCX Clarity Specifications. [Online]. http://automobiles.honda.com/fcx-clarity/specifications.aspx

[11] Michael A. Dornheim, "Fuel Cells Debut," *Aviation Week & Space Technology*, vol. 158, no. 22, 6/2/2003.

[12] UAS Advanced Development: Hornet. [Online]. http://www.avinc.com/uas/adc/hornet/

[13] (2008, March) AeroVironment Puma Small UAS Achieves Record Flight of Over Nine Hours Using Fuel Cell Battery Hybrid System. [Online]. http://www.avinc.com/resources/press_release/aerovironment_puma_small_uas_achieves_record_flight

[14] (2009, August) Worlds First Commercial Fuel Cell Unmanned Aerial System. [Online]. http://www.gizmag.com/worlds-first-commercial-fuel-cell-unmanned-aerial-system/12453/

[15] (2010, August) IAI Malat Equips Bird Eye 650 Unmanned Aircraft with Horizon's AEROPAK Fuel Cell System. [Online]. http://eon.businesswire.com/news/eon/20100823005559/en/Aeropak/Bird-Eye-650/Horizon-Energy-Systems

[16] (2009, November) NRL's Ion Tiger Sets 26-Hour Flight Endurance Record. [Online]. http://www.nrl.navy.mil/media/news-releases/2009/nrls-ion-tiger-sets-26hour-flight-endurance-record

[17] (2011, November) EnergyOr Demonstrates Fuel Cell Technology with Defence Research & Development Canada (DRDC). [Online]. http://www.energyor.com/energyor/news.cfm

[18] J. W. Youngblood, T. A. Talay, and R. J. Pegg, "Design of Long-Endurance Unmanned Airplanes Incorporating Solar and Fuel Cell Propulsion," in *AIAA/SAE/ASME 20th Joint Propulsion Conference*, Cincinnati, Ohio, June 11-13, 1984.

[19] Jeffrey J. Berton, Joshua E. Freeh, and Timothy J. Wickenheiser, "An Analytical Performance Assessment of a Fuel Cell-Powered, Small Electric Airplane," in *Novel Vehicle Concepts and Emerging Vehicle Technologies Symposium*, Brussels, Belgium, April 7–10, 2003.

[20] Michael G. Friend and David L. Daggett, "Fuel Cell Demonstrator Airplane," in *AIAA/ICAS International Air and Space Symposium and Exposition*, Dayton, Ohio, 14-17 July 2003.

[21] Tom Koehler. (2008, May) Boeing makes history with flights of Fuel Cell Demonstrator Airplane. [Online]. http://www.boeing.com/news/frontiers/archive/2008/may/ts_sf04.pdf

[22] Thomas H. Bradley and David E. Parekh, "Comparison of Design Methods for Fuel-Cell-Powered Unmanned Aerial Vehicles," *Journal of Aircraft*, vol. 46, no. 6, pp. 1945-1956, 2009.

[23] Thomas H. Bradley, Blake A. Moffitt, Thomas F. Fuller, Dimitri Mavris, and David E. Parekh, "Design Studies for Hydrogen Fuel Cell Powered Unmanned Aerial Vehicles," in *26th AIAA Applied Aerodynamics Conference*, Honolulu, Hawaii, 18 - 21 August 2008.

[24] Blake A. Moffitt, Thomas H. Bradley, Dimitri Mavris, and David E. Parekh, "Reducing Uncertainty of a Fuel Cell UAV through Variable Fidelity Optimization," in *7th AIAA Aviation Technology, Integration and Operations Conference*, Belfast, Northern Ireland, 18 - 20 September 2007.

[25] Thomas Heenan Bradley, "Modeling, Design and Energy Management of Fuel Cell Systems for Aircraft," Georgia Institute of Technology, Atlanta, GA, PhD Thesis December, 2008.

[26] Lakmal Karunarathne, John T. Economou, and Kevin Knowles, "Model based power and energy management system for PEM fuel cell/ Li-Ion battery driven propulsion system," in *5th IET International Conference on Power Electronics, Machines and Drives (PEMD 2010)*, Brighton, UK, 19-21 April 2010.

[27] Thomas H. Bradley, Blake A. Moffitt, David E. Parekh, Thomas F. Fuller, and

Dimitri N. Mavris, "Energy Management for Fuel Cell Powered Hybrid-Electric Aircraft," in *7th International Energy Conversion Engineering Conference*, Denver, 2009.

[28] Gottfried Sachs and Theodoros Christodoulou, "Reducing Fuel Consumption of Subsonic Aircraft by Optimal Cyclic Cruise," *Journal of Aircraft*, vol. 24, no. 9, pp. 616-622, 1987.

[29] Masanori Harada and Kevin Bollino, "Minimum Fuel Circling Flight for Unmanned Aerial Vehicles in a Constant Wind," in *AIAA Guidance, Navigation and Control Conference and Exhibit*, Honolulu, Hawaii, 2008.

[30] Dawn M. Bernardi and Mark W. Verbrugge, "A Mathematical Model of the Solid-Polymer-Electrolyte Fuel Cell," *Journal of The Electrochemical Society*, vol. 139, no. 9, pp. 2477-2491, 1992.

[31] Denver Cheddie and Norman Munroe, "Review and Comparison of Approaches to Proton Exchange Membrane Fuel Cell Modeling," *Journal of Power Sources*, vol. 147, no. 1, pp. 72-84, 2005.

[32] F. Standaert, K. Hemmes, and N. Woudstra, "Analytical Fuel Cell Modeling," *Journal of Power Sources*, vol. 63, pp. 221-234, 1996.

[33] W.Q. Tao et al., "Parameter Sensitivity Examination and Discussion of PEM Fuel Cell Simulation Model Validation Part I. Current Status of Modeling Research and Model Development," *Journal of Power Sources*, vol. 160, no. 1, pp. 359-373, 2006.

[34] Wei-Mon Yan, Hui-Chung Liu, Chyi-Yeou Soong, Falin Chen, and C.H. Cheng, "Numerical study on cell performance and local transport phenomena of PEM fuel cells with novel flow field designs," *Journal of Power Sources*, vol. 161, no. 2, pp. 907-919, 2006.

[35] Phong Thanh Nguyen, "A Three-Dimensional Computational Model of PEM Fuel Cell with Serpentine Gas Channels," University of Victoria, Victoria, Canada, Master Thesis 2001.

[36] Junbom Kim, Seong-Min Lee, Supramaniam Srinivasan, and Charles E. Chamberlin, "Modeling of Proton Exchange Membrane Fuel Cell Performance with an Empirical Equation," *Journal of Electrochemical Society*, vol. 142, no. 8, p. 2670, 1995.

[37] Caisheng Wang, M. Hashem Nehrir, and Steven R. Shaw, "Dynamic Models and Model Validation for PEM Fuel Cells Using Electrical Circuits," *IEEE Transactions on Energy Conversion*, vol. 20, no. 2, pp. 442-451, 2005.

[38] Haijiang Wang, Xiao-Zi YUan, and Hui Li, *PEM Fuel Cell Diagnostic Tools*. Boca Raton, FL: Taylor & Francis Group, LLC, 2012.

[39] Hua Jianfeng, Xu Liangfei, Lin Xinfan, Lu Languang, and Ouyang Minggao,

"Modeling and Experimental Study of PEM Fuel Cell Transient Response for Automotive Applications," *Tsinghua Science and Technology*, vol. 14, no. 5, pp. 639-645, October 2009.

[40] K. P. Adzakpa et al., "PEM Fuel Cells Modeling and Analysis Through Current and Voltage Transient Behaviors," *IEEE Transactions on Energy Conversion*, vol. 23, no. 2, pp. 581-591, June 2008.

[41] J.B. Jia, Y.T. Cham, Y. Wang, and Frank Lewis, "The Electrical Dynamic Response Study of PEMFC as a Backup Power Supply," in *2007 IEEE International Conference on Control and Automation*, Guangzhou, CHINA, May 30 - June 1, 2007.

[42] Laurent Dumercy, Raynal Glises, Jean-Marie Kauffmann, and Hasna Kouahlis-Galous, "Transient Thermal Computation of a PEM Fuel Cell by a Nodal Modeling," in *Vehicular Technology Conference, 2003. VTC 2003-Fall. 2003 IEEE 58th , vol.5*, 6-9 Oct. 2003.

[43] Li Fang, Li Di, and Yang Ru, "A Dynamic Model of PEM Fuel Cell Stack System for Real Time Simulation," in *2009 Asia-Pacific Power and Energy Engineering Conference*, Wuhan, China, 27-31 March 2009.

[44] Wolfgang Friede, Stéphane Raël, and Bernard Davat, "Mathematical Model and Characterization of the Transient Behavior of a PEM Fuel Cell," *IEEE Transactions on Power Electronics*, vol. 19, no. 5, pp. 1234-1241, September 2004.

[45] Benoit C. Chachuat, *Nonlinear and Dynamic Optimization - From Theory to Practice*.: Laboratoire d'Automatique, Ecole Polytechnique Federale de Lausanne, 2006/2007.

[46] Tamer Inanc, Kathy Misovec, and Richard M. Murray, "Nonlinear Trajectory Generation for Unmanned Air Vehicles with Multiple Radars," in *43rd IEEE Conference on Decision and Control*, Atlantis, Paradise Island, Bahamas, Dec 14-17, 2004.

[47] Reid A. Larson, Mark J. Mears, and Paul A. Blue, "Path Planning for Unmanned Air Vehicles to Goal States in Operational Environmen," in *AIAA's 4th Infotech@Aerospace Conference*, Arlington, VA, 26 - 29 September, 2005.

[48] Brian R. Geiger, Joseph F. Horn, Anthony M. DeLullo, and Lyle N. Long, and Albert F. Niessner, "Optimal Path Planning of UAVs Using Direct Collocation with Nonlinear Programming," in *AIAA Guidance, Navigation, and Control Conference and Exhibit*, Keystone, Colorado, 21 - 24 August, 2006.

[49] Yiyuan J. Zhao, "Extracting Energy from Downdraft to Enhance Endurance of Uninhabited Aerial Vehicles," *Journal of Guidance, Control and Dynamics*, vol. 32, no. 4, pp. 1124-1133, July–August 2009.

[50] Robert H. Chen and Jason L. Speyer, "Improved Endurance of Optimal Periodic

Flight," *Journal of Guidance, Control and Dynamics*, vol. 30, no. 4, pp. 1123-1133, July–August 2007.

[51] Branden J. Rademacher, Ping Lu, Alan L. Strahan, and Christopher J. Cerimele, "In-Flight Trajectory Planning and Guidance for Autonomous Parafoils," *Journal of Guidance, Control and Dynamics*, vol. 32, no. 6, pp. 1697-1712, November–December 2009.

[52] Marianne Jacobsen and Ulf T. Ringertz, "Airspace Constraints in Aircraft Emission Trajectory Optimization," *Journal of Aircraft*, vol. 47, no. 4, pp. 1256-1265, July–August 2010.

[53] Maya Dekel K. and Joseph Z. Ben-Asher, "Pseudo-Spectral-Method Based Optimal Glide in the Event of Engine Cut-off," in *AIAA Guidance, Navigation, and Control Conference*, Portland, Oregon, 08 - 11 August 2011.

[54] Elisa Capello, Giorgio Guglieri, Fulvia Quagliotti, and Gianluca Speciale, "Trajectory Optimisation for Autonomous Vehicles: A MiniUAV Application," in *The 26th International Congress of the Internaltioinal Council of the Aeronautical Sciences*, Anchorage, Alaska, USA, 14 - 19 September, 2008.

[55] John T. Betts, "Survey of Numerical Methods for Trajectory Optimization," *Journal of Guidance*, vol. 21, no. 2, March-April 1998.

[56] D. G. Hull, *Optimal Control Theory for Applications*. New York: Springer-Verlag, 2003.

[57] D. Benson, "A Gauss Pseudospectral Transcription for Optimal Control," PhD Thesis February 2005.

[58] D. G. Hull, "Conversion of Optimal Control Problems into Parameter Optimization Problems," *Journal of Guidance, Control and Dynamics,* vol. 20, no. 1, January-February 1997.

[59] B.A. Finlayson, *The Method of Weighted Residuals and Variational Principles: With Application in Fluid Mechanics, Heat and Mass Transfer*. New York: Academic Press, 1972.

[60] B. Fornberg, *A Practical Guide to Pseudospectral Methods*. Cambridge: Cambridge University Press, 1996.

[61] F. Fahroo and I. M. Ross, "Direct Trajectory Optimization by a Chebyshev Pseudospectral Method," *Journal of Guidance, Control and Dynamics*, vol. 25, no. 1, January-February 2002.

[62] G. Elnagar, M.A. Kazemi, and M. and Razzaghi, "The Pseudospectral Legendre Method for Discretizating Optimal Control Problems," *IEEE Transactions on Automatic Control*, vol. 40, no. 10, October 1995.

[63] D Grag, "Advances in Global Pseudospectral Methods for Optimal Control,"

University of Florida, PhD Thesis August 2011.

[64] I. M. Ross and F. Fahroo, "Convergence of Pseudospectral Discretizations of Optimal Control Problems," in *Proceedings of the 40th IEEE Conference on Decision and Control*, Orlando, Florida, December 2001.

[65] Victor M. Becerra. (2011, July) PSOPT Optimal Control Solver User Manual. [Online]. http://www.psopt.org/home

[66] Anil V. Rao and David Benson, "User's Manual for GPOPS Version 4.x," University of Florida, User's Manual August 2011.

[67] DIDO Optimal Control Software: Get Reuslts Fast and Easy. [Online]. http://www.elissarglobal.com/industry/products/software-3/

[68] Boeing Research & Technology - Sparse Optimal Control Software (SOCS). [Online]. http://www.boeing.com/phantom/socs/capabilities.html

[69] Introduction to IPOPT: A tutorial for downloading, installing, and using IPOPT. [Online]. http://www.coin-or.org/Ipopt/documentation/

[70] F. E Gill, "User's Guide for SNOPT Version 7: Software for Large-Scale Nonlinear Programming," June 2008.

[71] AXI, "AXI Products Catologue," Product Catalogue 2012.

[72] Wei-Mon Yan, Chyi-Yeou Soong, Falin Chen, and Hsin-Sen Chu, "Transient Analysis of Reatant Gas Transport and Performance of PEM Fuel Cells," *Journal of Power Sources*, vol. 143, pp. 48-56, 2005.

[73] Padmraja Yedamale, "Brushless DC (BLDC) Motor Fundamentals," Microchip Technology Inc., Application Notes 2003.

[74] Ward Brown, "Brushless DC Motor Control Made Easy," Microchip Technology Inc., Application Notes 2002.

[75] Quentin R. Wald, "The Aerodynamics of Propellers," *Progress in Aerospace Sciences*, vol. 42, no. 1, pp. 85-128, 2006.

[76] George De Bothezat, "The General Theory of Blade Screws," Technical Report 1919.

[77] Sydney Goldstein, *On the Vortex Theory of Screw Propeller*. St. Jonh's College, Cambridge, 1929.

[78] Hans Reisener, "A Generalized Vortex Theory of the Screw Propeller and its Application," Armour Institute of Technology, Washington, Technical Notes 1940.

[79] (2012, Oct) Aerosonde Product Development History. [Online]. http://www.aerosonde.com/products/product_dev_history.html

[80] Unmanned Dynamics, LLC, "Aerosim Blockset Version 1.2 Uer's Guide," Unmanned Dynamics, LLC, Hood River, OR, User Guide.

[81] (2012, Oct) Horizon Fuel Cell Technology - Fuel Cells. [Online]. http://www.horizonfuelcell.com/fuel_cell_stacks.htm

[82] "Open-Cathode PEM Fuel Cells," Singapore, 2012.

[83] Karen E. Swider-Lyons et al., "Hydrogen Fuel Cell Propulsion for Long Endurance Small UAVs," in *AIAA Centennial of Naval Aviation Forum "100 Years of Achievement and Progress"*, Virginia Beach, VA, 21-22 September, 2011.

[84] Stephen P. Hendrickson, "A Miniature Powerplant for Very Small, Very Long Range Autonomous Aircraft," The Insitu Group Inc., Bingen, Washington, Technical Report 1999.

[85] J. Vlassenbroeck and R. Van Doreen, "A Chebyshev Technique for Solving Nonlinear Optimal Control Problems," *IEEE Tranactions on Automatic Control*, vol. 33, no. 4, pp. 33-340, Apr 1988.

[86] F. Fahroo and I. M. Ross, "Costate Estimation by a Legendre Pseudospectral Method," *Journal of Guidance, Control and Dynamics*, vol. 24, no. 2, pp. 270-277, March-April 2001.

[87] F. Fahroo and I.M. Ross, "Pseudospectral Methods for Infinite-Horizon Nonlinear Optimal Control Problems," *Journal of Guidance, Control and Dynamics*, vol. 31, no. 4, pp. 927-936, 2008.

[88] Divya Garg et al., "Direct trajectory optimization and costate estimation of finite-horizon and infinite-horizon optimal control problems using a Radau pseudospectral method," *Computational Optimization and Applications*, vol. 49, no. 2, pp. 335-358, 2011.

[89] G. T. Huntington, "Advancement and Analysis of a Gauss Pseudospectral Transcription for Optimal Control Problems," Massachusetts Institute of Technology, PhD Thesis 2007.

[90] Fariba Fahroo and I. Michael Ross, "Advances in Pseudospectral Methods for Optimal Control," in *AIAA Guidance, Navigation and Control Conference*, Honolulu, HI, USA, August 2008.

[91] Qi Gong, I. Michael Ross, and Fariba Fahroo, "Pseudospectral Optimal Control On Arbitrary Grids," in *AAS/AIAA Astrodynamics Specialist Conference*, Pittsburgh, PA, USA, Aug 9-13, 2009.

[92] R. Kress, *Numerical Analysis*. New York: Springer-Verlag, 1998.

[93] C. Canuto, M. Y. Huassaini, A. Quarteroni, and T. A. Zang, *Spectral Methods in Fluid Dynamics*. New York: Springer-Verlag, 1988.

[94] Greg von Winckel. Numerical Integration on an Arbitrary Grid. [Online]. http://www.mathworks.com/matlabcentral/fileexchange/6864-numerical-integration-on-an-arbitrary-grid

[95] Greg von Winckel. Pseudospectral Differentiation on an Arbitrary Grid. [Online]. http://www.mathworks.com/matlabcentral/fileexchange/5515-pseudospectral-differentiation-on-an-arbitrary-grid

[96] G. Szego, *Orthogonal Polynomials*. Providence, Rhode Island: American Mathematical Society, 1939.

[97] A. V. Rao, "A Survey of Numerical Methods for Optimal Control," in *AAS/AIAA Astrodynamics Specialist Conference*, Pittsburgh, PA, USA, August 10-13, 2009.

[98] C. B. Boyer and U. C. Merzbach, *A History of Mathematics*. New York: John Willey, 1991.

[99] A.R. Babaei and M. Mortazavi, "Three-Dimensional Curvature-Constrained Trajectory Planning Based on In-Flight Waypoints," *Journal of Aircraft*, vol. 47, no. 4, Jul-Aug 2010.

[100] M. Shanmugavel, A. Tsourdos, R. Zbikowski, and B.A. White, "Path Planning of Multiple UAVs using Dubins Sets," in *AIAA Guidance, Navigation, and Control Conference and Exhibit*, San Franscisco, CA, USA, 15-18 Aug, 2005.

[101] X. Ma and D.A. Castanon, "Receding Horizon Planning for Dubins Traveling Salesman Problems," in *Proceedings of the 45th IEEE Conference on Decision & Control*, San Diego, CA, USA, 13-15 Dec, 2006.

[102] K. Savla, E. Frazzoli, and F. Bullo, "Travelling Salseperson Problems for the Dubins Vehicle," *IEEE Transactions on Automatic Control*, vol. 53, no. 6, Jul 2008.

[103] X. Yu and J.Y. Huang, "A Genetic Algorithm for the Dubins Traveling Salesman Problem," in *Proceedings of 2012 IEEE International Symposium on Industral Electronics (ISIE)*, Hangzhou, China, May 28-31, 2012.

[104] G. Gutin and A.P. Punnen, *The Travelling Salesman Problem and Its Variations*. New York: Kluwer Academic Publishers, 2004.

[105] M. Bellmore and G.L. Nemhauser, "The Traveling Salesman Problem: A Survey," *Operations Research*, vol. 16, no. 3, pp. 538-558, May-Jun 1968.

[106] P. Milotis, "Integer Programming Approaches to the Travelling Salesman Problem," *Mathematical Programming*, vol. 10, pp. 367-378, 1976.

[107] R. Bellman, "Dynamic Programming Treatment of the Travelling Salesman Porblem," *Journal of ACM*, vol. 9, no. 1, pp. 61-63, 1961.

[108] D. Davendra, *Traveling Salesman Problem - Theory and Application*. India: InTech, 2010.

[109] J.L. Ny and E. Feron, "An Approximation Algorithm for the Curvature Constrained Traveling Salesman Problem," in *Proceedings of the 43rd Annual Allerton Conference on Communications, Control and Computing*, Monticello, Illinois, USA, Sep 28-30,2005.

[110] K. Savla, E. Frazzoli, and F. Bullo, "On the Point-to-point and Traveling Salesperson Problems for Dubins' Vehicle," in *American Control Conference*, Portland, OR, USA, June 2005.

[111] J.L. Ny, E. Feron, and E. Frazzoli, "On the Dubins Traveling Salesman Problem," *IEEE Transactions on Automatic Control*, vol. 57, no. 1, Jan 2012.

[112] L.E. Dubins, "On Curves of Minimal Length with a Constant on Average Curvature and with Prescribed Initial and Terminal Positions and," *American Journal of Matehematics*, vol. 79, no. 3, pp. 497-516, Jul 1957.

[113] Emile Aarts and Jan K. Lenstra, *Local Search in Combinatorial Optimization*, 1st ed. New York, USA: John Wiley & Sons, Inc., 1997.

[114] S.N. Sivanandam and S.N. Deepa, *Introduation to Genetic Algorithms*. Heidelberg: Springer-Verlag, 2008.

[115] J.H. Holland, *Adapation in Natural and Artificial Systems*.: The MIT Press, 1992.

[116] P. Larratiaa, C.M.H. Kuijpers,.H. Muga I. Inza, and S. Dizadrevic, "Genetic Algorithms for the Travelling Salesman Problems: A Review of Representations and Operators," *Artificial Intelligence Review*, vol. 13, pp. 129-170, 1999.

[117] L. Davis, "Applying Adaptive Algorithms to Epistatic Domains," in *Proceeding of the International Joint Conference on Artificial Intelligence*, Los Angeles, CA, USA, 1985.

[118] Z. Michalewicz, *Genetic Algorithms + Data Structures = Evolution Program*. Berlin: Springer-Verlag, 1996.

[119] Olivier Toupet and Gregory Mark, "Design and Optimization of a UAV Platform," in *46th AIAA/ASME/ASCE/AHS/ASC Structures, Structural Dynamics & Materials Conference*, Austin, Texas, USA, 18-21 Apr, 2005.

[120] Andras Sobester and Andy J. Keaney, "Multidisciplinary Design Optimization of UAV Airframes," in *47th AIAA/ASME/ASCE/AHS/ASC Structures, Structural Dynamics, and Materials Confere*, Newport, Rhode Island, USA, 1-4 May, 2006.

[121] Ohad Gur and Aviv Rosen, "Optimizing Electric Propulsion Systems for UAVs," in *12th AIAA/ISSMO Multidisciplinary Analysis and Optimization Conference*, Victoria, British Columbia, Canada, 10-12 Sep, 2008.

[122] Bryan Morrisey and Rob McDonald, "Multidisciplinary Design Optimization of an Extreme Aspect Ratio HALE UAV," in *9th AIAA Aviation Technology, Integration, and Operations Conference (ATIO)*, Hilton Head, SC, USA, 21-23

Sep, 2009.

[123] Danielle S. Soban and Eric Upton, "Design of a UAV to Optimize Use of Fuel Cell Propulsion Technology," in *Infotech@Aerospace*, Arlington, Virginia, USA, 26-29 Sep, 2005.

[124] Taeyun Paul Choi, "A Recourse-based Solution Approach to the Design of Fuel Cell Aeropropulsion System," Georgia Instutite of Technology, Atlanta, GA, PhD Thesis 2008.

[125] Blake Almy Moffitt, "A Methodology for the Validated Design Space Exploration of Fuel Cell Powered Unmanned Aerial Vehicles," Georgia Institute of Technology, Atlanta, PhD Thesis May 2010.

VITA

Min Zhou was born on Jan 17, 1979 in Jiangshan, Zhejiang, China. He received his Bachelor degree in Mechanical Engineering from Nanyang Technological University, Singapore, in 2001. After graduation, he started his job at DSO National Laboratories, Singapore, where his work responsibilities were mainly on the design, fabrication, and testing of UAVs, including both fixed-wing configurations and rotary-wing configurations. While he was on the full-time job at DSO, he also enrolled on a part-time graduate course at National University of Singapore in 2005, and he received his Master degree in Mathematics in 2007.

Zhou was awarded the DSO Postgraduate Scholarship in January 2007, and he joined the School of Aerospace Engineering at Georgia Institute of Technology for his Ph.D. study in August 2008, under the supervision of Dr. J.V.R. Prasad. Since then, he has been working on the trajectory optimization for fuel cell powered UAVs. He is expecting his Ph.D. degree in December 2013.